

FINAL REPORT

EM3 – COMPONENT ARRAY SENSORS FOR UXO DISCRIMINATION One Year Study

SERDP Project MR-1445

SEPTEMBER 2006

Dr. Michael Asten
Mr. Gary Hooper
Flagstaff GeoConsultants, Pty. Ltd.

Mr. Andrew Duncan
ElectroMagnetic Imaging Technology, Pty. Ltd.

This document has been cleared for public release



Report Documentation Page				Form Approved OMB No. 0704-0188	
Public reporting burden for the collection of information is estimated to average 1 hour per response, including the time for reviewing instructions, searching existing data sources, gathering and maintaining the data needed, and completing and reviewing the collection of information. Send comments regarding this burden estimate or any other aspect of this collection of information, including suggestions for reducing this burden, to Washington Headquarters Services, Directorate for Information Operations and Reports, 1215 Jefferson Davis Highway, Suite 1204, Arlington VA 22202-4302. Respondents should be aware that notwithstanding any other provision of law, no person shall be subject to a penalty for failing to comply with a collection of information if it does not display a currently valid OMB control number.					
1. REPORT DATE SEP 2006		2. REPORT TYPE		3. DATES COVERED 00-00-2006 to 00-00-2006	
4. TITLE AND SUBTITLE EM3 - Component Array Sensors for UXO Discrimination. One Year Study				5a. CONTRACT NUMBER	
				5b. GRANT NUMBER	
				5c. PROGRAM ELEMENT NUMBER	
6. AUTHOR(S)				5d. PROJECT NUMBER	
				5e. TASK NUMBER	
				5f. WORK UNIT NUMBER	
7. PERFORMING ORGANIZATION NAME(S) AND ADDRESS(ES) Flagstaff GeoConsultants, Pty. Ltd, 337A Lennox Street Suite 2, Richmond South, Victoria Australia 3121,				8. PERFORMING ORGANIZATION REPORT NUMBER	
9. SPONSORING/MONITORING AGENCY NAME(S) AND ADDRESS(ES)				10. SPONSOR/MONITOR'S ACRONYM(S)	
				11. SPONSOR/MONITOR'S REPORT NUMBER(S)	
12. DISTRIBUTION/AVAILABILITY STATEMENT Approved for public release; distribution unlimited					
13. SUPPLEMENTARY NOTES					
14. ABSTRACT					
15. SUBJECT TERMS					
16. SECURITY CLASSIFICATION OF:			17. LIMITATION OF ABSTRACT Same as Report (SAR)	18. NUMBER OF PAGES 113	19a. NAME OF RESPONSIBLE PERSON
a. REPORT unclassified	b. ABSTRACT unclassified	c. THIS PAGE unclassified			

This report was prepared under contract to the Department of Defense Strategic Environmental Research and Development Program (SERDP). The publication of this report does not indicate endorsement by the Department of Defense, nor should the contents be construed as reflecting the official policy or position of the Department of Defense. Reference herein to any specific commercial product, process, or service by trade name, trademark, manufacturer, or otherwise, does not necessarily constitute or imply its endorsement, recommendation, or favoring by the Department of Defense.

TABLE OF CONTENTS

1.	ACKNOWLEDGEMENTS.....	10
2.	EXECUTIVE SUMMARY	11
2.1.	Background to the UXO discrimination requirement	11
2.2.	The BEAMOD proposal	11
2.3.	First year objectives	11
2.4.	Criterion for success of the first year project.....	12
2.5.	Criterion for recommendation for project continuance into further years	13
2.6.	Declaration of successful outcome, and recommendation from the first year project	15
2.7.	SERDP action requested	15
3.	THE BEAMOD™ CONFIGURATION.....	16
3.1.	B-field sensors.....	16
3.2.	Component advantage of B-field sensors	16
3.3.	Decay sensitivity advantage of B-field sensors.....	17
3.3.1.	<i>Mathematical model</i>	17
3.3.2.	<i>Modeling example</i>	18
3.4.	Prototype design of the BEAMOD™ system	20
3.5.	The BEAMOD™ Mk. 1 Laboratory Bench Prototype	22
3.6.	The BEAMOD™ Mk2 mobile prototype	23
3.7.	Specifications of the Mk2 BEAMOD™ System	24
4.	TEST FACILITIES FOR THIS PROJECT	29
4.1.	EMIT Test Pit.....	29
4.2.	Newholme UXO Test Range	30
5.	CHARACTERISATION OF B-FIELD SENSORS.....	32
5.1.	Introduction: Early Tests.....	32
5.1.1.	<i>Fluxgate Sensor</i>	32
5.1.2.	<i>SQUID sensor</i>	33
5.2.	Processing developed for BEAMOD™ sensors	34
5.3.	Linearity and decay of Fluxgate and SQUID sensors.....	36
5.4.	Algorithm for assessing noise level in presence of signal	40
5.5.	Intrinsic Noise Level: Fluxgate and SQUID Sensors.....	42
5.6.	Survey Noise Level: Environmental at EMIT Test Pit	42
5.7.	Survey Noise Level: Environmental at EMIT Bench Test	46
5.8.	Consequences of slew rate, noise and linearity studies on B-field sensors.....	51
6.	EM63 RESULTS OVER TEST PIT	52
6.1.	EM63 Transmitter and Receiver Moments and Waveform	52
6.2.	Selection of targets.....	54
6.3.	Geological background and noise at EMIT test pit.....	55

6.4. Summary of results	57
6.5. Comparison of target responses with modeling using a conductive permeable prism approximation.....	58
7. B-FIELD SENSOR RESULTS OVER TEST PIT	62
7.1. Selection of targets.....	62
7.2. Geological background and noise at EMIT test pit.....	62
7.3. Summary of results using B-field sensors.....	66
7.4. Comparison of target responses with modeling using a conductive permeable prism approximation.....	68
7.5. Assessment of maximum depth of detection, EM63 vs. fluxgate sensor.....	72
7.6. Summary of performance advantage in depth detection.....	78
8. FLUXGATE MAGNETOMETER RESULTS OVER NEWHOLME UXO TEST RANGE (ARMIDALE, NSW AUSTRALIA).....	79
8.1. Geological background	79
8.2. Response of rocket heads and BDU33 practice bombs.....	82
8.3. Response of 500 lb Mk 82 bombs.....	84
8.4. Response of a target acquired from a moving platform.....	86
8.5. Conclusions on response of a target acquired from a moving platform.....	89
9. COMPARISON OF POWER-LINE NOISE REJECTION WITH BEAMOD™ AND EM63	90
9.1. EM63 Profile.....	90
9.2. Fluxgate Sensor Profile.....	92
9.3. SQUID Profile.....	94
9.4. Conclusions on success of power line noise rejection	95
10. SCOPING OF AN ALGORITHM FOR FAST INVERSION OF EMI DATA OVER A FERROUS TARGET.....	97
11. INVERSION SENSITIVITY WITH THE BEAMOD™ CONFIGURATION.....	98
11.1. Modeling and inversion of synthetic data with the BEAMOD™ configuration.....	98
11.2. Key results from modeling and inversion studies with the BEAMOD™ configuration on synthetic data.....	101
11.3. Modeling and inversion of field data with the BEAMOD™ configuration.....	102
11.4. Key results from modeling and inversion studies with the BEAMOD™ configuration on field data	106
12. SUMMARY OF RESULTS MEASURED AGAINST PERFORMANCE METRICS AND RECOMMENDATION	107
12.1. Metrics objectives	107
12.2. Assessment of results against metrics: noise, performance and cost	107
12.2.1. Noise characteristics.....	107
12.2.2. Compare fluxgate SQUID and EM63 systems over a suite of ordnance targets	108
12.2.3. Advantage of the vector sensor for determining position and orientation of a target.	108
12.2.4. Signal processing for reduction of cultural (power line) noise.	109
12.3. Performance of B-field sensor on a moving platform.....	109

12.4. Recommendation	109
13. REFERENCES	110
A2. Noise characteristics	111
A3. Comparison of signal/noise over metallic targets	112
A4. Advantages of the vector sensor in BEAMOD™ configuration	112
A5. Advantages of real-time signal processing in BEAMOD™ system	113
A6. Criterion for success of this project	113

APPENDICES

"

"

APPENDIX A

METRICS FOR PROJECT MR-1445

- A1. Objectives
- A2. Noise characteristics
- A3. Comparison of signal/noise over metallic targets
- A4. Advantages of the vector sensor in BEAMOD™ configuration
- A5. Advantages of real-time signal processing in BEAMOD™ system
- A6. Criterion for success of this project

.....**NUV'QH'HK WTGU**

"

"

"

"

"

"

Figure 1 – Pictures of Bartington fluxgate magnetometer (left) and CSIRO SQUID magnetometer (right)	16
Figure 2 – Modeled copper pipe at depth 0.75 m, and half-size scrap at depth 0.5 m	19
Figure 3 – B-field and dB/dt responses of copper pipe and half-size scrap	19
Figure 4 – Alternative designs for an array of three, 3-component sensors	20
Figure 5 – The BEAMOD™ Mk.1 bench system used for characterisation studies on the fluxgate and SQUID sensors.	22
Figure 6 – The BEAMOD™ Mk.2 mobile prototype system used for noise and profile studies on munitions targets with the fluxgate and SQUID sensors.	23

Figure 7 – Drawings for the BEAMOD™ main platform	26
Figure 8 – Drawings for the BEAMOD™ fluxgate sensor Helmholtz coil	27
Figure 9 – Drawings for the BEAMOD™ SQUID sensor Helmholtz coil	28
Figure 10 – BEAMOD™ Mk.1 prototype system (left) and EM63 (right) used over the EMIT test pit, Mundaring, Western Australia	29
Figure 11: Targets used in studies at the EMIT test pit.	30
Figure 12 – Targets used in studies at the Newholme UXO Test Range, Armidale NSW	31
Figure 13 – Decay curve of fluxgate sensor used in BEAMOD™ Mk 1 system, over test pit, with no target	32
Figure 14 - The effectiveness of the leveling algorithm is demonstrated on a profile of SQUID data	35
Figure 15 - Linearity test on bench of fluxgate sensor with no target	37
Figure 16 - Linearity test on bench of fluxgate sensor with and without a target	37
Figure 17 - Superimposed leveled normalized decay curve responses from Figure 16, for three transmitter currents, with the fluxgate sensor over the copper pipe target	38
Figure 18 - Linearity test on bench of SQUID sensor with and without a target	39
Figure 19: Superimposed leveled and stripped decay curve responses from Figure 18, for three transmitter currents, with the SQUID sensor over the copper pipe target	39
Figure 20: The process of for assessing Gaussian noise level in the presence of a synthetic signal	41
Figure 21: Intrinsic noise of fluxgate sensor measured in mumetal shield, using BEAMOD™ time windows, no transmitter	43
Figure 22: Intrinsic noise of SQUID sensor measured in mumetal shield, using BEAMOD™ time windows, no transmitter	44
Figure 23: Noise of fluxgate sensor in a 4 m profile of 15 points over EMIT test pit, using BEAMOD™ time windows, no transmitter	45
Figure 24: Noise of SQUID sensor in a 4 m profile of 15 points over EMIT test pit, using BEAMOD™ time windows, no transmitter	46
Figure 25: Estimation of noise in profile over the EMIT test pit, fluxgate sensor	47
Figure 26: Estimation of noise in profile over the EMIT test pit, SQUID sensor.	48
Figure 27: Noise of fluxgate sensor in the 2m profile of Figure 25	49
Figure 28: Noise of SQUID sensor in the 2m profile of Figure 26	50
Figure 29 Side view schematic diagram showing the geometry of the EM63 metal detector with transmitter and receiver coils above ground level	52
Figure 30 EM63 waveform – At 50 Hz power line setting and M frequency, measured base frequency was 4.5 Hz	53
Figure 31: EM63 waveform – At 50 Hz powerline setting and H frequency, repetition frequency of the waveform is at 30 Hz while turned on – 8.333 msec +/-off/-off	53
Figure 32: EM63 profiles over EMIT test pit, with no target	56
Figure 33: Noise of EM63 profile in a 4m profile over the EMIT test pit, speed 0.5 m/sec ...	57
Figure 34 – EM63 profiles Line 203 over a 40mm cannon shell oriented horizontally, axis parallel with traverse. Base 300mm below pit cover.	60
Figure 35: BEAMOD™ Mk2 profiles, using fluxgate sensors measuring three components in a profile over the EMIT test pit, with no target	63
Figure 36: BEAMOD™ Mk2 profiles, using SQUID sensors measuring two components in a profile over the EMIT test pit, with no target.	64

Figure 37: Noise of fluxgate sensor with BEAMOD™ Mk 2 system in a 4m profile over EMIT test pit, using BEAMOD™ time windows, transmitter current 12A.	65
Figure 38: Noise of SQUID sensor with BEAMOD™ Mk 2 system in a 4 m profile over EMIT test pit, using BEAMOD™ time windows, transmitter current 3.5A.	66
Figure 39: Three-point half profile observed and model responses of a 400mm x 100mm copper pipe at true depth 530mm below the pit cover, as observed using the fluxgate sensor.	69
Figure 40: Observed and model profile responses of a 400mm x 100mm copper pipe at true depth 880mm below the pit cover, as observed using the fluxgate sensor.	69
Figure 41: Observed and model profile late-time responses of a 40mm cannon shell with base at ground level (pit cover), as observed using the fluxgate sensor.	70
Figure 42: Observed and model profile late-time responses of a 40mm cannon shell with base at depth 300 mm below pit cover, as observed using the fluxgate sensor.	70
Figure 43: Observed and model early-time profile responses of a 40mm cannon shell with base at ground level (pit cover), as observed using the fluxgate sensor.	71
Figure 44 Model response of the copper pipe target oriented horizontally, to three EMI systems.	74
Figure 45 Model response of the 40mm shell target oriented horizontally, to two EMI systems	75
Figure 46 – Modeled response of the 75 mm shell target oriented horizontally, to two EMI systems	76
Figure 47 – Modeled response of the BDU33 practice bomb target oriented horizontally, to two EMI systems.	77
Figure 48 – Profile with BEAMOD™ Mk2, transmitter current 12A, and fluxgate sensor at south-west corner of Newholme test site, without a target (File FG702)	80
Figure 49 – Profile with BEAMOD™ Mk2 and fluxgate sensor at east edge of Newholme test site, without a target (File FG712).	80
Figure 50 – Profile with BEAMOD™ Mk2 and fluxgate sensor at EMIT test pit, without a target (File FG804).	81
Figure 51 – Profile with BEAMOD™ Mk2 and fluxgate sensor at Newholme test range, same location as Figure 48 with a 40 mm shell as target	81
Figure 52 – Profile with BEAMOD™ Mk2 and fluxgate sensor at Newholme test range, target 11 (PWH rocket head) at depth 500 mm, notionally below station 2.0.	82
Figure 53 – Profile with BEAMOD™ Mk2 and fluxgate sensor at Newholme test range, target 12 (PWH rocket head) at depth 500 mm, notionally below station 2.0.	83
Figure 54 – Profile with BEAMOD™ Mk2 and fluxgate sensor at Newholme test range, target 13 (PWH rocket head) at depth 500 mm, oriented vertical, notionally below station 2.0.	83
Figure 55 – Profile with BEAMOD™ Mk2 and fluxgate sensor at Newholme test range, target 34 (BDU33 practice bomb) at depth 800 mm, notionally below station 2.0	84
Figure 56 – Profile with BEAMOD™ Mk2 and fluxgate sensor at Newholme test range, target 33 (BDU33 practice bomb) at depth 2 m, notionally below station 2.0	84
Figure 57 – Profile with BEAMOD™ Mk2 and fluxgate sensor at Newholme test range, target 21 (Mk 82 bomb, 500 lb) at depth 600 mm, notionally below station 2.0.	85
Figure 58 – Profile with BEAMOD™ Mk2 and fluxgate sensor at Newholme test range, target 4 (Mk 82 bomb, 500 lb) at depth 2.6 m, notionally below station 2.0.	86
Figure 59 – Conventional stop-start profile with BEAMOD™ Mk2 and fluxgate sensor at Newholme test range, target 13 (PWH rocket head 2.75 inch, oriented vertically).	87

Figure 60 – Continuous motion profile with BEAMOD™ Mk2, medium frequency, and fluxgate sensor at Newholme test range, target 13 (PWH rocket head 2.75 inch, oriented vertically).	88
Figure 61 – Continuous motion profile, as for Figure 60 but with a low transmitter frequency of 2.08 Hz (File FG720).	88
Figure 62 – Continuous motion profiles with BEAMOD™ Mk2, at Newholme test range, no target below the profile.	89
Figure 63 – BEAMOD™ Mk 2 and EM63 instruments in use under high-tension power lines	90
Figure 64 – Profiles acquired with the EM63 and BEAMOD™ Mk2 with fluxgate sensor, under power lines	91
Figure 65 Three component profile acquired with the BEAMOD™ Mk2 with fluxgate sensor under power lines.	93
Figure 66 Profiles acquired with the BEAMOD™ Mk2 with fluxgate sensor, under power lines, at low transmitter frequency.	94
Figure 67 Profiles acquired with the BEAMOD™ Mk2 with SQUID sensor, under power lines	96
Figure 68 - Starting and fitted models for an example of inversion of synthetic B-field data for a single 3-component B-field sensor.	99
Figure 69 - Profiles and inverted model with all three sensor positions of BEAMOD™ Mk2 (fluxgate sensors) at Newholme test range.	103
Figure 70 - Profiles and model as for Figure 69, but with (a-c) shorter target length of 0.15 m, and (d-f) with longer target length of 0.4 m.	105

LIST OF TABLES

Table 1 – Time windows (33 time windows when using a 2.08 Hz transmitter frequency): ..	25
Table 2 – Time Windows (33 time windows when using a 2.08 Hz Transmitter Frequency)	54
Table 3 – EM63 time domain EMI observations on munitions in EMIT pit	59
Table 4 - Time-Domain EMI Observations on Munitions at EMIT Test Pit	67
Table 5 – Inversion study on synthetic three-component in-loop B-field data.	100
Table 6 – Inversion study on synthetic single Z-component in-loop B-field data.	100
Table 7 – Inversion study on synthetic single Z-component in-loop B-field data.	101
Table 8 – Metallic Objects and Munitions under Test – Project MR-1445	112

ACRONYMS

BEAMOD™	B-field Electromagnetic Array for Munitions and Ordnance Detection
EMI	ElectroMagnetic Induction
EMIT	ElectroMagnetic Imaging Technology Pty Ltd
FAR	False alarm rate
UXO	Unexploded Ordnance
SQUID	Superconducting Quantum Interference Device

1. ACKNOWLEDGEMENTS

This study was supported by the Strategic and Environmental Research and Development Program (SERDP) under Contract UX-1445. The authors thank colleagues: Dr John Stanley of GAP Geophysics Ltd, Rob Siegel of Science Applications International Corporation (SAIC), Dr Jon Miller of AETC Inc, and Len Pasion of The University of British Columbia for many fruitful discussions.

We also thank the Australian Air Force who through Dr John Stanley of G-Tek Pty Ltd (now GAP Geophysics Pty Ltd) made available to this Project the suite of munitions targets. Dr Stanley is a past and present Co-Investigator on ESTCP projects, and his cooperation with this Project has been of great value.

—

This document is to be approved for public release and distribution is unlimited.

DISCLAIMERS

VIEWS, OPINIONS, AND/OR FINDINGS CONTAINED IN THIS REPORT ARE THOSE OF THE AUTHOR(S) AND SHOULD NOT BE CONSTRUED AS AN OFFICIAL DEPARTMENT OF THE ARMY POSITION OR DECISION UNLESS SO DESIGNATED BY OTHER OFFICIAL DOCUMENTATION.

Flagstaff has prepared this report based upon information believed to be accurate at the time of completion, but which is not guaranteed. Flagstaff makes no representation or warranty as to the accuracy, reliability or completeness of the information contained in this report and will not accept liability to any person for any errors or omissions or for losses or damages claimed as a result, directly or indirectly, of items discussed, opinions rendered or recommendations made in this report, except for statutory liability which may not be excluded.

2. EXECUTIVE SUMMARY

2.1. Background to the UXO discrimination requirement

The requirement for high-technology discrimination between metal fragments and intact munitions was spelled out by Dr William Delaney of the Defense Science Board, in a Keynote Paper (Delaney, 2003). He noted the need for the screening of 2 million acres of current and former US military sites for the presence of UXOs, and estimated the cost of the current 100:1 false-alarm rate (FAR) at \$30 billion for digging holes on targets of which 99% are associated with scrap metal or artifacts. He called for discrimination tools capable of reducing the FAR.

2.2. The BEAMOD proposal

In answering this call, Flagstaff GeoConsultants initially submitted its proposal for BEAMOD™ (**B**-field **E**lectromagnetic **A**rray for **M**unitions and **O**rdnance **D**etection) based over three years for the development of a prototype sensor system for UXO discrimination. The project's target expectation, coupled with the development of discrimination algorithms, is the possible reduction in FAR rates by 80%, implying potential savings in digging holes in the order of \$24 billion.

SERDP approved the first year of the BEAMOD™ development and Project UX-1445 was commissioned to investigate how hardware and software innovations in time-domain electromagnetic induction (EMI) instrumentation, developed within the mineral exploration industry, might be applied to UXO detection in such a way as to enhance detection and discrimination capabilities on buried munitions and scrap metal.

The one year project characterizes and investigates the use of two vector magnetic field sensors (one fluxgate magnetometer and one SQUID magnetometer) and develops complementary processing and modeling algorithms in order to enhance measurement and interpretation capabilities of EMI systems in UXO applications.

Three key differences between munitions detection and mineral exploration are noted:

1. in munitions detection, transmitters and targets are a factor of 100 to 1000 smaller than those common in mineral exploration,
2. in munitions detection, targets are majority ferrous objects having strong magnetic polarization responses which dominate over induction current responses, and
3. in munitions detection, the local environment may be electrically noisy requiring additional signal processing to reduce that 'cultural' noise.

2.3. First year objectives

In order to maximize the opportunity for the BEAMOD™ prototype to be successful, instrumental innovations beyond mineral exploration standards are required, leading to three hardware objectives in the first year of the project:

1. to characterize noise levels, sensitivity and linearity of three-component fluxgate and SQUID sensors to detect the pulse-EM induced field, inside and outside the transmitter loop,
2. to evaluate the benefits of measuring EM magnetic field rather than time rate of change of EM field the vector magnetic field of an EM response; quantify the higher sensitivity to intact and/or buried UXOs vs. near-surface scrap, achievable with these sensors, and
3. to suppress interfering EM noise from infrastructure such as power lines and communication equipment, thus achieving a lower noise floor.

In addition, a fourth objective was to develop a conceptual complementary software interpretation methodology:

4. scope out an inversion method which can yield orientation of an eddy current “filament” from data acquired at three vector sensor locations (inside, outside in front, and outside behind the transmitter loop).

In this one-year project, tests authorized for the project were limited to the use of one sensor (fluxgate or SQUID) only, although the project envisages future use of an array of three sensors (fluxgate or SQUID).

SERDP is looking for Flagstaff GeoConsultants to make a recommendation on which sensor to take forward into the following years of the BEAMOD™ prototype development.

2.4. Criterion for success of the first year project

The criterion proposed for the first year of the project was as follows:

One of,

One or both B-field vector sensors achieves a greater time window range of detection (i.e. bandwidth of detection) than the EM63, for the majority of the targets listed in Table 4,

or,

One or both B-field vector sensors in BEAMOD™ configuration has comparable bandwidth of detection compared with the EM63, but provides higher precision in fixing location and orientation of an ordnance target, when inverting field or model data.

or,

One or both of the B-field vector sensors in BEAMOD™ trials, interfaced to "new" (SMARTem) real-time signal processing equipment, has comparable bandwidth of detection compared with the EM63 in measurements relatively free of power line noise, but provides an improvement in bandwidth of detection of at least a factor of 2 over EM63 in a "culturally noisy" environment in the vicinity of power lines.

Of these three “criteria for success”, we find **all three have been met by this first year project**, with the following findings:

From Section 7.6, we have: “In terms of window of detection, the fluxgate sensor shows increases of between 25% and 125% in late-time detection for steel targets (strongest increase for largest targets), but a decrease in window of detection for the copper pipe target”.

From Section 11, we have results of a study of inversion effectiveness on synthetic data for a single-component sensor, a single vector sensor, and the full BEAMOD™ array of three vector sensors. These results show that using synthetic data we have:

- A single vector sensor delivers an order of magnitude greater accuracy in location in X,Y,Z space and orientation of the target, compared with the use of z-component only data.
- Comparison of the use of a single vector sensor and the BEAMOD™ array of three vector sensors in model studies shows that where the target size is unknown, the single vector sensor is likely to produce unstable orientation estimates, whereas use of the array of three vector sensors delivers accurate and stable estimates of orientation of the unknown target.

In addition, a study using observed data compared with model data using the full BEAMOD™ configuration over a PWH rocket head at the Newholm UXO test range allows us to say:

- We propose a hypothesis for future studies, that it is feasible with the full BEAMOD™ geometry to determine position, orientation AND nose direction of a munitions target, and that the difference in response between nose and tail of a flat-lying target may be an additional tool for discrimination of target type.

From Sections 9.2 and 9.4, we have a significant result in signal processing applied to the reduction of 50 Hz noise in the vicinity of power lines:

- The BEAMOD™ system achieves a 5:1 improvement in suppression of 50 Hz noise in time windows > 1msec, compared with the EM63. This applies over similar sample stacking times, and similar transmitter moments.

2.5. Criterion for recommendation for project continuance into further years

The criterion proposed at the SAB meeting in October 2004 for the first year of the project was as follows:

Proceed if:

Noise level of either B-field sensor (in presence of transmitter) is below noise level of conventional coil receiver (as measured by threshold depth of detection for one or more sample 20 mm, 60 mm & 155 mm shells),

and

Scoping of inversion of modeled vector data recorded simultaneously from three sensors proves feasibility of the BEAMOD™ discrimination algorithm.

Due to the difficulty of quantifying noise in absolute units, which is a result of lack of published system information on the EM63 conventional instrument, and on the fact that conventional and B-field systems measure noise in different units, we have developed a relative measure for comparison of noise levels, based on the maximum depth of detection of a given target for each system. The lower the noise level of the system, the deeper the threshold depth of detection for a given target.

Both of the above two criteria have been met in this first year project, using available ordnance items 20mm, 40mm, 75mm shells, and a BDU33 practice bomb, diameter 150mm.

The first of the above criteria has been met by development of a method for quantifying noise levels for a profile (instrumental and geological), followed by modeling studies which establish depth of detection for a specific target type as determined by the criterion of a 2:1 target signal amplitude to noise ratio.

Depth of detection studies in Sections 7.6 and 8.3 summarized thus:

Copper pipe: The SQUID has an advantage of 1700 mm vs 1400mm for the EM63 and fluxgate (20% deeper - applies only at short window times <1 msec, which is not of high value),

40mm cannon shell: The fluxgate sensor has an advantage of 780 mm vs 530mm for the EM63 (47% deeper),

75mm cannon shell: The fluxgate sensor has an advantage of 1110 mm vs 780mm for the EM63 (42% deeper),

BDU33 practice bomb: The fluxgate sensor and EM63 have comparable depth sensitivity at the intermediate time range 5-10 msec, but the fluxgate is strongly superior at late times of order 20 msec, having a computed depth detection advantage of about 780 mm vs 480 mm for the EM63 (50% deeper).

In addition we have an empirical result with the BEAMOD™ system alone, not yet compared with an EM63 response, that

500 lb Mk 82 practice bomb: The fluxgate sensor detects the target on all three components to a depth of 2.6 m.

The second criterion is met by demonstration of feasibility of inversion of data from a single vector sensor and a full BEAMOD™ array of three vector sensors, as described in Section 11. Model studies and inversions performed on synthetic data show the use of a single vector sensor delivers an order of magnitude greater accuracy in location in X,Y,Z space and orientation of the target, compared with the use of z-component only data.

Comparison of the use of a single vector sensor and the BEAMOD™ array of three vector sensors in model studies shows that where the target size is unknown,

the single vector sensor is likely to produce unstable orientation estimates, whereas use of the array of three vector sensors delivers accurate and stable estimates of orientation of the unknown target.

2.6. Declaration of successful outcome, and recommendation from the first year project

The project has met all three Criteria for Success in Section 2.4, and has met both Criteria for project continuation as listed in Section 2.5.

Section 12 summarizes performance of sensors under study versus agreed metrics for the project, and concludes with the recommendation:

The BEAMOD™ design in its prototype form is proven technically to have superior noise, depth of detection, and capability for determination of target location and orientation. It is recommended that the hardware and software development as envisaged in UX-1445 and the preceding three-year proposal, be funded for a further two years, using the fluxgate magnetometer as the basis for an array of vector sensors.

2.7. SERDP action requested

This report is provided for SERDP to judge progress after the one year of investigations, and to authorize if it sees fit the continuation of the BEAMOD™ development. A cost saving is available relative to the previous three-year proposal, since we recommend use of the fluxgate sensor alone, rather than parallel development of both the fluxgate and SQUID sensors.

3. THE BEAMOD™ CONFIGURATION

3.1. B-field sensors

The two sensors studied in this project are the Bartington Fluxgate magnetometer Type MAG03-MCESL70, and the CSIRO LANDTEM SQUID magnetometer, pictured below.



Figure 1 – Pictures of Bartington fluxgate magnetometer (left) and CSIRO SQUID magnetometer (right)

LEFT: a 3-component vector fluxgate sensor used by EMIT in mineral exploration field trials. Length is 200mm x 20mm diameter.

RIGHT: A LANDTEM 3-component SQUID sensor (boxed with Dewar and electronics) as used in Australia in mineral exploration over highly conductive ore-bodies. Length is 300mm long x 200mm x 150mm high (excluding cap). The cap sits on a small Dewar vessel which holds the liquid nitrogen required for this high-temperature super-conducting device to operate.

3.2. Component advantage of B-field sensors

Induction coil sensors used on commercial metal detectors designed for detection of munitions are typically 500 mm square (Geonics EM63). This makes a 3-component detector geometrically large and logistically unwieldy (a 500mm cube). The logistics become more difficult if we seek to use multiple 3-component sensors in an array of receivers.

The fluxgate magnetometer sensor as implemented by Bartington is approximately 15mm long and it is possible to position three sensors orthogonally, with accompanying electronics, in a cylinder of diameter 20mm and length 200mm (see Figure 1). This represents a huge geometric advantage for the design and use of multiple-component sensors, compared with induction coil sensors. The advantage is further increased with an array of multiple 3-component sensors.

The SQUID magnetometer uses a super-conducting chip the size of a coin which contains three Josephson junctions geometrically orthogonal, thus providing a three-component sensor. The chip resides in a small Dewar vessel containing liquid nitrogen, and requires ancillary electronics which results in a sensor assembly of size 300x200x150mm as shown in Figure 1. Details of the

background to the LANDTEM development and application to mineral exploration are given in Foley et al (1999) and Lee et al (2001).

3.3. Decay sensitivity advantage of B-field sensors

We use the “B-field” terminology here for sensors that measure magnetic field B which became common in the mineral exploration industry when referring to a magnetometer sensor used in EM Induction measurements. This is distinct from an induction coil sensor which measures the time rate of change of magnetic induction, and is referred to by the generic name dB/dt sensor.

We now show the advantage of a B-field sensor over a dB/dt sensor in detection of larger deeper targets versus surface scrap, by means of (a) a simple mathematical concept, and (b) a simple model study. Both demonstrations rely on two basic physical phenomena:

1. B-field EMI early-time (high-frequency) response is proportional to size & depth of target;
2. dB/dt early-time (high-frequency) response is proportional to size, depth and inversely proportional to decay time-constant, hence scrap response is amplified relative to UXO target responses.

3.3.1. Mathematical model

The sensitivity of a pulsed induction EM (also called time-domain EM) system to a target, in the presence of secondary targets and/or a conducting earth, and where signal:noise ratio is limited by EM noise from atmospheric or cultural sources, is complex. A strict comparison of differences between a coil sensor (measuring dB/dt) and a fluxgate or SQUID sensor (measuring magnetic field B) needs to consider each of these items. However a useful and very illuminating comparison of dB/dt vs B field can be made with a much simplified set of assumptions as follows:

Suppose we have a target (intact UXO) that has a step response to a change in primary magnetic field given by the decay curve

$B(t) = X \exp(-t / \tau_t)$, where X is a constant set by transmitter-target-receiver magnetic coupling, and τ_t is the time-constant of exponential decay of eddy currents induced in the target.

Suppose we also have an item of scrap, which typically has a shorter time constant τ_s , and a step response of the form

$B(t) = Y \exp(-t / \tau_s)$, where Y is a constant set by transmitter-target-receiver magnetic coupling, and τ_s is the time-constant of exponential decay of eddy currents induced in the scrap.

The classical coil receiver sensor used in EM instruments will see a combined response from these two objects given by the time rate of change of B, i.e.

$$dB(t)/dt = (X/\tau_t) \exp(-t / \tau_t) + (Y/\tau_s) \exp(-t / \tau_s).$$

Now let us suppose we have an occurrence in a field survey where the target UXO and piece of scrap are giving a similar response at early times ($t \ll \tau_s$) for a classic instrument such as EM61 reading to $t = 1.5$ msec. This condition may be written in the form

$$X/\tau_t = Y/\tau_s,$$

and by our assumption above, the response ratio at early times is

$$\text{UXO: scrap} = 1.$$

Now consider the same survey repeated using B-field sensors such as the fluxgate or SQUID magnetometer. The combined response (decay curve) for the two objects is

$$B(t) = X \exp(-t / \tau_t) + Y \exp(-t / \tau_s),$$

and the response ratio at early times is

$$\text{UXO: scrap} = X/Y = \tau_t / \tau_s.$$

For a UXO (e.g. 150mm shell) with a time constant of 30msec (Miller, 2003), and a scrap item with a time-constant of say 5msec, this implies the B-field measurement will provide a UXO:scrap advantage of 6:1. The B-field sensor thus:

- a. enhances UXO signal relative to scrap, and
- b. improves sensitivity of the EM system to deeper UXO targets below surface scrap.

3.3.2. *Modeling example*

Figure 2 shows a simple model of two metallic items of the same conductivity but different size and burial depth in a resistive half-space. Figure 3 shows their responses on a single profile over the two targets, as seen by a dB/dt sensor, and a B-field detector. The modeling approximation and algorithm used is described in Appendix B.

It is clear from the simple model provided that the B-field response produces a stronger response over the larger target, even though the larger target is at greater depth. Decay curve analysis of the dB/dt response will also show the target at right to be the larger target (slower decay), and obviously if the larger target is sufficiently deep its response amplitude will sink below that of the scrap, but the inherent advantage of improving the target vs scrap response ratios will always be present.

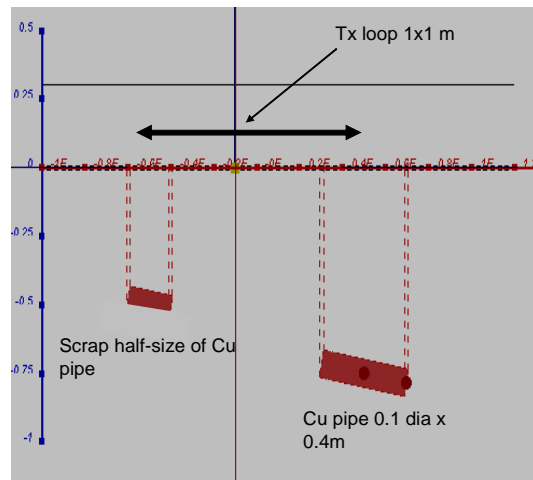


Figure 2 – Modeled copper pipe at depth 0.75 m, and half-size scrap at depth 0.5 m

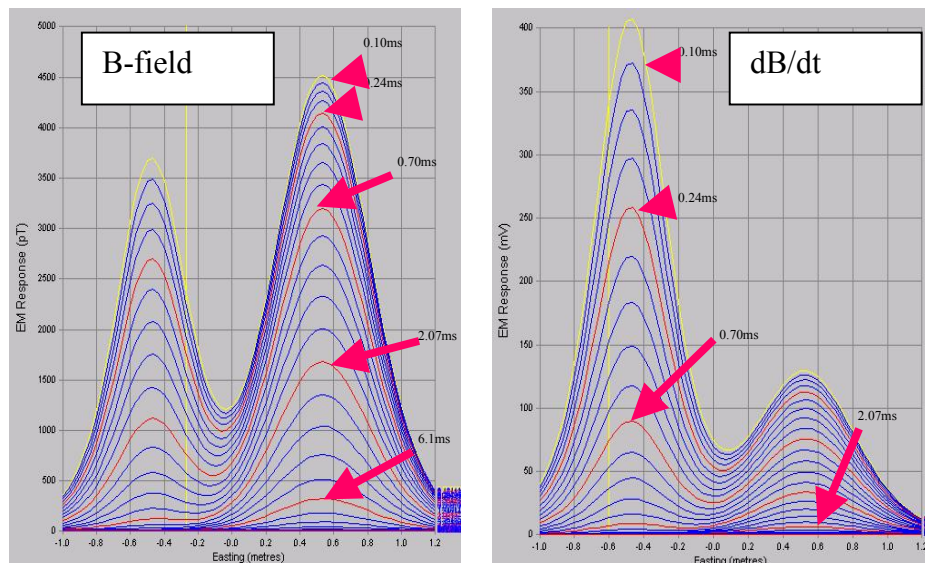


Figure 3 – B-field and dB/dt responses of copper pipe and half-size scrap

LEFT: B-field response; the larger pipe has the larger response.

RIGHT: dB/dt response (EM63 geometry and moment); scrap response dominates at early sample times.

3.4. Prototype design of the BEAMOD™ system

The BEAMOD™ system seeks to improve target detect ability, location and discrimination by utilizing the multiple components available with the B-field sensors, plus multiple sensor positions, made possible by the small size of the sensors.

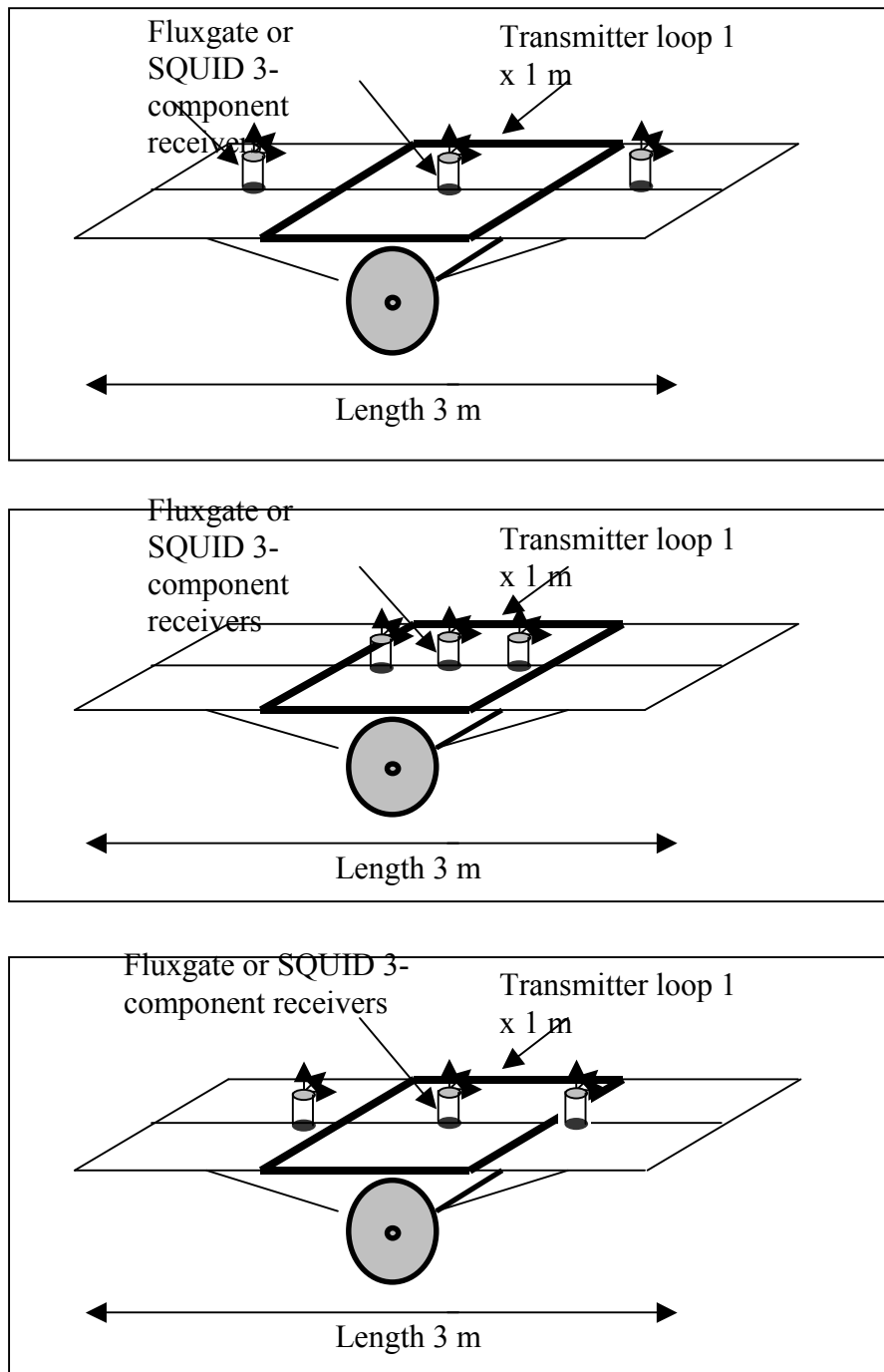


Figure 4 – Alternative designs for an array of three, 3-component sensors.

Three designs have been considered in this one year project, as shown in the above figure. These alternative designs for the array of three sensors (each being a 3-component sensor) are as follows:

1. Two sensors are outside the transmitter loop at distance L from the loop center, where L =loop side length.
2. Two sensors are inside the transmitter loop at distance $4L/10$ from the loop center, where L =loop side length.
3. Two sensors are outside the transmitter loop at distance $0.63L$ from the loop center, where L =loop side length.

Choice of geometry is subject to trade-offs in terms of relative signal strength at the multiple receiver sensors, and primary field strength at the sensors. Relative signal strength is a function of depth to target (a deep target at depth $\gg L$ will show similar response at the three sensors). Primary field strength during the on-pulse of the transmitter is important as it determines and affects the performance of the B-field sensors, as detailed in Section 5 of this Report.

The geometry of Figure 4a with a wide spread of sensors is advantageous in terms of subtending a large angle at a target, which facilitates position location. However the disadvantage is that the ratio of signal strength from a target as detected by the outer sensor versus the center sensor is poor. We compute the secondary field at the three sensor positions due to inductive excitation of a target of size 0.2 m length and diameter 0.1 m, placed below the center of the transmitter. For a target at 0.5m depth (or 0.92m below a transmitter loop, after allowing for ground clearance) the signal strength ratio is of order 0.05 to 0.06 for the vertical component, or 0.2 for the total field.

The geometry of Figure 4b is regarded as undesirable with the two sensors under test, since the primary field close to the transmitter wire, 100mm inside the loop, is a factor of 2.3 larger than the primary field at the center. This places a heavy additional demand on receiver processing outlined in Section 5.2 and has therefore not been considered further in this project.

The geometry of Figure 4c with a sensors placed outside the transmitter loop at a distance $0.63L$ has the advantage that the primary field at the outside sensors is exactly equal and opposite to the primary field at the loop center. The geometry also has the advantage that for a target at 0.5m depth, the signal strength ratio is of order 0.3 for the vertical component, or 0.5 for the total field, and hence the outer sensors and center sensor will have comparable signal/noise characteristics when used for precise location and discrimination studies on targets in the critical 0.5m burial zone. For both these reasons, this is the sensor geometry adopted for the BEAMOD™ system.

3.5. The BEAMOD™ Mk. 1 Laboratory Bench Prototype

Figure 5 shows the bench prototype of a BEAMOD™ system, where a single primary-field nulling (or bucking) coil is used to attenuate the primary field at the receiver sensor. This configuration was used for characterization studies on the two B-field sensors described in Section 5, and for acquisition of sample data over the EMIT test pit. However as the importance of precise nulling of the primary field became apparent, an alternative design using Helmholtz nulling coils was developed.



Figure 5 – The BEAMOD™ Mk.1 bench system used for characterization studies on the fluxgate and SQUID sensors.

LEFT: the fluxgate sensor (FG) surrounded by a nulling coil (NC) and transmitter loop (Tx).

RIGHT: the SQUID sensor (SQ) surrounded by a nulling coil (NC) and transmitter loop (Tx).

The transmitter loop consists of 10 turns, and typically used currents of 1 A in this prototype, giving a low transmitter moment of 10 A.m².

3.6. The BEAMOD™ Mk2 mobile prototype

Figure 6 shows the Mk. 2 BEAMOD™ system which can be moved in profiles across the EMIT test pit, or towed on a “sled” as demonstrated in profiles at the Newholme UXO test range, Armidale, northern NSW, Australia.

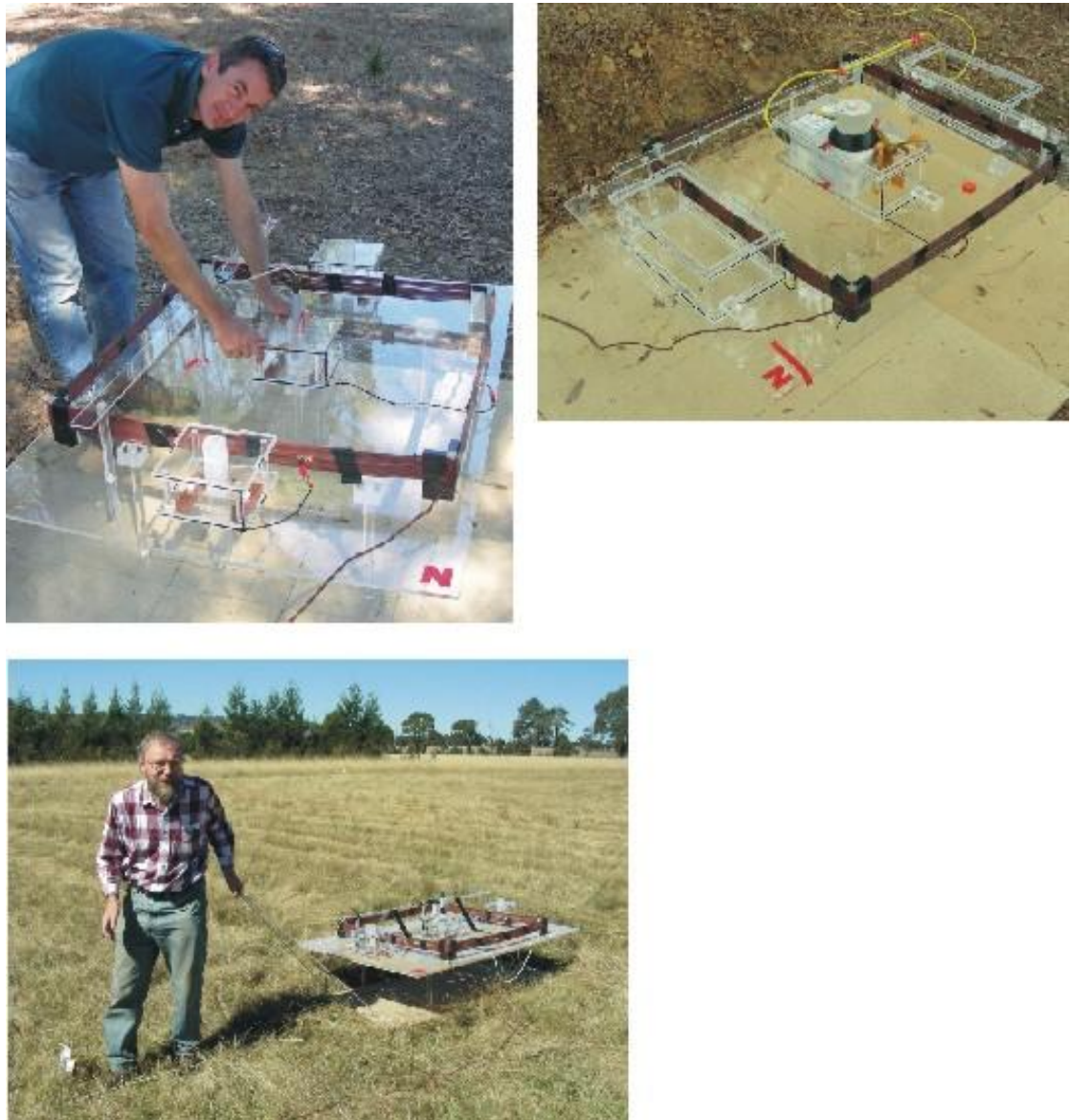


Figure 6 – The BEAMOD™ Mk.2 mobile prototype system used for noise and profile studies on munitions targets with the fluxgate and SQUID sensors.

TOP: Configured with a fluxgate sensor and Helmholtz coils, on the EMIT test pit.

RIGHT: Configured with a SQUID sensor and Helmholtz coils, on the EMIT test pit.

BOTTOM: Configured with a fluxgate sensor and Helmholtz coils, mounted on a sled for profiling over buried munitions on the Newholme UXO test range, Armidale, NSW.

3.7. Specifications of the Mk2 BEAMOD™ System

Transmitter: Zonge ZT-20 driving current typically 12A for fluxgate sensor, or 3.5A for SQUID sensor, giving transmitter moment of 180A.m² or 52A.m².

Operating frequency 2.08Hz for most measurements in this project; 8.33Hz also used and appears satisfactory.

Transmitter loop: 1 x 1 m, 15 turns, center of loop is 395mm above ground surface.

Sensor: Bartington Fluxgate magnetometer Type MAG03-MCESL70, or CSIRO LANDTEM SQUID. Each sensor measures three orthogonal components. One sensor only authorized for use in this project, but system will be designed to use three sensors.

Elevation of sensor measurement point above ground level is 395 mm.

Receiver: EMIT SMARTem Mk 5, with full-waveform processing and smart stacking to reduce power-line and other coherent noise.

Table 1 – Time windows (33 time windows when using a 2.08 Hz transmitter frequency):

NUMTIMES=33	BFREQ=2.08	ONTIME=120.1	OFFTIME=120.1
CENTRE	WIDTH	CENTRE	WIDTH
(msec)	(msec)	(msec)	(msec)
0.1	0.02	7.565	1.89
0.125	0.03	9.39	2.34
0.15	0.04	11.66	2.92
0.195	0.05	14.47	3.62
0.24	0.06	17.965	4.49
0.295	0.07	22.31	5.58
0.365	0.09	27.695	6.93
0.455	0.11	34.38	8.6
0.56	0.14	42.685	10.67
0.7	0.18	52.99	13.24
0.87	0.22	65.785	16.45
1.075	0.27	81.67	20.42
1.34	0.34	101.395	25.35
1.665	0.41		
2.065	0.51		
2.565	0.65		
3.185	0.79		
3.955	0.99		
4.905	1.23		
6.09	1.52		

The following three pages show three figures as follows:

Figure 7. Drawings for the BEAMOD™ main platform

Figure 8. Drawings for the BEAMOD™ fluxgate sensor Helmholtz coil

Figure 9. Drawings for the BEAMOD™ SQUID sensor Helmholtz coil.

Replace with BEAMOD™ design

Figure 7 – Drawings for the BEAMOD™ main platform

Replace with BEAMOD™ design

Figure 8 – Drawings for the BEAMOD™ fluxgate sensor Helmholtz coil

Replace with BEAMOD™ design

Figure 9 – Drawings for the BEAMOD™ SQUID sensor Helmholtz coil

4. TEST FACILITIES FOR THIS PROJECT

4.1. EMIT Test Pit

As part of this project, a test facility was built at the property of ElectroMagnetic Imaging Technology Pty Ltd (EMIT), in Mundaring, east of Perth, Western Australia. A pit of width 0.7m, depth varying from 1m to 0.5m, length 2m, was dug within soil and weathered rock at a location 50m away from all buildings and power lines. It was found in profiling studies as part of this project that the soil at this site is significantly magnetic, containing iron oxides usually considered characteristic of arid climates rather than this forested and agricultural province on the outskirts of the city. We can suppose the source of lateritic material is associated with past geologic times when this region fluctuated in climate between west-coast desert type and west-coast Mediterranean type climates.

The pit is used for profiling over munitions by placing the target object on a plastic table within the pit, and covering the pit with particle board sheets. Figure 10 shows the EMIT test pit, with the BEAMOD™ Mk. 1 system and the EM63 commercial metal detector in use.



Figure 10 – BEAMOD™ Mk.1 prototype system (left) and EM63 (right) used over the EMIT test pit, Mundaring, Western Australia

The facility does not entirely duplicate the environment of buried munitions, since the pit represents a zone of free space surrounded by soil and rock.

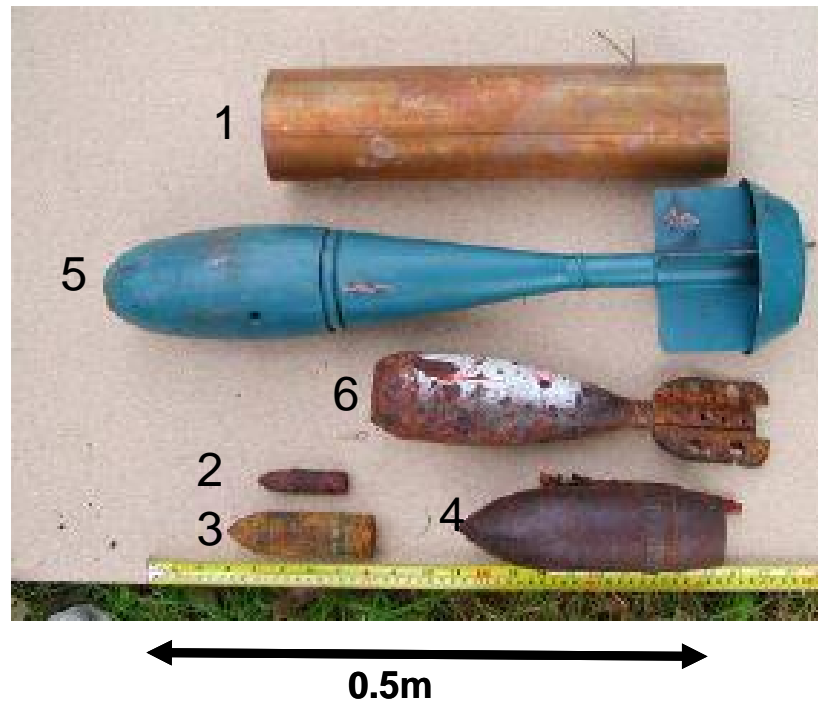


Figure 11: Targets used in studies at the EMIT test pit.

The targets used in studies at the EMIT test pit shown in Figure 11 are:

1. Copper pipe 400 mm x 100mm diameter.
2. 20 mm cannon shell, length 80 mm.
3. 40 mm cannon shell, length 130 mm.
4. 75 mm cannon shell, length 230 mm.
5. BDU-33 practice bomb, length 600 mm, diameter 100 mm (body); 150 mm (tail assembly).
6. 80 mm mortar shell, length 350 mm.

Figure 11 shows the suite of munitions targets made available to this Project by the Australian Air Force through Dr John Stanley of G-Ttek Pty Ltd (now GAP Geophysics Pty Ltd). Dr Stanley is a past and present Co-Investigator on ESTCP projects, and his cooperation with this Project has been of great value.

4.2. Newholme UXO Test Range

A series of profiles were also acquired near the close of this Project at the Newholme UXO Test Range, established at Armidale, northern NSW, Australia, by the Australian Air Force and Gtek Pty Ltd. The targets at this site range from 75 mm rocket heads (2.75 inch PWH) to Mk84 2000 lb bombs. Tests conducted at this site for this project were restricted to PWH rocket heads, BDU33 practice bombs, a 40 mm shell, and two MK82 (500lb) bombs. The smaller items are pictured in Figure 12. Detailed specifications for this site are listed in Appendix C.



Figure 12 – Targets used in studies at the Newholme UXO Test Range, Armidale NSW

1. BDU-33 practice bomb, length 600 mm, diameter 100 mm (body); 150 mm (tail assembly).
2. 75mm rocket head (2.75 inch PWH), length 400 mm.
3. 40 mm cannon shell, length 130 mm.

5. CHARACTERISATION OF B-FIELD SENSORS

5.1. Introduction: Early Tests

5.1.1. Fluxgate Sensor

Tests on the sensors have been made using a Zonge ZT-20 transmitter, which achieves a transmitter pulse turn-off of 150usec into a 10-turn transmitter loop (BEAMOD™ Mk 1, current 2.5A, moment 25 A.m²), and a transmitter turn-on pulse length of order 2000usec. The receiver used was a multi-channel EMIT SMARTem Mk 5 Receiver.

The primary field at the center of a transmitter loop used for UXO detection is typically three orders of magnitude higher than that at the center of a transmitter loop used for mineral exploration. This high field places very large linearity requirements on the sensing device, since the desired measurement of off-time decay of induced target response is perturbed if the sensor is driven into a mode of non-linear response by the strong primary fields associated with the on-time pulse.

The high primary field affects the response of the two sensors under study in different but profound ways.

Figure 11 illustrates the problems with non-linear response of the fluxgate magnetometer, seen using the sensor with no nulling coil, with an approximate nulling coil reducing the primary field by x10, and with a reversed nulling coil which increases the primary field by x2.

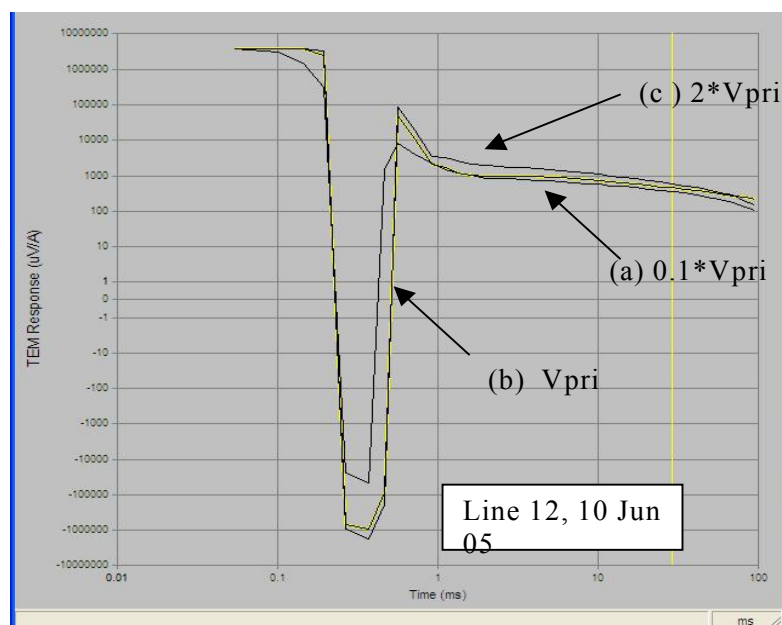


Figure 13 – Decay curve of fluxgate sensor used in BEAMOD™ Mk 1 system, over test pit, with no target.

Primary field V_{pri} from transmitter at the sensor is 28275 nT (transmitter moment 25 A.m²). Curve labeled (a) is decay curve with approximate nulling to level about x10. Yellow line (b) is decay without a nulling loop.

Curve labeled (c) is decay curve with reversed nulling loop, i.e. V_{pri} increased by x2. Responses are obviously non-linear with respect to V_{pri} .

At early times ($<0.5\text{msec}$) the sensor response rings positive-negative –positive, but the amplitude of the ringing is obviously not proportional to the primary field at the sensor. At late times ($> 10\text{msec}$) the sensor response decays exceedingly slowly, but the amplitude of this decay is not linearly related to the primary field.

The very slow decay rate and non-linear behavior of fluxgate sensor decay at late times (the decay “tail”) caused some delays in the project while possible causes were investigated. Common mode pickup in the sensor cables was considered, and eliminated as a cause by building a 3-channel differential output for the sensor electronics. The differential output made no consistent and quantifiable difference, but has been retained for subsequent use with the fluxgate sensor consistent with sound electronic design of receiver components operating in the presence of high primary fields. Another possible cause of the decay tail investigated was residual currents circulating in the transmitter coil associated with incomplete turn off of the transmitter pulse. This possible cause was studied and eliminated by monitoring the transmitter current as an additional channel in the receiver.

We conclude that the tail is an intrinsic property of the fluxgate sensor; it seems likely that it is associated with the relaxation of magnetic polarization of the fluxgate core. In the following section we show how linear behavior can be obtained after using precise primary-field nulling and further signal processing.

The fluxgate magnetometer also shows evidence of level shifts somewhat analogous to (but much less severe than) the problems experienced with the SQUID sensor. Existence of level shifts is not an expected property of the fluxgate magnetometer design, but use of the leveling algorithm described below for the SQUID sensor does provide a noticeable improvement in linearity of the response.

5.1.2. SQUID sensor

With the SQUID sensor, the major challenge for operation in the presence of high primary magnetic fields is the limitation on slew rate imposed by the RF field of the SQUID sensor electronics. The slew rate specification is 1 mT/sec , compared with the slew rate in the BEAMOD™ Mk 1 assembly of 28275nT over a transmitter turn off time of 150 usec , or 188 mT/sec . Use of the SQUID in a UXO-type EMI system without a nulling coil therefore violates the slew-rate specification by 2 to 3 orders of magnitude. When the slew rate of the primary field exceeds the specification, the RF feedback circuit within the SQUID loses lock with a resultant shift in the DC levels of the output signals for the three components of the SQUID. These shifts appear as small steps in the output signal when loss of lock is minor, but become progressively larger when slew rate is exceeded by larger margins. For high primary fields they show as large irregular drift of the DC levels over the time span of a multi-stack EM reading.

The LANDTEM SQUID on some models contains an internal shorted coil (guard coil) of 40, 80 or 160 turns which has a passive time constant in the range 0.1 to 1msec , and is designed to protect the SQUID element from the high slew rate of the primary field, at the cost of convolving (smoothing) the received field over time lengths of order 1msec . The loss of high frequency response is in some exploration applications a satisfactory compromise in order to gain the advantages

of the SQUIDS low-noise late-time or low frequency sensitivity. A series of trials were conducted using the internal guard coil, but apart from its disadvantage in degrading desired high-frequency response in the munitions application, it proves insufficient to prevent loss of lock in the high primary fields necessary, even when using an active primary field nulling coil.

Loss of lock has the property that it is a DC level shift only, with each pulse and each transient observed by the receiver suffering from a different, unpredictable but precisely DC, level shift. In consequence, this project has developed a novel processing procedure whereby each transient is level shifted back to an assumed zero level.

The SQUID sensor also suffers from a self response in this high primary-field environment, which necessitates the use of processing analogous to that developed for the fluxgate sensor.

5.2. Processing developed for BEAMOD™ sensors

A two-stage processing of time-domain EM data is found to be suited to the requirements of both the fluxgate and the SQUID sensor:

1. leveling the decay curves, essential with the SQUID for compensation of slew-rate limitations, and advantageous with the fluxgate sensor, as noted in the preceding Section, and
2. stripping the self response of the sensor from a profile of measurements.

The leveling algorithm assumes that the decay curve is sampled to sufficiently late times that the decay has reached zero. The time window where the decay is at (or assumed to be at) zero is termed the reference window. In practice, signal detected in the reference window consists of noise, and the noise level can be reduced by using a wide time range for the reference window. We use sample times 70msec to 113msec as the reference window in this study.

The effectiveness of the leveling algorithm is demonstrated on a profile of SQUID data in Figure 14. Without leveling, (Figure 14a) the profile appears meaningless. After leveling, smooth profiles are obtained for each time window (Figure 14b) although a large vertical separation exists between time channels due to the large background or self response of the SQUID sensor. After stripping the self response (Figure 14c), a meaningful set of profiles remains, which is the genuine signature of a copper pipe target placed below the test bench. The figure only shows the z-component, but the X and Y-components behave similarly, and yield, after leveling and stripping, a set of physically correct 3-component profiles for the copper pipe target (Figure 14d). The X-component shows an asymmetry in the placement of the target copper pipe (nominally horizontal, oriented parallel with the profile). The Y-component is noise only, since the target is not laterally offset from the profile.

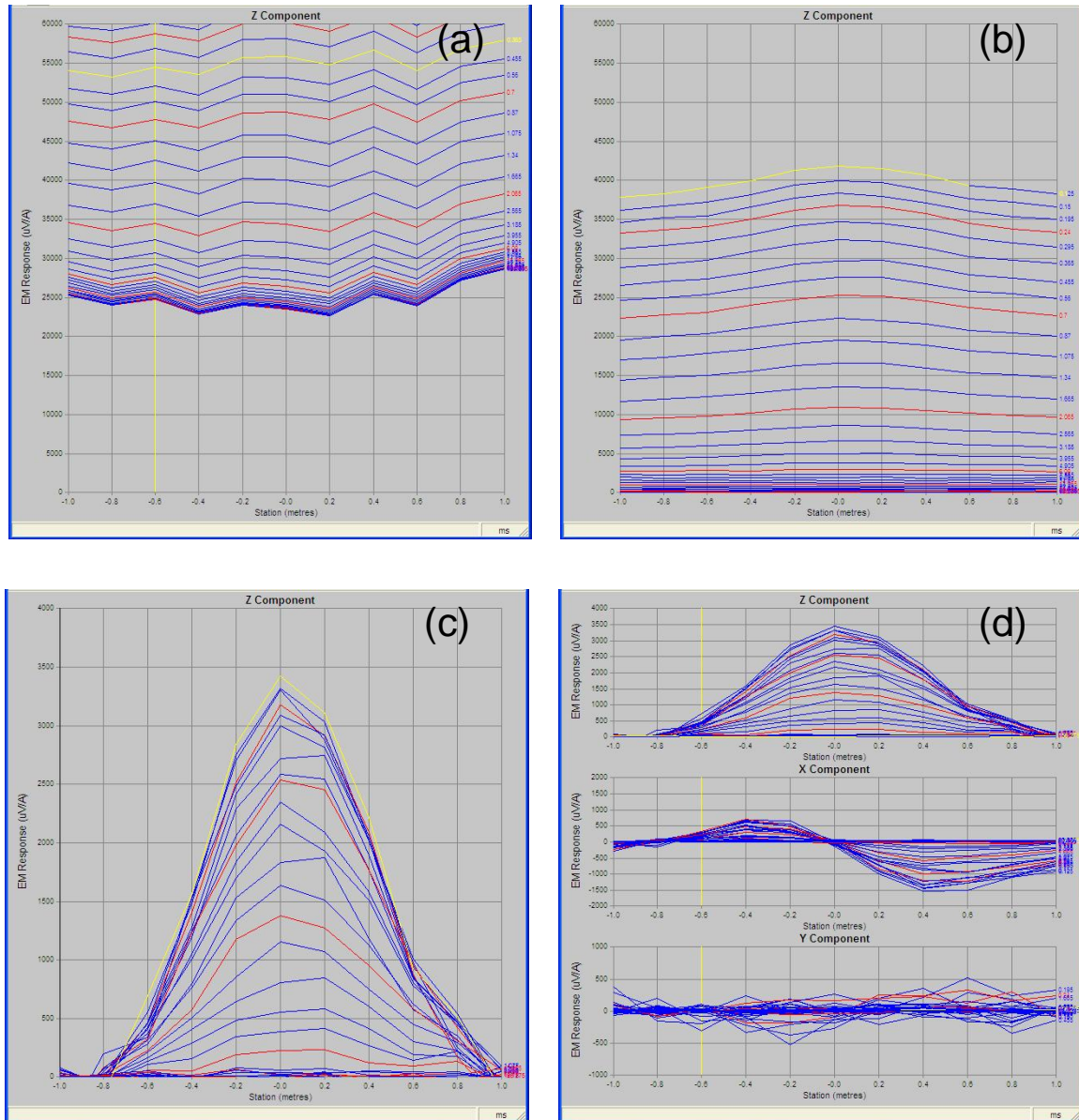


Figure 14 - The effectiveness of the leveling algorithm is demonstrated on a profile of SQUID data

- (a) Raw profile of z-component data acquired with SQUID sensor, BEAMOD™ Mk 1 on test bench, transmitter current 1 A, moment 10 A.m². The profile is heavily overprinted with a very large irregular positive shift due to SQUID loss of lock. Primary field at the sensor in the absence of nulling was 11000 nT. Primary field after nulling was 25 nT.
- (b) The leveling algorithm is applied, giving clear profiles showing anomaly signatures over a copper pipe target at depth 640 mm below the transmitter.
- (c) After application of the stripping algorithm the profiles are those expected for the target.
- (d) The three-component profile, where each component has been leveled and stripped.

The stripping algorithm is implemented by selecting one point (or a set of points) assumed to represent background, with absence of any target response, and subtracting this background from the entire profile. The stripping algorithm relies on the assumption that the self-response of the sensor is constant for each reading. This is certainly true for the profile on the test bench in Figure 14, since the transmitter and receiver were in a constant location, while the target was the item moving from point to point. However the method is also shown to be valid when

using the BEAMOD™ Mk2 system profiling across the EMIT test pit (Section 7). The weakness of the stripping process is that it cannot differentiate between a background response associated with a sensor self response, and a background response associated with geology (whether conductive or magnetic soils). Despite this limitation, the method solves the problem of sensor self response and allows the B-field sensors to be used in the high primary-field configuration of munitions detection.

It is also worth mentioning that the commercial conventional EM63 instrument also sacrifices quantitative background response for improved target response, by having a background nulling button available to the operator.

5.3. Linearity and decay of Fluxgate and SQUID sensors

Initial tests discussed in Section 5.1 showed the fluxgate sensor to lack linearity in the high primary fields of the BEAMOD™ Mk 1. The use of Helmholtz nulling coils in BEAMOD™ Mk 2 is yielding suppression of primary field by a factor between 500 and 2000. The following tests show how the hardware nulling of primary field combined with software processing using the leveling and stripping algorithms is yielding linear behavior for both the fluxgate and SQUID sensors.

Figure 15 shows decay curves for data acquired in a bench test, using three different transmitter currents. The decay curves are not similar in shape at late times, indicating that this raw data has a non-linear response. However when the data is leveled, the decay curves are seen to change linearly with respect to transmitter current. At late times (10-100msec) the decay is exponential with $\tau \sim 16\text{msec}$. It appears that the FG sensor is not able to track the strong primary field (even when using the nulling coils), with the result that the sensor output suffers a level shift at the start of the Tx offtime. The leveling algorithm corrects for this level shift.

Figure 16 repeats the comparison of leveled data from a bench test, normalized for transmitter current, and both without and with a target (copper pipe 400mm x 100mm) placed below the transmitter. In each case, normalized decay curves for the three currents coincide, confirming that over the range of currents used (1.2 to 13 A) we have linear response of the fluxgate sensor.

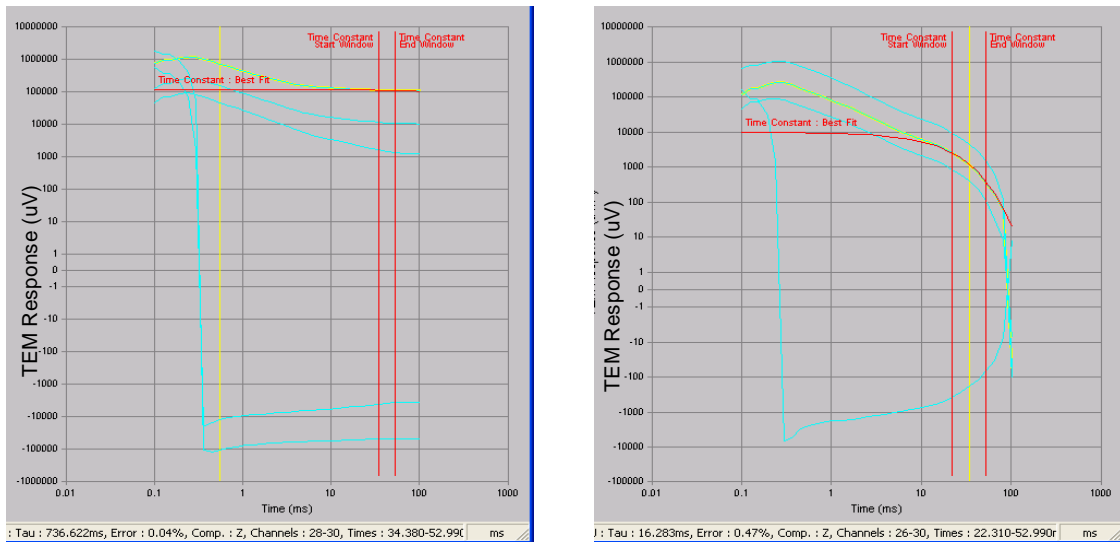


Figure 15 - Linearity test on bench of fluxgate sensor with no target
Measurement on bench, no target, using BEAMOD™ Mk 2 system [files FG401, FG402, FG403]. Data is NOT normalized for current.

LEFT: Three decay curves for raw data acquired using transmitter currents 1.2, 3.5, & 13A. Nonlinearity in this raw data is evident because the late time decay rate is different.

RIGHT: Curves are leveled (but not stripped). Note the curves are shifted by a constant multiplier (the Tx current) so the process is linear.

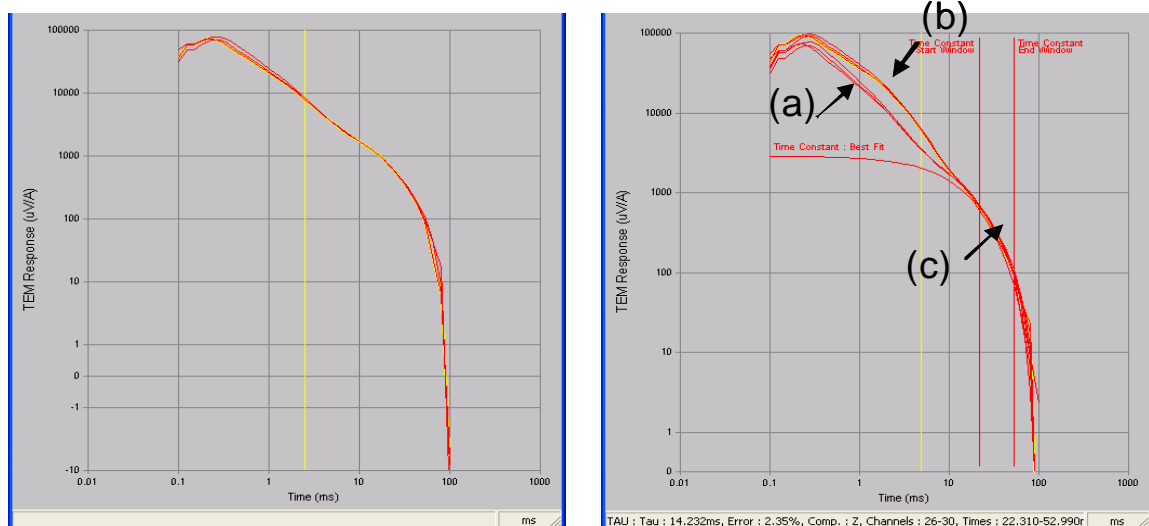


Figure 16 - Linearity test on bench of fluxgate sensor with and without a target
Measurement on bench, using BEAMOD™ Mk 2 system, with transmitter currents 1.2, 3.5 & 13A (giving transmitter moments 18, 52, 195 A.m²; primary fields 2E4, 5.9E4, 2.2E5 pT). Target is copper pipe placed 640 mm below transmitter [files FG401, FG402, FG403].

LEFT: The three leveled decay curves (without target) from Figure 15 are normalized for transmitter current, and confirm the match noted in Figure 15.

RIGHT: Curves (a) duplicate the three curves without a target. Curves (b) are the corresponding three decay curves with the target in place below the sensor. At late times (> 20 msec) all curves merge (labeled (c)); this is a system response associated with the fluxgate sensor in the large transmitter field. This system response shows a fitted exponential decay of order tau=15msec, and exists regardless of the location of the instrument, or the presence of a target.

(c) The three leveled decay curves are normalized for transmitter current; confirm the match in (b).

Figure 17 shows the superposition of leveled fluxgate responses over the copper target, after stripping the background sensor self response. The normalized, leveled, stripped curves overlay until the onset of noise at time window 15msec, and a fitted exponential curve shows a time constant for the target of 2.2msec, which is the same as the decay observed for this target when using a coil sensor and the EM63 instrument. We conclude that both the leveling and stripping algorithms are demonstrating linearity of processed fluxgate magnetometer output with respect to transmitter current.

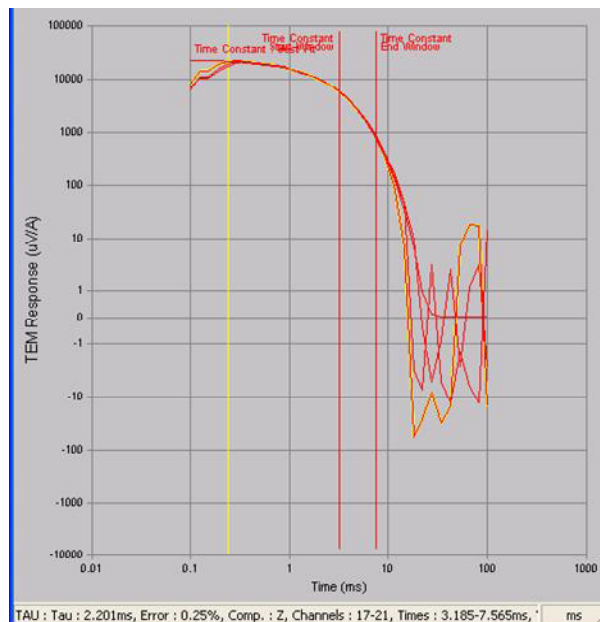


Figure 17 - Superimposed leveled normalized decay curve responses from Figure 16, for three transmitter currents, with the fluxgate sensor over the copper pipe target

Figure 18 and

Figure 19 show the results of a similar linearity test using a SQUID sensor within the Helmholtz nulling coils. The figures demonstrate excellent linearity of the SQUID sensor after processing with the leveling and stripping algorithms. They also show two important differences between the SQUID and fluxgate sensors:

1. clean matching curves down to the earliest sample time, reflecting the wider bandwidth of the SQUID sensor (DC to 10 KHz, compared with DC to 3 KHz for the fluxgate sensor), and
2. matching curves to later time due to lower noise of the SQUID sensor. The following Section quantifies the difference in noise of the two sensors.

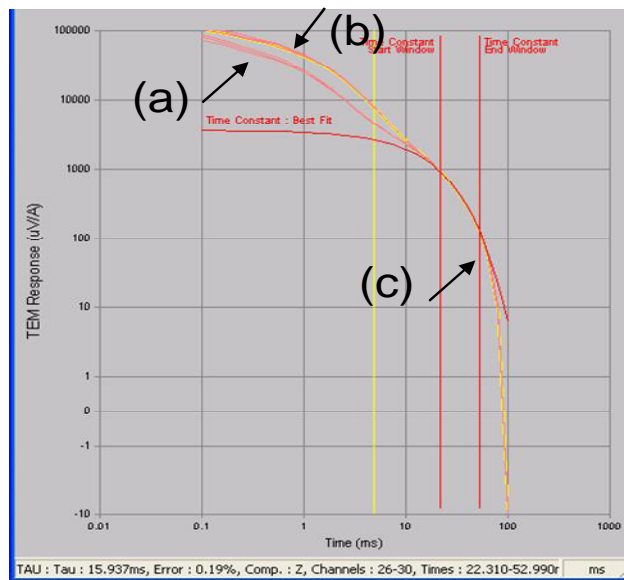


Figure 18 - Linearity test on bench of SQUID sensor with and without a target Measurement on bench, using BEAMOD™ Mk 2 system, with transmitter currents 1.2, 3.5, & 9A (giving transmitter moments 18, 52, 135 A.m²; primary fields 2E4, 5.9E4, 1.5E5 pT). Target is copper pipe placed 640 mm below transmitter [files SQ400, SQG401, SQ402]. Curves (a) are normalized leveled decay curves acquired without a target, at the three transmitter currents. Curves (b) are the corresponding three decay curves with the target in place below the sensor. At late times (> 20msec) all curves merge (labeled (c)); this is a system response associated with the SQUID sensor in the large transmitter field. This system response shows a fitted exponential decay of order tau=15 msec, and exists regardless of the location of the instrument, or the presence of a target.

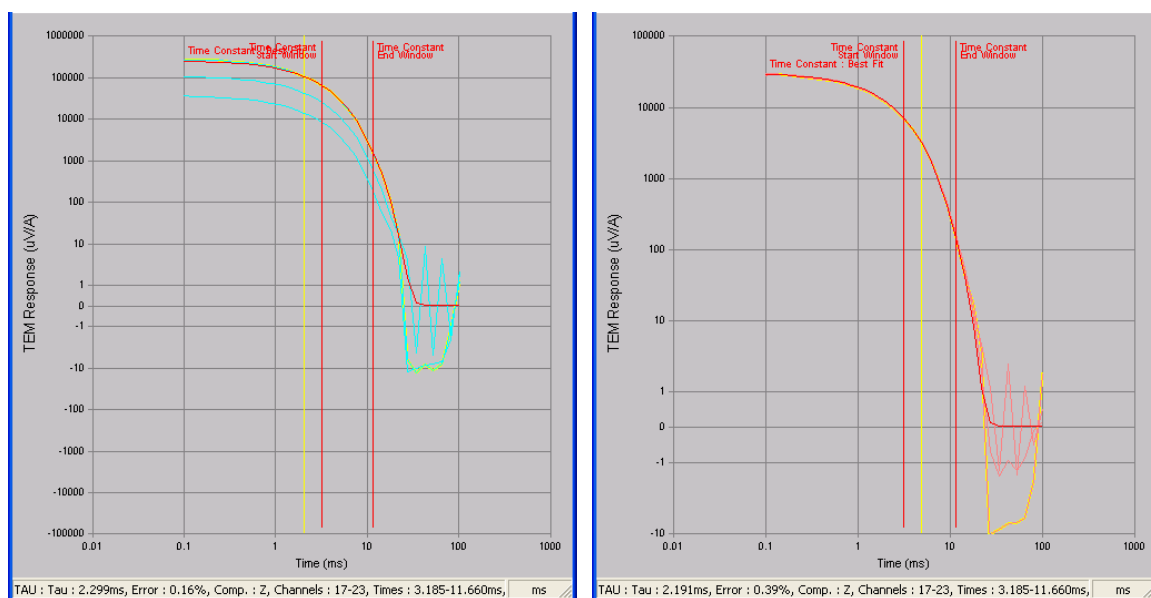


Figure 19: Superimposed leveled and stripped decay curve responses from Figure 18, for three transmitter currents, with the SQUID sensor over the copper pipe target

LEFT: The curves are not normalized for current (facilitates assessment of noise levels). The red curve is a fitted exponential curve, where the fit is quite exact and obscures the observed decay curve underneath.

RIGHT: The curves are normalized for transmitter current and overlay very closely. The fitted exponential decay curve has tau=2.2 msec.

5.4. Algorithm for assessing noise level in presence of signal

For practical EMI instruments, noise can take four forms:

1. Intrinsic or internal noise associated with sensor and data logger electronics,
2. Noise associated with external geomagnetic or cultural magnetic field variations,
3. Noise associated with change in geological background obscuring a target response along a profile, and
4. Noise produced by motion of the sensors in the Earth's magnetic field during a moving-system profile.

No comparative noise study can expect to be successful without recognizing and separating out these four independent sources of noise. The task is further complicated by the fact that external geomagnetic noise (typically associated with spheric activity in the atmosphere) varies through the day and by an order of magnitude from the winter (low) to summer seasons (high) through the year (McCracken et al, 1986).

Noise associated with “geological change” along a profile may in general also include variations associated with movement and re-positioning of sensors. We seek a method of showing point-to-point noise, while recognizing that geological background and variation produces trends of low spatial frequency as well as point-to-point noise. In order to separate point-to-point noise from trends we use a roughening or high-pass filter on profiles. The filter we use is a high-pass filter generated by using a 5-point Hanning bell convolution filter to smooth the data, followed by subtraction of the smoothed curve from the original. The process is first illustrated on synthetic pure Gaussian noise in Figure 20. Curve (a) is of sufficient length such that the computed RMS amplitude (shown at top of graph) converges to be close (2.1) to the theoretical value (2.0) used to generate the random number sequence. Curve (b) is the same data after application of the roughening filter. The computed RMS is reduced due to loss of low frequency energy, but the loss is a constant factor which is a function of the shape of the filter; in this case the factor is 1.32. This factor remains constant regardless of how many points are used in the input noise sequence.

Figure 20 (c) and (d) show a 15-point Gaussian noise sequence before and after application of the roughening filter. The choice of 15 points is made to correspond with several profiles of observed data discussed in Sections 5.5-5.7. Curve (e) shows the same noise sequence with addition of a bell-shaped “signal” of amplitude 12 units (analogous to the shape of a munitions EM anomaly). Curve (f) shows the effect of applying the roughening filter to (e). It is seen that the estimate of RMS noise is closely similar to that in (d), which demonstrates how use of the roughening filter allows estimation of RMS noise from data sequences which contain a target signal or trend.

The roughening filter is applied to examples of observed data which contain a target anomaly, in Section 5.7.

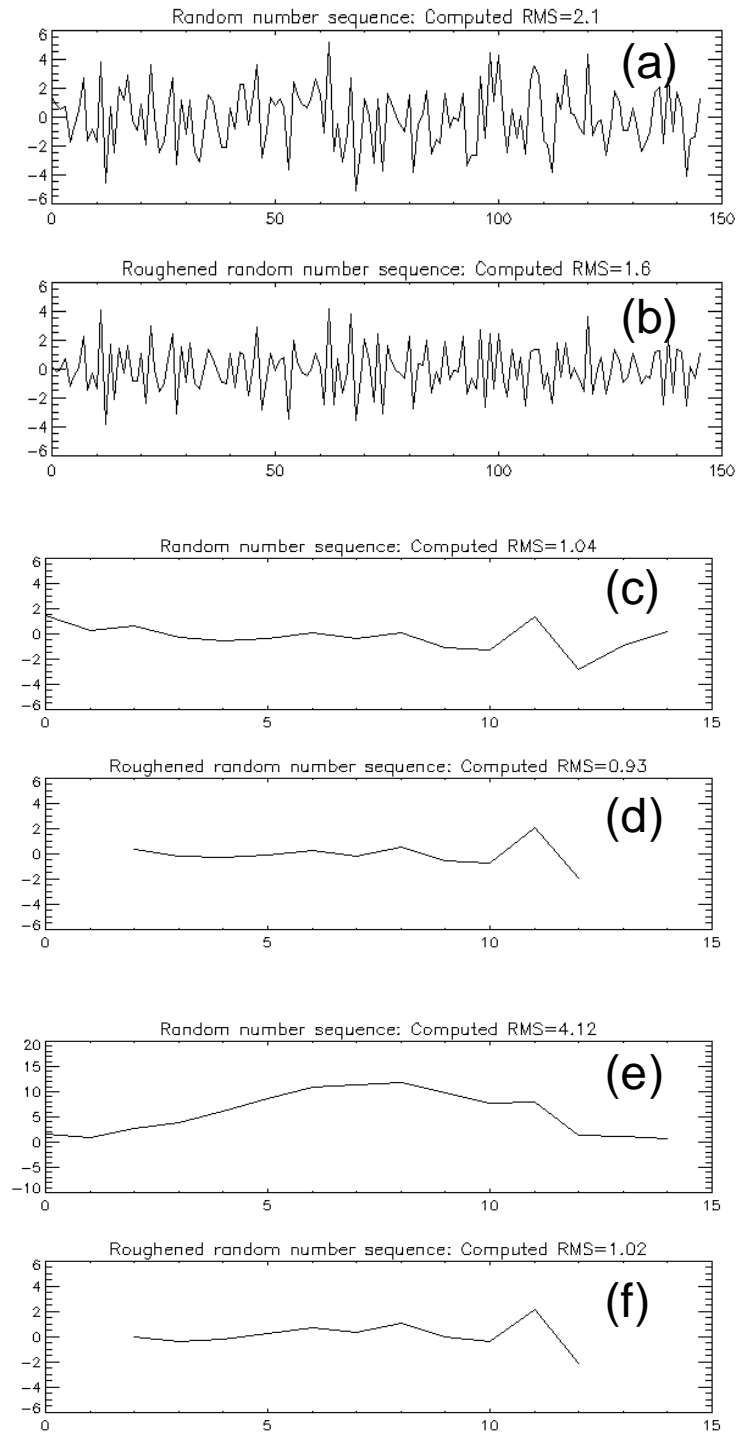


Figure 20: The process of for assessing Gaussian noise level in the presence of a synthetic signal
 (a) Synthetic Gaussian noise of length 150 points, generated using mean zero and rms 2.0.
 (b) Data from (a) after application of roughening filter.
 (c) Synthetic Gaussian noise of length 15 points, generated using mean zero and rms 2.0.
 (d) Data from (c) after application of roughening filter.
 (e) Synthetic Gaussian noise from (c) with bell curve of amplitude 12 units added.
 (f) Data from (e) after application of roughening filter.

A key requirement when using the specified 5-point roughening filter is that the computed RMS must be increased by the factor 1.32 in order to correspond with

an RMS estimate computed on pure Gaussian noise; the effect of this is seen in Figure 21 and Figure 22 where RMS noise is shown computed both by use of the roughening filter, and on raw data, with closely similar results.

5.5. Intrinsic Noise Level: Fluxgate and SQUID Sensors

Intrinsic noise levels of each sensor as used with the time-domain EM SMARTem recorder were estimated in Figure 21 and Figure 22 by placing the sensor in a mumetal shield and recording noise levels for a sequence of 15 readings, each of 64 “stacks” (with the transmitter off).

The behavior of white noise after windowing and stacking in a time-domain EM system is considered by McCracken et al (1986). They show that

$$\text{variance} = S_o / 2Ns,$$

where S_o is spectral density, N is the number of stacks, and s is the time window width. In order to compare noise across different time-domain EM systems, differing stacking rates and window widths must be considered. In this work we have opted firstly to present noise data in picoTesla (pT) RMS in each time window for the BEAMOD™ system, for 64 stacks as observed in measured data (See Section 3.7 for a listing of time windows). Secondly, we present RMS noise data for each window multiplied by the square root of the window width, which has the advantage that noise figures can be directly compared with noise obtained with any other set of windows in a time-domain EM system using the same number of stacks. The resulting unit of noise is $\text{pT} \cdot \sqrt{\text{sec}}$ or $\text{pT} \cdot \text{rtsec}$, and is dimensionally equivalent to the familiar noise unit of “amplitude per root Hz” commonly used for frequency-domain descriptions of noise. We have not attempted to normalize for stacking since we have no information on the stacking algorithm used in one of our systems under study (the EM63). All noise studies performed with the BEAMOD™ system use reading acquired with 64 stacks.

It is immediately obvious from a comparison of Figure 21 and Figure 22 that the SQUID has an intrinsic noise level a factor of 10 lower than the fluxgate sensor, across the entire spectrum of interest, for data samples of the same length in time (64 stacks).

5.6. Survey Noise Level: Environmental at EMIT Test Pit

Figure 23 and Figure 24 show noise for the two sensors recorded by moving them in a profile over the EMIT test pit, but with the transmitter off. These profiles are thus a measure of intrinsic plus environmental noise, plus any instrumental instabilities associated with repeated movement of the sensors. It is not possible to be definitive about the relative noise levels of the two instruments since these two data sets were acquired two days apart, opening the possibility that geomagnetic noise could be different at the two measurement times. Having stated that uncertainty we note that the fluxgate noise is a factor of about three above the intrinsic noise level, and the SQUID noise level a factor of 10 above the intrinsic noise level, giving the SQUID a noise advantage for these observations, across all time windows, of about 3.5.

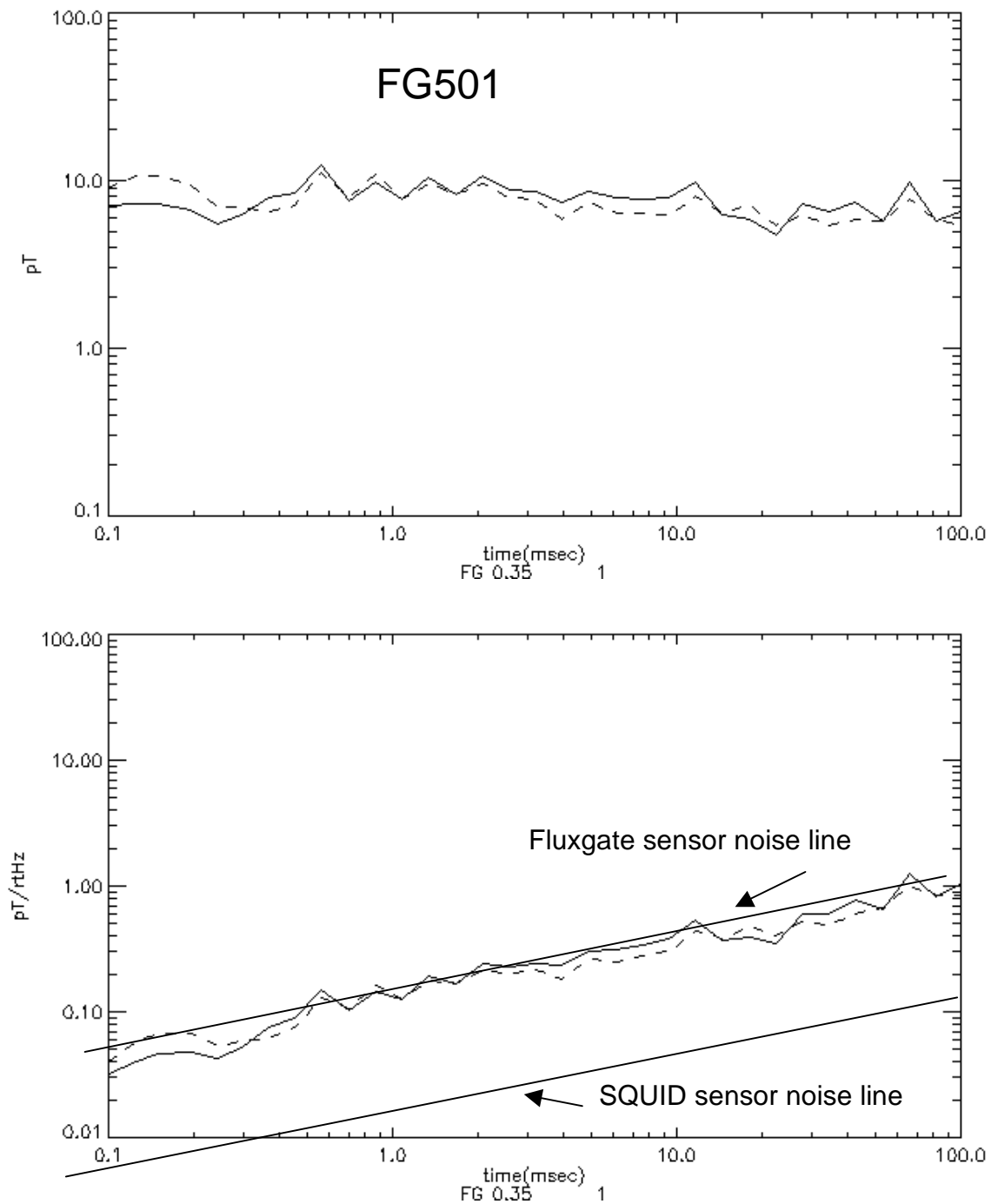


Figure 21: Intrinsic noise of fluxgate sensor measured in mumetal shield, using BEAMOD™ time windows, no transmitter

TOP: RMS noise in pT in each time window, for 64 stacks.

BOTTOM: RMS noise normalized for time window width, into units of $\text{pT} \cdot \sqrt{\text{sec}}$.

Solid line: noise computed from roughened profile as described in text.

Dotted line: noise computed from raw data.

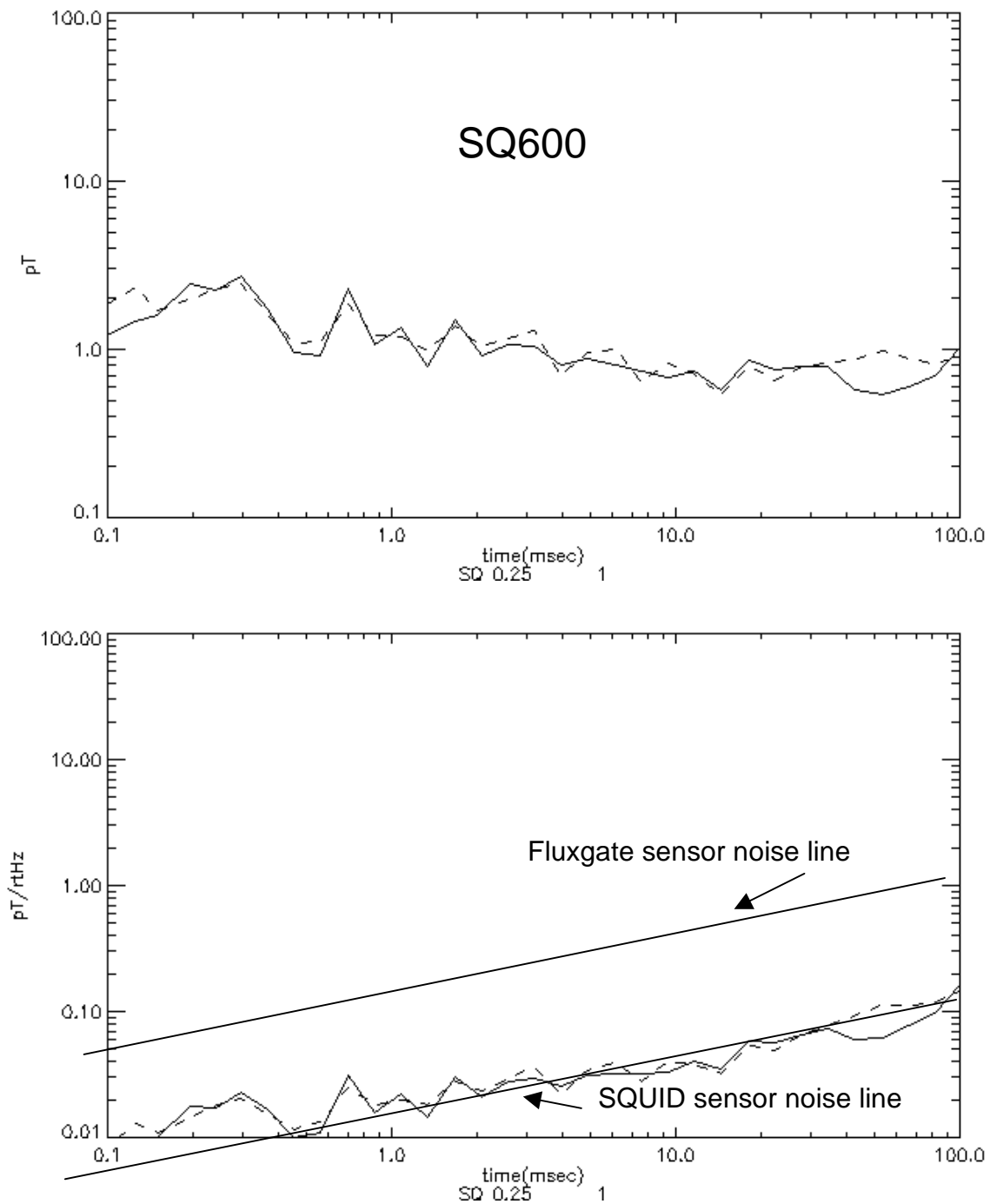


Figure 22: Intrinsic noise of SQUID sensor measured in mumetal shield, using BEAMOD™ time windows, no transmitter

Note that intrinsic noise of the SQUID sensor is close to a factor of 10 lower than that for the fluxgate sensor.

TOP: RMS noise in pT in each time window, for 64 stacks.

BOTTOM: RMS noise normalized for time window width, into units of $\text{pT}/\sqrt{\text{sec}}$

Solid line: noise computed from roughened profile as described in text.

Dotted line: noise computed from raw data.

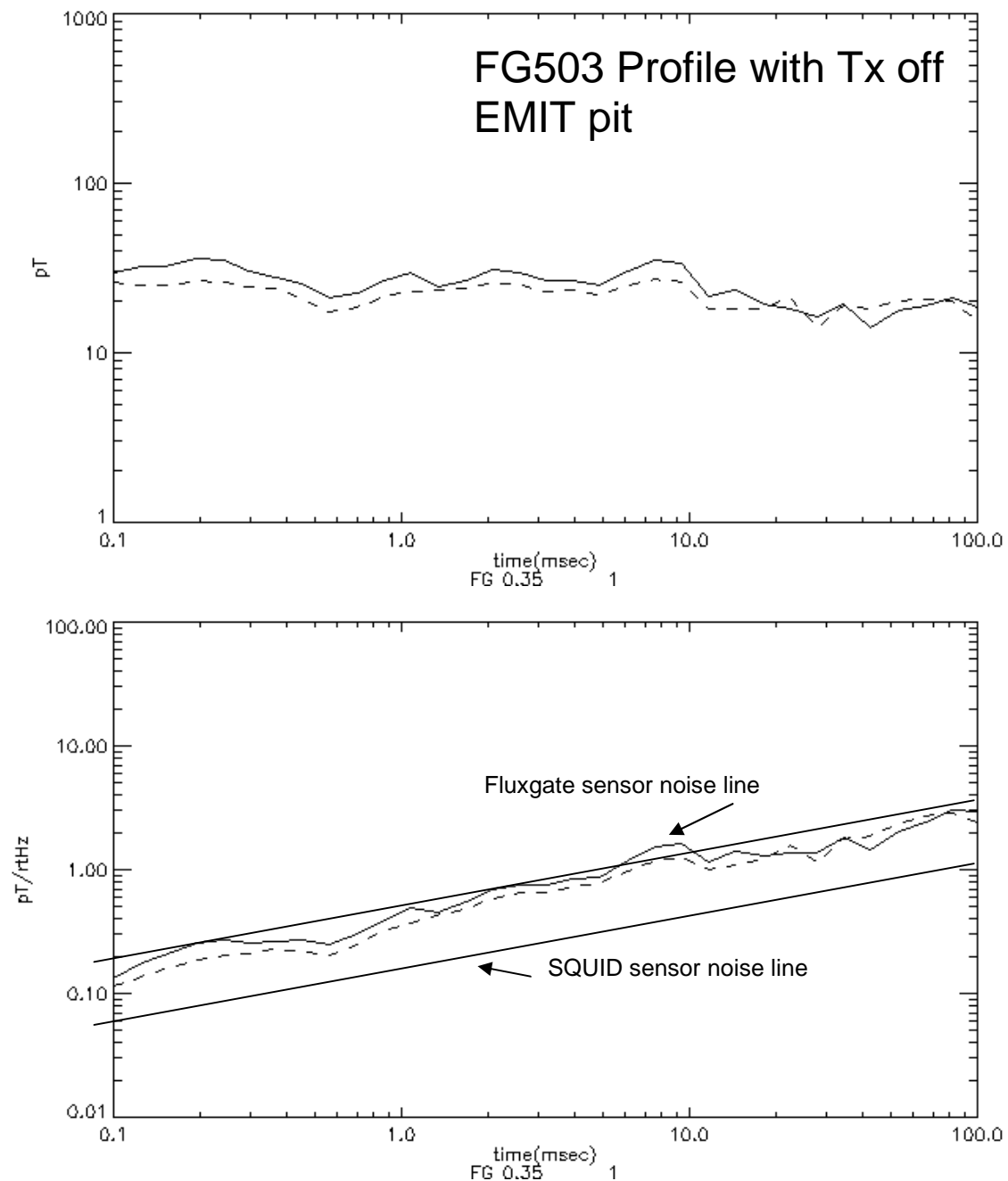


Figure 23: Noise of fluxgate sensor in a 4 m profile of 15 points over EMIT test pit, using BEAMOD™ time windows, no transmitter
 TOP: RMS noise in pT in each time window, for 64 stacks.
 BOTTOM: RMS noise normalized for time window width, into units of $\text{pT} \cdot \sqrt{\text{sec}}$
 Solid line: noise computed from roughened profile as described in text.
 Dotted line: noise computed from raw data.

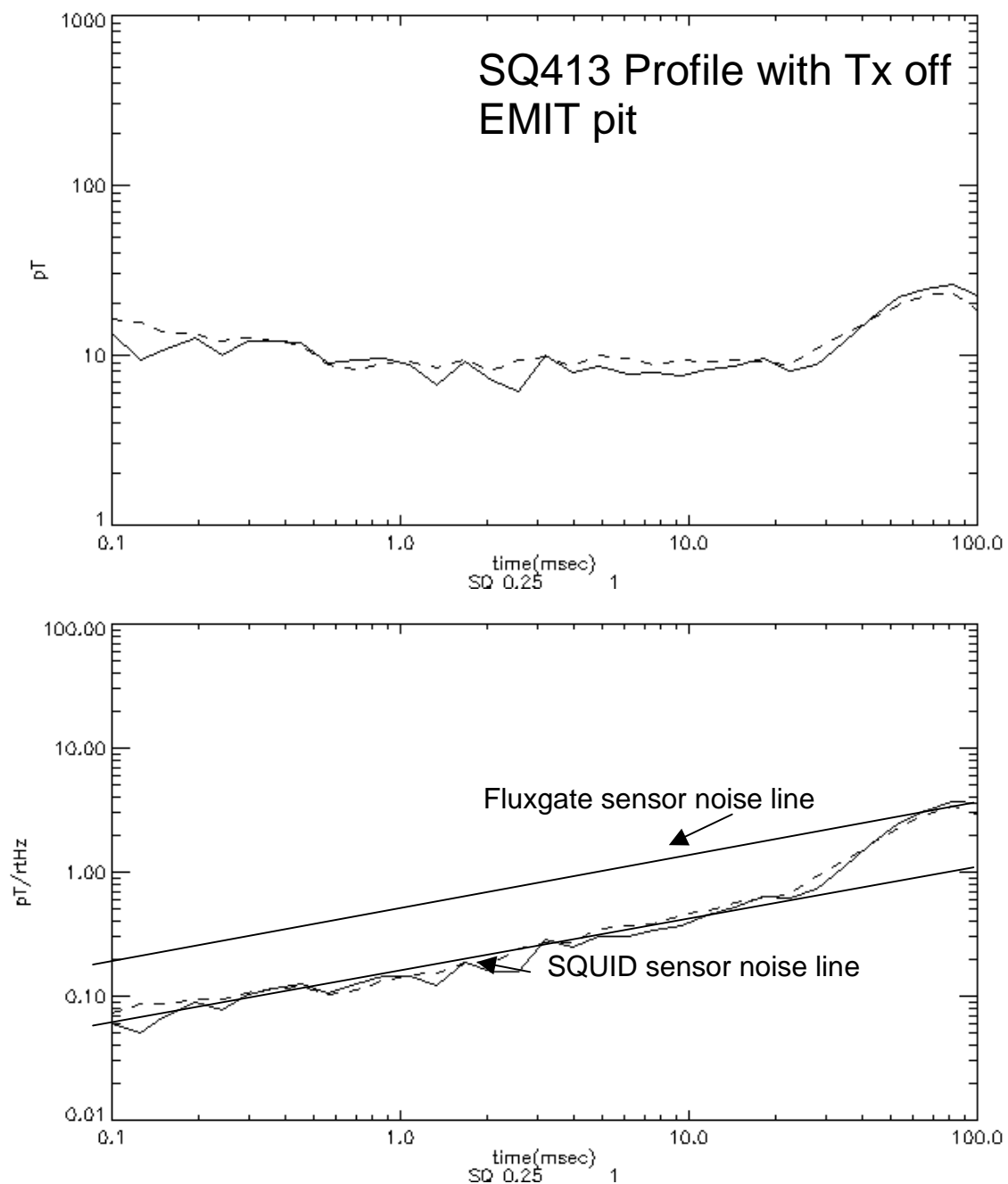


Figure 24: Noise of SQUID sensor in a 4 m profile of 15 points over EMIT test pit, using BEAMOD™ time windows, no transmitter
Environmental noise including set-up variations for the SQUID sensor is lower than that for the fluxgate sensor by a factor of about 3.5.

TOP: RMS noise in pT in each time window, for 64 stacks.

BOTTOM: RMS noise normalized for time window width, into units of $\text{pT}/\sqrt{\text{sec}}$

Solid line: noise computed from roughened profile as described in text.

Dotted line: noise computed from raw data.

5.7. Survey Noise Level: Environmental at EMIT Bench Test

Another comparison of instrumental and environmental noise observed by the two B-field sensors can be made from bench tests, where profiles of target response were obtained on a test bench using a moving target object below the bench. The

transmitter and receiver were held stationary, thus keeping background geological signal constant. Variation from point to point is therefore attributable to instrumental and environmental noise, excluding geological noise. By using the roughening filter as described above to attenuate the target response and extract an estimate of point-to-point noise we obtain the comparison of instrumental noise shown in Figure 25 to Figure 28.

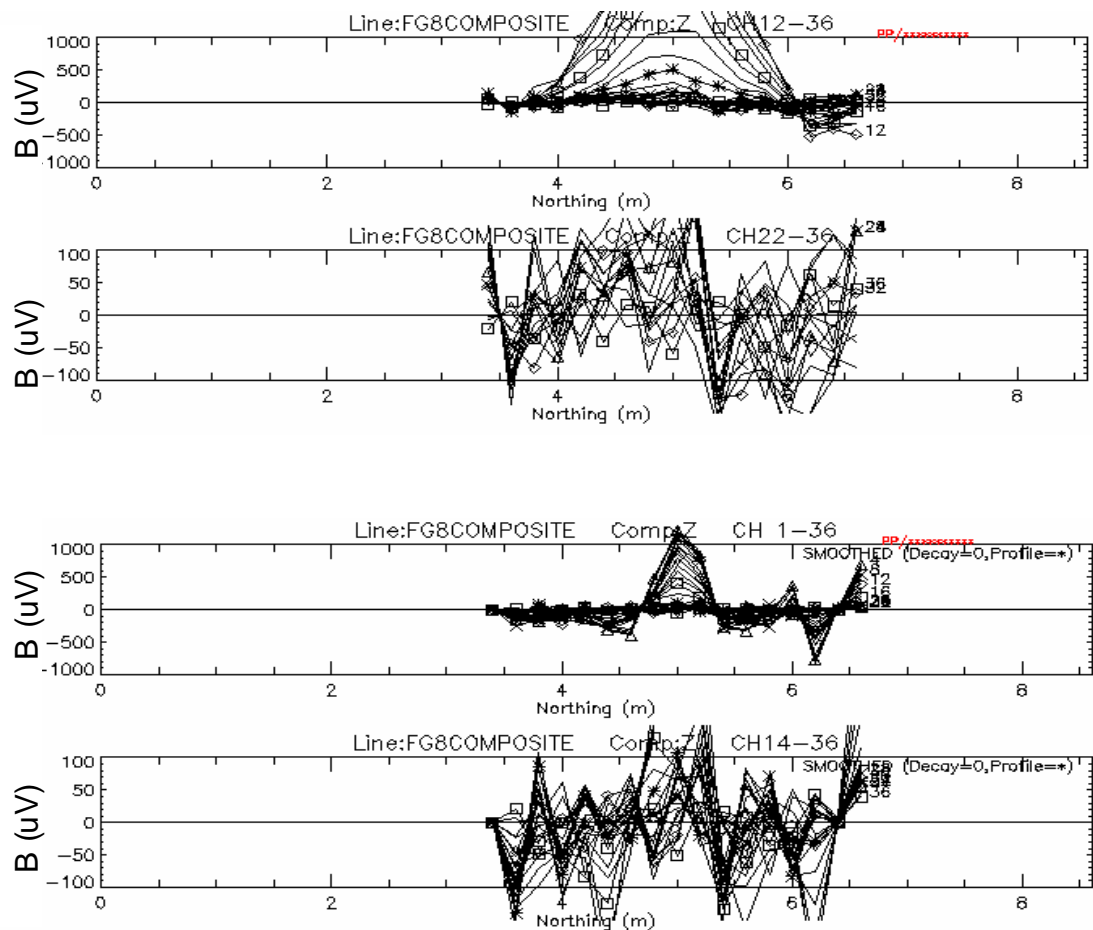


Figure 25: Estimation of noise in profile over the EMIT test pit, fluxgate sensor.

Top pair of plots: Z-component profiles of 15 points over length 2 m using fluxgate sensor, EMIT test bench, using BEAMOD™ time windows, BEAMOD™ Mk 1 transmitter, current 1A, fluxgate sensor, 64 receiver stacks. The target was a copper pipe 400mm x 100mm, oriented vertically, top 560mm below the transmitter. Profiles show a target signature for channels 12-20, with target signal submerged in noise for channels 22-36.

Lower pair of plots: Roughened profiles which remove the low-frequency spatial variation of the target response, and allow RMS noise to be computed from point to point variations.

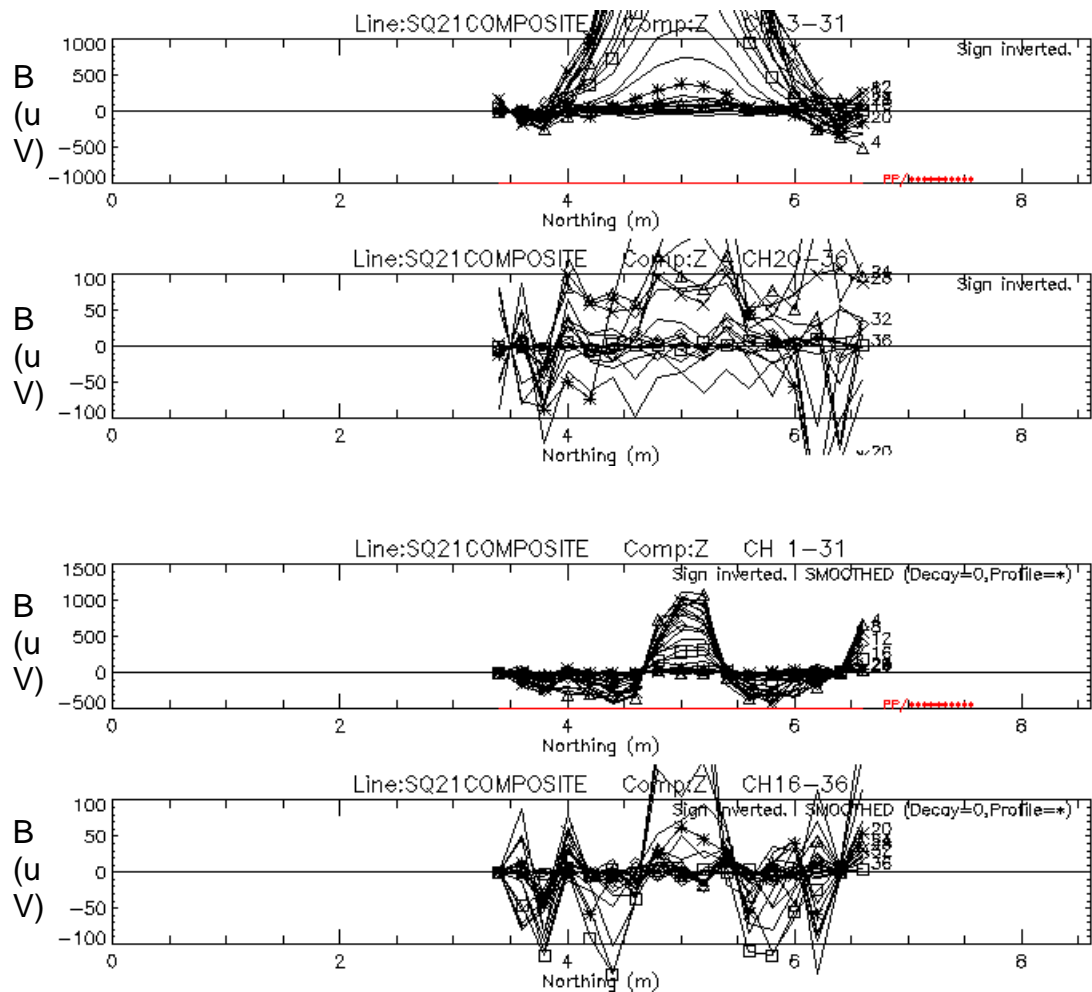


Figure 26: Estimation of noise in profile over the EMIT test pit, SQUID sensor.

Top pair of plots: Z-component profiles of 15 points over length 2 m using SQUID sensor, EMIT test bench, using BEAMOD™ time windows, BEAMOD™ Mk 1 transmitter, current 1A, SQUID sensor. The target was a copper pipe 400mm x 100mm, oriented vertically, top 560mm below the transmitter. Profiles show a target signature for channels 12-20, with target signal submerged in noise for channels 22-36.

Lower pair of plots: Roughened profiles which remove the low-frequency spatial variation of the target response, and allow RMS noise to be computed from point to point variations.

It is evident from Figure 25 and Figure 26 that the roughening filter is not perfect in its suppression of target signal in early time channels, but the comparison between performances of the two sensors is still very useful.

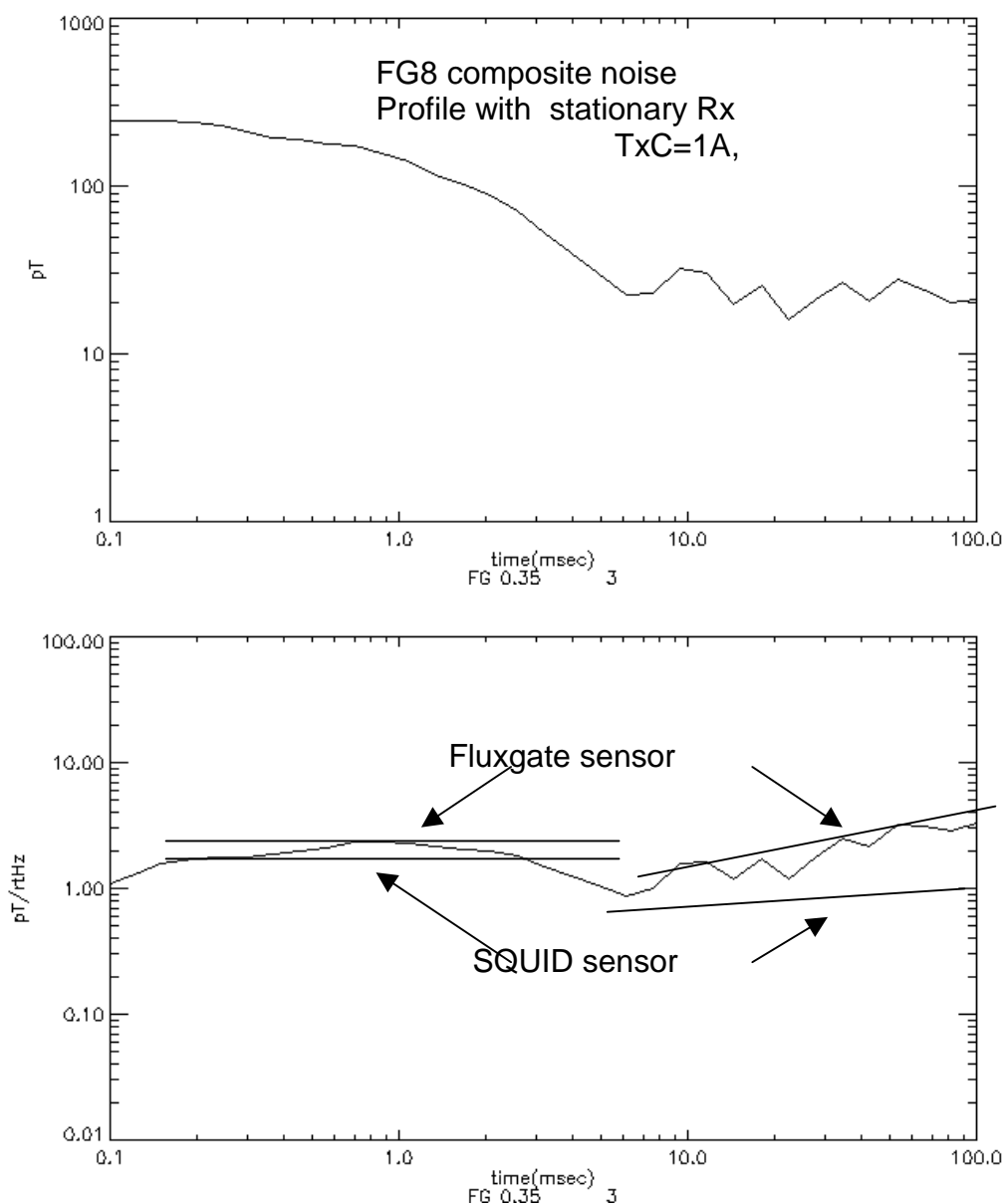


Figure 27: Noise of fluxgate sensor in the 2m profile of Figure 25

TOP: RMS noise in pT in each time window, for 64 stacks.

BOTTOM: RMS noise normalized for time window width, into units of $\text{pT} \cdot \sqrt{\text{sec}}$

Noise computed from data which has been leveled, stripped, and roughened as described in text.

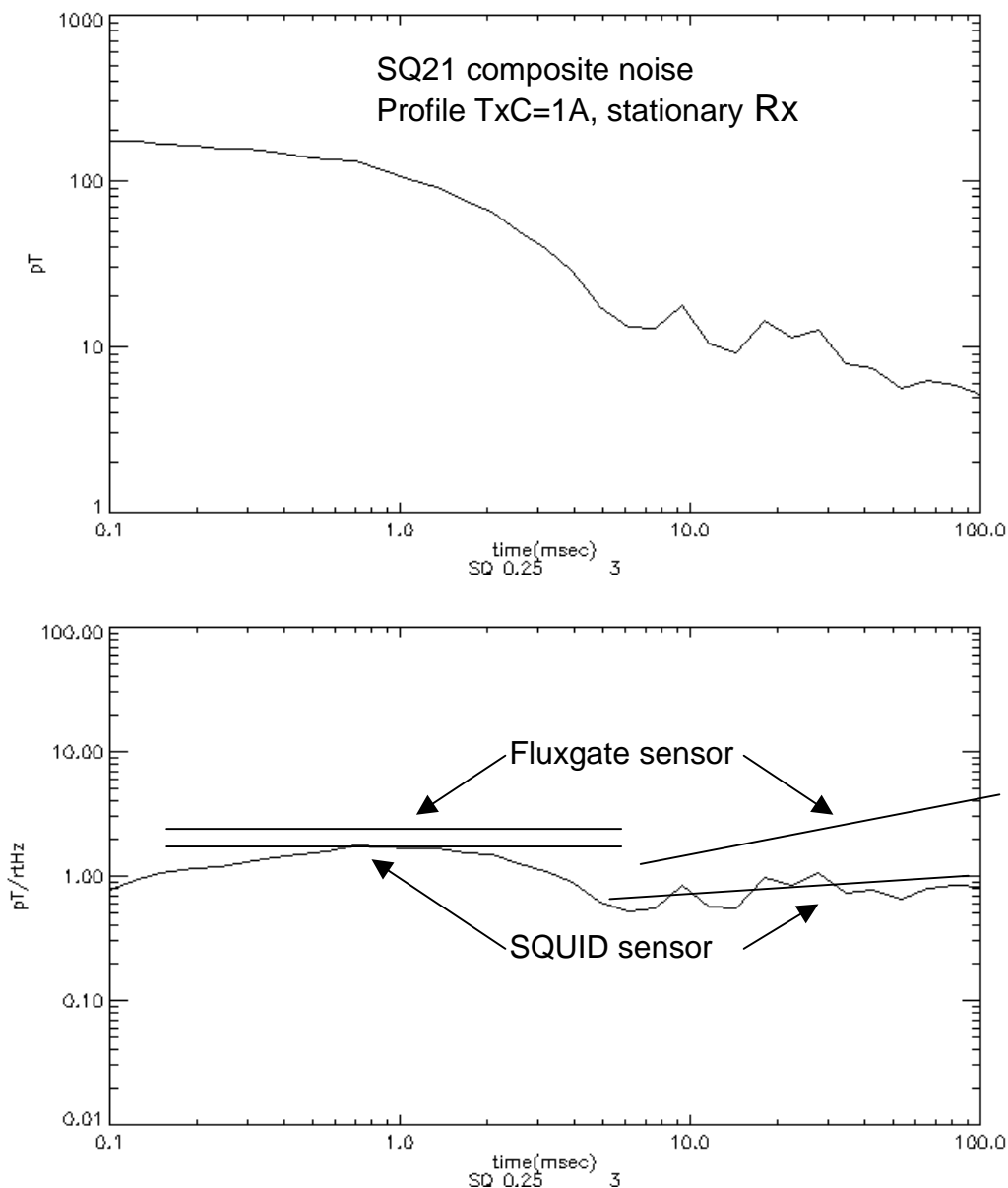


Figure 28: Noise of SQUID sensor in the 2m profile of Figure 26

TOP: RMS noise in pT in each time window, for 64 stacks.

BOTTOM: RMS noise normalized for time window width, into units of $\text{pT} \cdot \sqrt{\text{sec}}$

Noise computed from data which has been leveled, stripped, and roughened as described in text.

Figure 27 and Figure 28 show noise in pT and also in $\text{pT} \cdot \sqrt{\text{sec}}$ for the two sensors used in the two previous figures. It is evident that for early and mid time channels (0.1-5 msec) the SQUID has a noise advantage below a factor of 2, while at later times (10-100msec) the SQUID noise advantage is between 2 and 4.

While the comparative noise figures have to be qualified recognizing that the two profiles were acquired on successive days (geomagnetic noise can and does change from day to day), and recognizing that at early times the roughened profiles still contain part of the target signature, we can conclude that the noise advantage of the SQUID for this test lies in the range 2 to 5, which is consistent with the factor of 3.5 obtained in separate tests conducted over the EMIT test pit section 5.6).

5.8. Consequences of slew rate, noise and linearity studies on B-field sensors

Both the fluxgate and SQUID sensors have demonstrated linearity in the BEAMOD™ Mk 2 transmitter with transmitter currents in the range 1.2-13A (transmitter moments 18 to 195 A.m², or primary fields in the range 20,000 to 220,000 pT). Linearity is conditional on the use of the hardware bucking field via the Helmholtz coils, together with the software leveling and stripping algorithms described in Section 5. However the irregular level shifts in SQUID receiver output, which are a consequence of loss-of-lock in the SQUID feedback circuit and the slew-rate limitation of the sensor, become excessive when transmitter currents exceed 3.5A; the zero level of the off-time decay frequently drifts out of range of the receiver electronics in the time span of a single reading (about 20 sec). While this drift and ranging problem could be addressed with re-design of SQUID electronics, such changes are outside the scope of this project where authorized tests extend to use of a rental unit only. The consequence is that SQUID observations over munitions targets with BEAMOD™ Mk 2 are limited to transmitter currents of 3.5A (transmitter moments of 52.5 A.m²). By contrast, the fluxgate sensor is able to operate at 12A transmitter current (transmitter moment 195A) without drift (higher currents may be possible but would require heavier transmitter wire) and so when the two sensors are compared we have the following trade-offs:

1. Fluxgate advantage: operates stably at a transmitter moment x3.4 larger than SQUID,
2. SQUID advantage: lower noise in profile applications by factor of order 2 to 5.
3. SQUID advantage: wider bandwidth, DC to >10kHz.

In addition the fluxgate sensor has advantages of being

4. A factor x26 cheaper than the SQUID (\$6000 vs \$160,000, although very large reductions in SQUID costs can be expected if multiple units were to be ordered for BEAMOD™ use), and
5. The fluxgate sensor is physically smaller and physically more robust (does not require a Dewar vessel or use of liquid nitrogen on site).

The first two trade-offs basically cancel since the higher noise of the fluxgate sensor can be compensated by use of higher transmitter moments. The second two trade-offs clearly favor the use of the fluxgate sensor for future trials.

The SQUID advantage of wider bandwidth remains, but since the BEAMOD™ concept using B-field sensors is targeted primarily at discrimination using longer decay times on larger types of munitions, the SQUID bandwidth advantage is not of immediate value.

Our recommendation is therefore to continue development of the BEAMOD™ system using fluxgate magnetometers as the B-field sensors of choice.

6. EM63 RESULTS OVER TEST PIT

6.1. EM63 Transmitter and Receiver Moments and Waveform

Figure 3.1 shows the EM63 instrument in use over the EMIT test pit. Fig.5.1 shows the geometry of the instrument hired for this Project from Geonics Ltd, Mississauga, Ontario.

EM63 GEOMETRY

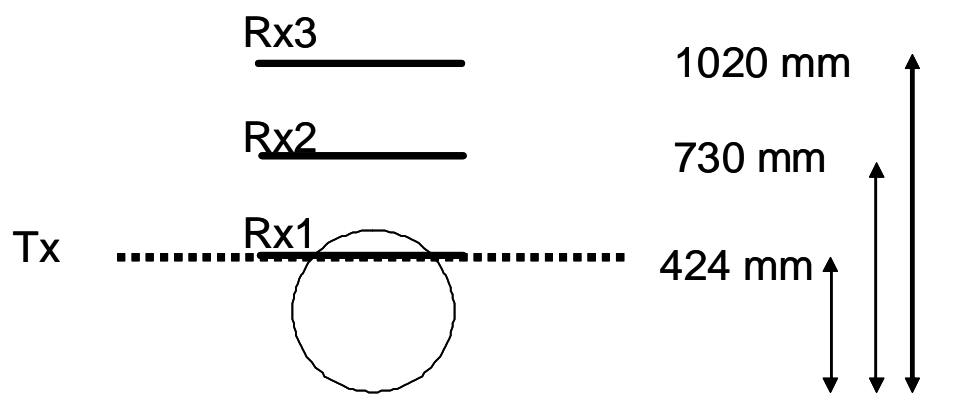


Figure 29 Side view schematic diagram showing the geometry of the EM63 metal detector with transmitter and receiver coils above ground level

Transmitter coil Tx is 1m x 1m. Receiver coils Rx1, Rx2, Rx3 are 0.5 x 0.5m.

Transmitter and receiver specifications are not given by manufacturer and may vary between different units.

Peak transmitter moment of unit rented was measured at 445 A.m²

Receiver units are given by instrument in mV. Estimate of receiver effective area (turns x area x amplification) on the rented unit is 1000000m². (Divide EM63 reading by 1000 to convert from mV to pT/s).

Specifications of the EM63 are not provided by the manufacturer. On the rented instrument, the transmitter peak moment was measured at 445A.m² by use of a fluxgate magnetometer sensor in near vicinity. The receiver effective area (turns x area x amplification) was estimated as 1000000 m² using the inductive limit response of the system over a copper target of known area. Time windows from the lowest coil only are used in this project; the upper coil provides only a single time window in the available rented instrument.

Figure 30 and Figure 31 show the transmitter observed waveform as measured with a separate fluxgate magnetometer as receiver in near vicinity. Note that the waveform is unusual in that positive and negative transmitter pulses are asymmetrical and of unequal length; we do not know the reasons for this.

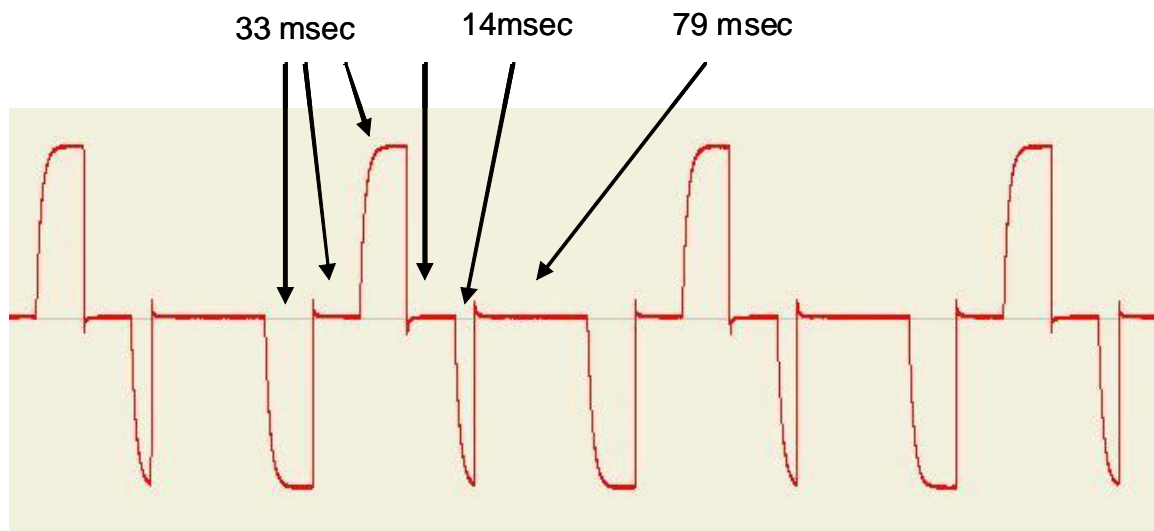


Figure 30 EM63 waveform – At 50 Hz power line setting and M frequency, measured base frequency was 4.5 Hz

At frequency M (medium) and 60 Hz power line setting, waveform frequency = 4.42 Hz = period of 226msec



Figure 31: EM63 waveform – At 50 Hz powerline setting and H frequency, repetition frequency of the waveform is at 30 Hz while turned on – 8.333 msec +/-off/-off

The complete cycle including the blank time takes 0.191 seconds – a fundamental rate of 5.23 Hz. The duration of the blank time is 85 msec.

The time windows used by the EM63 are listed in Table 2 below. They are similar to the set used by the BEAMOD™ system (Section 2.6), but are restricted to a maximum delay time of 25msec.

Table 2 – Time Windows (33 time windows when using a 2.08 Hz Transmitter Frequency)

EM63 time windows	(in msec)
Centre	Width
0.177	0.033
0.191	0.024
0.216	0.033
0.246	0.033
0.286	0.053
0.336	0.073
0.400	0.082
0.480	0.102
0.584	0.131
0.714	0.151
0.883	0.210
1.097	0.259
1.366	0.318
1.714	0.396
2.157	0.504
2.724	0.661
3.445	0.827
4.361	1.062
5.535	1.337
7.032	1.719
8.858	2.160
10.724	2.621
13.151	3.228
16.196	3.973
20.047	4.914
25.012	6.149

6.2. Selection of targets

The purpose of obtaining EM63 data for a set of targets at multiple depths is three-fold:

1. assess the noise characteristics of the instrument (Section 6.3)
2. assess the depth of detection of differing targets with the instrument (Section 6.4)
3. use the data in the development of the fast approximation for modeling of EMI response of munitions (Section 6.5).

A range of ordnance target types from 20mm to 150mm diameter (see Section 4.1, Figure 11) were selected. In addition a length of copper pipe 100mm diameter, 400mm long was used to provide a non-magnetic target.

6.3. Geological background and noise at EMIT test pit

Figure 32 shows three different passes of the EM63 over the pit with no target in place. We see a significant geological response towards the end of the profile. This response is difficult to calibrate with the EM63 since the provision in the instrument of a button for suppression of background signal makes quantitative study difficult. However after reviewing this data together with profiles acquired with the B-field sensors discussed subsequently, we believe the large geological background at the end of the profile (2.4m and beyond, which corresponds with the end of the pit) is due to magnetic minerals in the soil. The response is too high and too slow in its decay to be associated with conductive soil.

The noise level observed by the EM63 in a profile across the test pit can be assessed using the roughening filter of Section 6.4 applied to the profiles of Figure 32. The noise level for processed time-domain data is shown in Figure 33. As noted in Section 5.5 for the B-field sensors, we present noise in two plots, units of pT/s for the EM63 time windows, and units of $\text{pT/s} \cdot \sqrt{\text{sec}}$ to give a plot which is independent of the time window widths used.

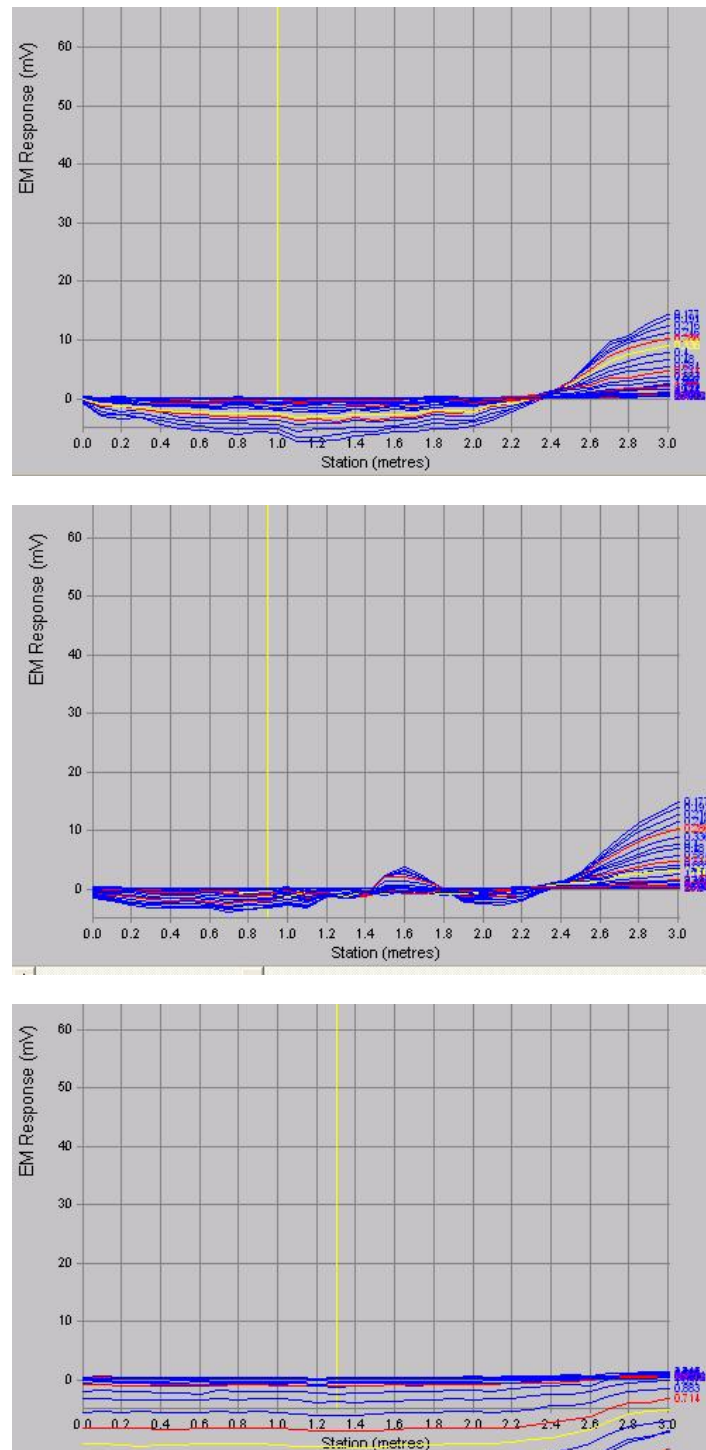


Figure 32: EM63 profiles over EMIT test pit, with no target

The different background levels reflect differing use of the background suppression button on the EM63. The higher response at the right hand end of the profile (2.4-3 m) is believed to be due to magnetic minerals in the soil.

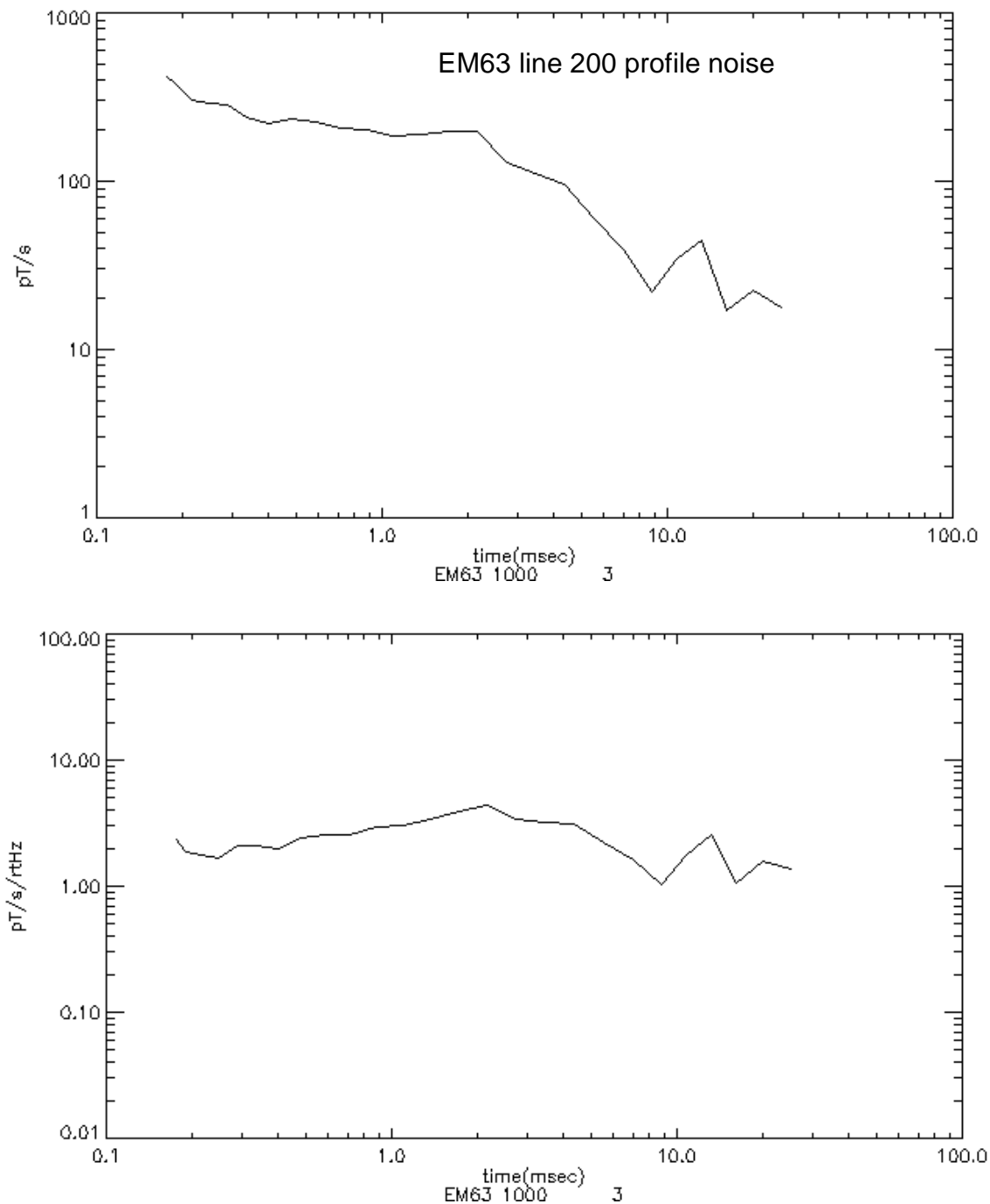


Figure 33: Noise of EM63 profile in a 4m profile over the EMIT test pit, speed 0.5 m/sec
 TOP: RMS noise in pT/s in each time window. Units: 1 pT/s = 0.001 mV .
 BOTTOM: RMS noise normalized for time window width, into units of pT/s/rHz

6.4. Summary of results

Table 3 shows the set of targets, depths and orientations tested with the EM63 over the EMIT test pit. Plotted profiles and decay curves are included in full in Appendix D.

6.5. Comparison of target responses with modeling using a conductive permeable prism approximation

The approximation algorithm is described in Section 10 and in full in a paper included as Appendix B. The paper discusses use of the model algorithm for the copper pipe target, and for the 75mm cannon shell

Figure 34 provides a further example of use of the algorithm in comparing observed and model responses of a 40mm cannon shell at depths 0 and 300mm below ground level. Figure 34(a) and (b) show a match of observed and modeled EM63 decay amplitude and rate where the target is 300 mm below ground level. The late-time channels (b) were inverted to obtain the model shown. Conductivity, apparent flux gathering and effective permeability parameters are the same for late-time data for the targets at the two different depths (as expected, if the model algorithm is to be generally useful). The major difference noted is that apparent flux gathering and effective permeability parameters are a factor of 3 to 4 larger at late times compared with early times (consistent with observations with the 75 mm shell in Appendix D) which we attribute to the non-linear or viscous behavior of magnetic properties in steel.

Table 3 – EM63 time domain EMI observations on munitions in EMIT pit

TIME-DOMAIN EMI OBSERVATIONS ON MUNITIONS AT EMIT TEST PIT

Target	Depth to base	EM63		Fluxgate FG		SQUID SQ	
		x//	vert	x//	vert	x//	vert
Cu pipe	0						
	300						
	530	y	y				
	880	y	y				
20mm shell	0	y	y				
	300	n	y				
	530						
	880						
40mm shell	0	y	y				
	300	y	y				
	530	m	y				
	880	n	m				
75mm shell	0						
	300	y	y				
	530	y	y				
	880	n	y				
BDU33 practice bomb	0						
	390	y					
	530						
	910	y					

Notes: (1) Cu pipe copper plumbing pipe 400mm long x 100 mm diameter
 20 mm shell: cannon shell, ferrous, 80mm long x 20mm diameter
 40 mm shell: cannon shell, ferrous, 130mm long x 40mm diameter
 75 mm shell: cannon shell, ferrous, 230mm long x 75mm diameter
 BDU33 practice bomb, ferrous, 600mm long, body 100mm diameter, tail assembly 150 mm diameter

Notes: (2) Depth to base is depth below pit cover or ground level.
 For EM33, add 425mm for depth below transmitter coil and receiver coil
 For BEAMOD™ Mk2 assembly, add 395 mm for depth below transmitter coil centre,
 and receiver sensor reference point

Notes: (3) y = target detectable above noise
 n = target NOT detectable above noise
 m = target marginally detectable in noise

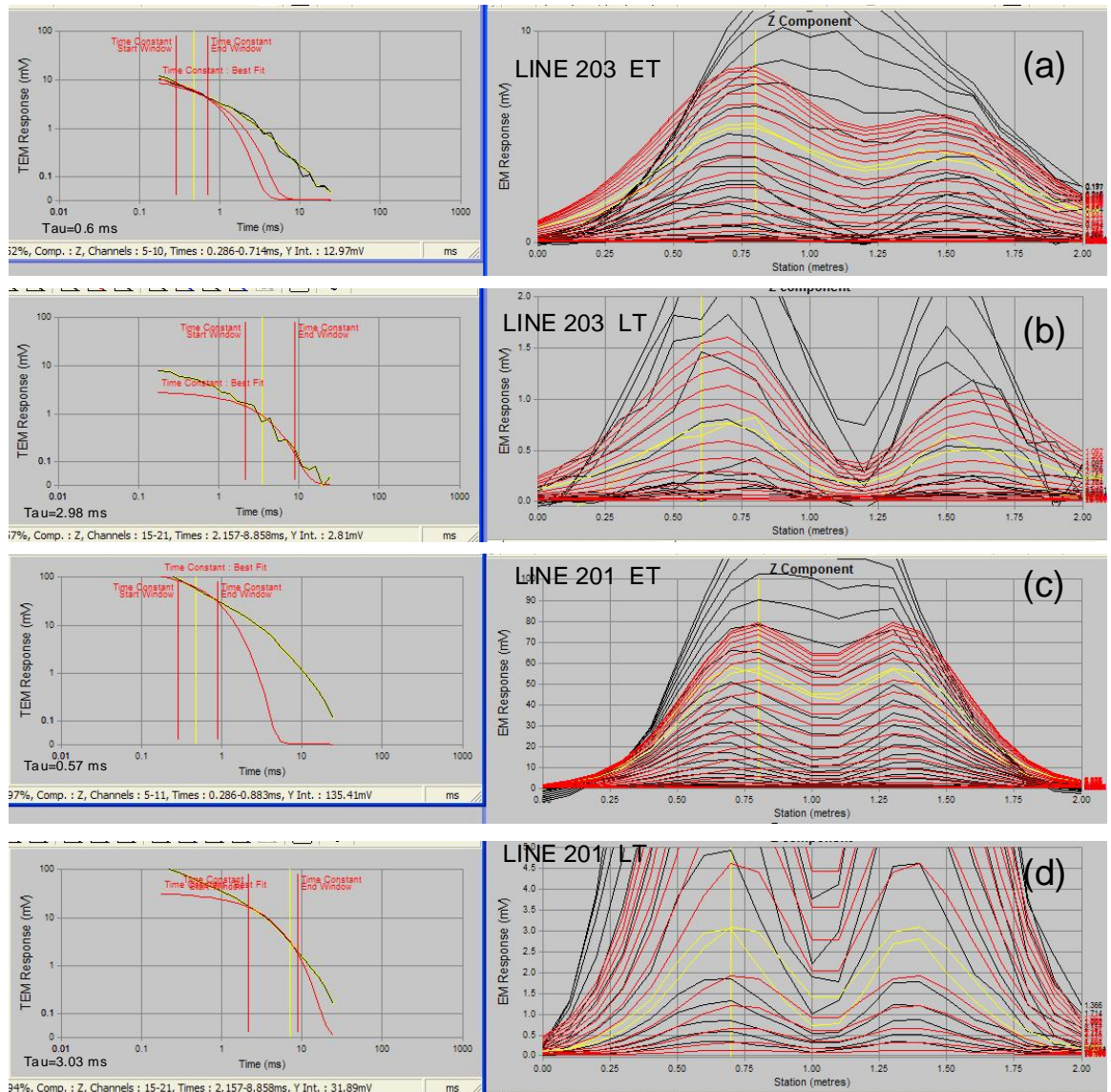


Figure 34 – EM63 profiles Line 203 over a 40mm cannon shell oriented horizontally, axis parallel with traverse. Base 300mm below pit cover.

Black: observed data. Red: model data.

(a) Fitting on early time channels 5-10 (0.3-0.7 ms).

Center of shell at $x = 1.05$, depth to top modeled = 0.73 m (actual was 0.70 m).

Equivalent conductivity = 130E3 S/m.

Apparent flux gathering coefficients $U_1 = 1200$, $U_2 = 38$.

Effective magnetic permeability $\mu_{e1} = 100$, $\mu_{e2} = 75$.

(b) Inversion on late time channels 17-22 (3.4-10 ms).

Center of shell at $x = 1.1^*$, depth to top modeled = 0.733* m (actual was 0.70 m).

Dip of shell axis = 5.2^* , diameter = 0.04 m.

Length = 0.13m, equivalent conductivity = 130E3* S/m.

Apparent flux gathering coefficients $U_1 = 5000$, $U_2 = 38$.

Effective magnetic permeability $\mu_{e1} = 400$, $\mu_{e2} = 300$.

(figure caption continued next page)

(c) Fitting on early time channels 5-10 (0.3-0.7 ms).
Center of shell at $x = 1.05$, depth to top modeled = 0.38 m (actual was 0.38 m).
Equivalent conductivity = $130\text{E}3$ S/m.
Apparent flux gathering coefficients $U_1 = 2000$, $U_2 = 38$.
Effective magnetic permeability $\mu_{e1} = 140$, $\mu_{e2} = 100$.
(d) Fitting on late time channels 17-22 (3.4-10 ms).
Center of shell at $x = 1.05$, depth to top modeled = 0.38 m (actual was 0.38 m).
Equivalent conductivity = $130\text{E}3$ S/m.
Apparent flux gathering coefficients $U_1 = 5000$, $U_2 = 38$.
Effective magnetic permeability $\mu_{e1} = 400$, $\mu_{e2} = 300$.

7. B-FIELD SENSOR RESULTS OVER TEST PIT

7.1. Selection of targets

The specifications of the BEAMOD™ Mk 2 system with a fluxgate sensor as used for acquiring data over the EMIT test pit are given above in Section 3.6.

The purpose of obtaining B-field sensor data for a set of targets at multiple depths is three-fold:

1. assess the noise characteristics of the sensors and BEAMOD™ instrument (Sections 5.5, 5.6 and 5.7)
2. use the data in the development of the fast approximation for modeling of EMI response of munitions (Sections 7.4 and 10)
3. assess the depth of detection to differing targets with the instrument (Section 7.5).

Targets were selected to offer a range of ordnance types from 20mm to 150mm diameter (see Section 4.1, Figure 11). In addition a length of copper pipe 100mm diameter by 400mm long was used to provide a non-magnetic target.

7.2. Geological background and noise at EMIT test pit

Figure 35 shows BEAMOD™ Mk 2 profiles of the pit with no target in place, using the fluxgate sensor. Figure 36 shows similar profiles using the SQUID sensor. The raw data for the fluxgate shows relatively small, but still significant, noise associated with level shifts, while the raw data for the SQUID is overprinted by huge level shifts. However processing these profiles with leveling and stripping algorithms as discussed in Section 5.4 yields profiles of value. Note that we have not normalized data for transmitter current, hence the fluxgate data is a factor of three larger (in pT) than the SQUID data.

As noted with the EM63 instrument at this site, we see a significant geological response towards the end of the profile (3m and beyond) which corresponds with the end of the pit). We believe this large response is due to magnetic minerals in the soil as the response is too high and too slow in its decay to be associated with conductive soil.

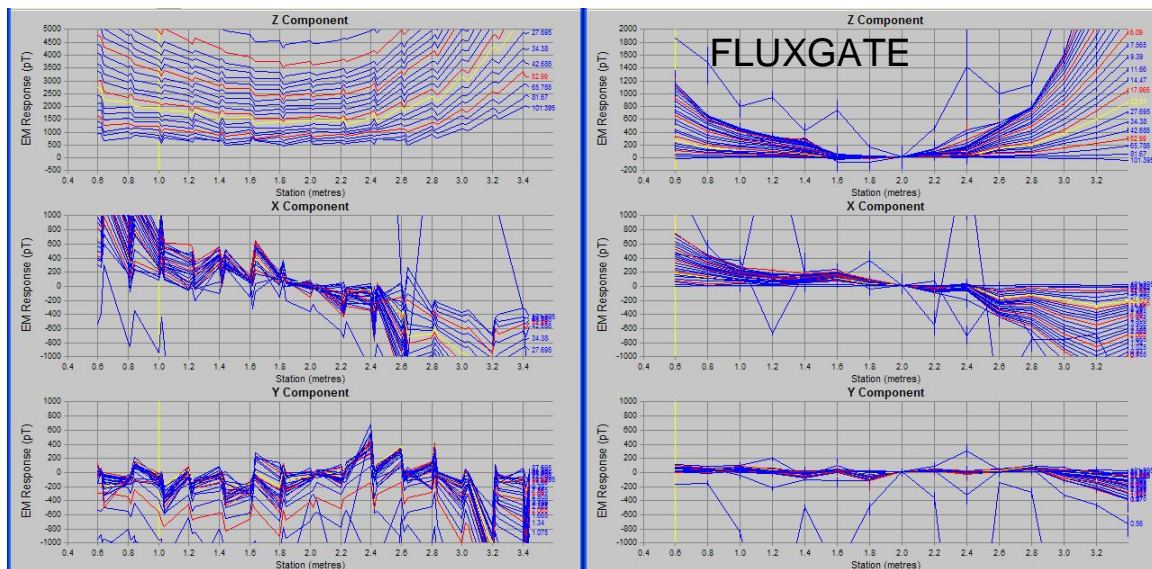


Figure 35: BEAMOD™ Mk2 profiles of length 3 m, using fluxgate sensors measuring three components in a profile over the EMIT test pit, with no target. Each plot shows profiles for time windows 7 to 33 (times 0.36 to 101 msec). Windows 1 to 6 are excluded due to bandwidth limitations of the fluxgate sensor.

Left: Line FG411. Fluxgate sensor, no target, raw data. There are two readings per station plotted separately. Level variations between successive readings are visible on all components. Transmitter current 12 A. Note that scale on the Z-component is -500 to +5000 pT, while scale on X and Y components is +-1000 pT, hence noise appears larger on the stretched scale of the X and Y components.

Right: Line FG411. Fluxgate sensor, no target. Data has been leveled and stripped. Response is geological background from magnetic soil (low response at center is due to absence of soil cover over the pit). Note: Station 2.0 marks the pit center, and is the same location as the station labeled 1.0 in EM63 profiles. Data units are pT.

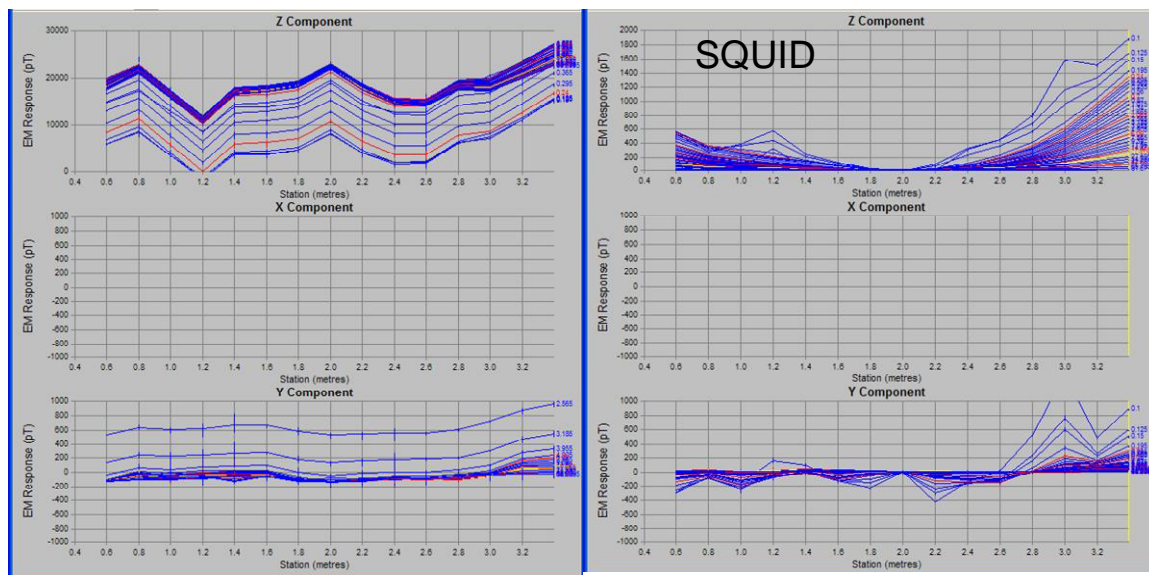


Figure 36: BEAMOD™ Mk2 profiles of length 3 m, using SQUID sensors measuring two components in a profile over the EMIT test pit, with no target. Each plot shows profiles for time windows 1 to 33 (times 0.1 to 101 msec). NB the early-time windows 1 to 6 are useable in SQUID data, whereas they are removed from fluxgate data due to the lower bandwidth of the fluxgate sensor.

Left: Line SQ412. SQUID sensor, no target, raw data. There are two readings per station plotted separately. The Z-component is grossly overprinted with unpredictable leveling problems. The X-component of the SQUID sensor was malfunctioning for these tests. Transmitter current 3.5 A.

Right: Line SQ412. SQUID sensor, no target. Data has been leveled and stripped. Response is geological background from magnetic soil (low response at center is due to absence of soil cover over the pit).

Note: Station 2.0 marks the pit center, and is the same location as the station labeled 1.0 in EM63 profiles. Data units are pT.

The noise level observed by the fluxgate sensor in a profile across the test pit can be assessed using the roughening filter of Section 5.4 applied to the profiles of Figure 35 and Figure 36. The noise level for stacked time-domain data for the fluxgate sensor is shown in

Figure 37. As noted in Section 5.5 for the B-field sensors, we present noise in two plots, units of pT for the BEAMOD™ time windows, and units of $\text{pT} \cdot \sqrt{\text{sec}}$ to give a plot which is independent of the time window widths used.

Figure 38 shows the equivalent noise levels observed in a profile using the SQUID sensor and BEAMOD™ Mk 2 system. The noise with the SQUID sensor for times greater than 1 msec is about a factor of three lower than that for the fluxgate sensor, corresponding to the lower transmitter current employed. The noise at times above 1 msec in these two figures is therefore believed to be geological in origin rather than instrumental.

For early time windows below 0.5msec,

Figure 37 and Figure 38 show the SQUID sensor very much lower in noise, by up to a factor of 100 at 0.1 msec. This difference is attributable to the limited bandwidth of the fluxgate sensor (DC-3 kHz, compared with DC to >10kHz for the SQUID).

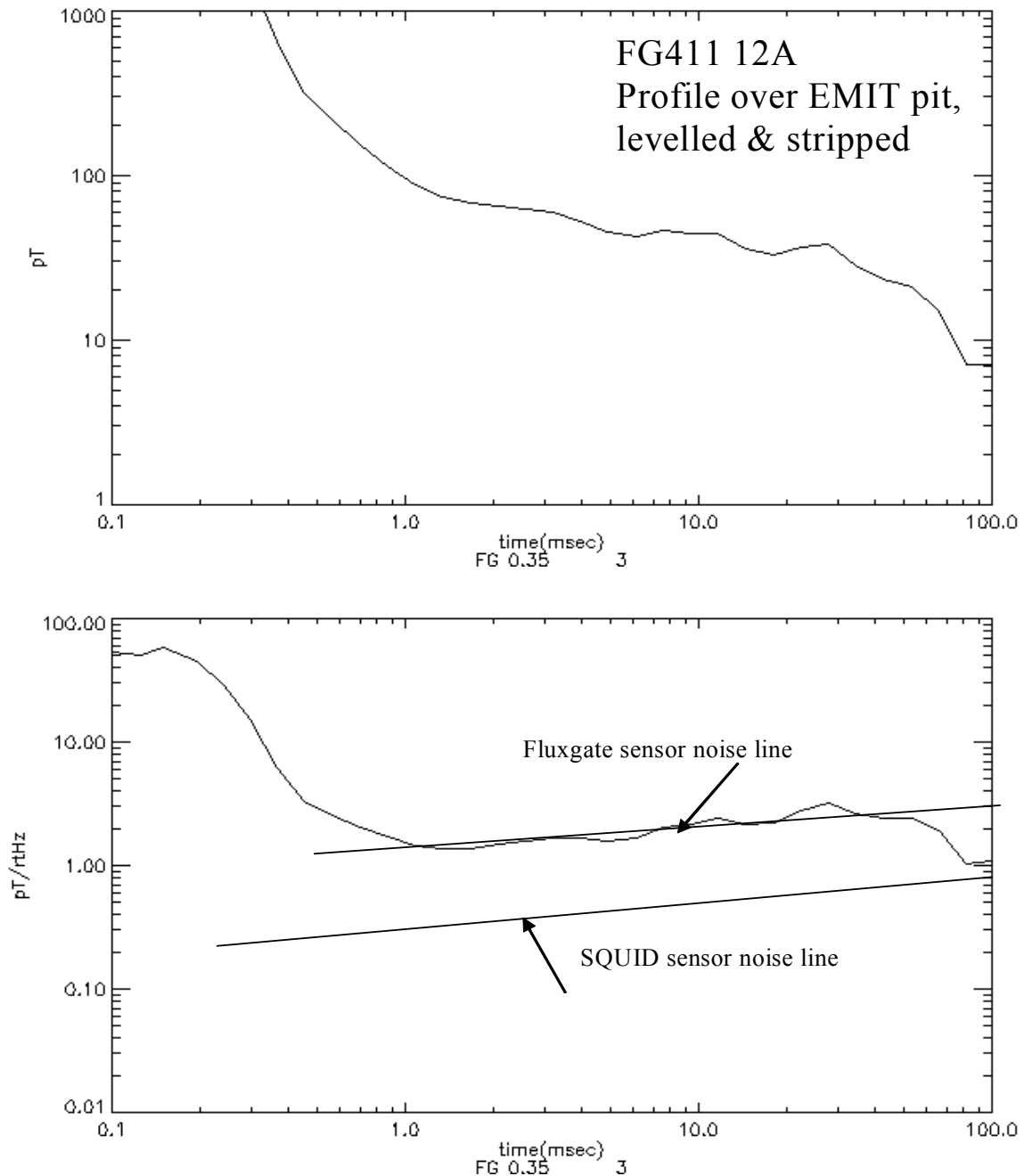


Figure 37: Noise of fluxgate sensor with BEAMOD™ Mk 2 system in a 4m profile over EMIT test pit, using BEAMOD™ time windows, transmitter current 12A.

TOP: RMS noise in pT in each time window, for 64 stacks.

BOTTOM: RMS noise normalized for time window width, into units of pT.√sec

Noise is computed from data which has been levelled, stripped and roughened as described in text.

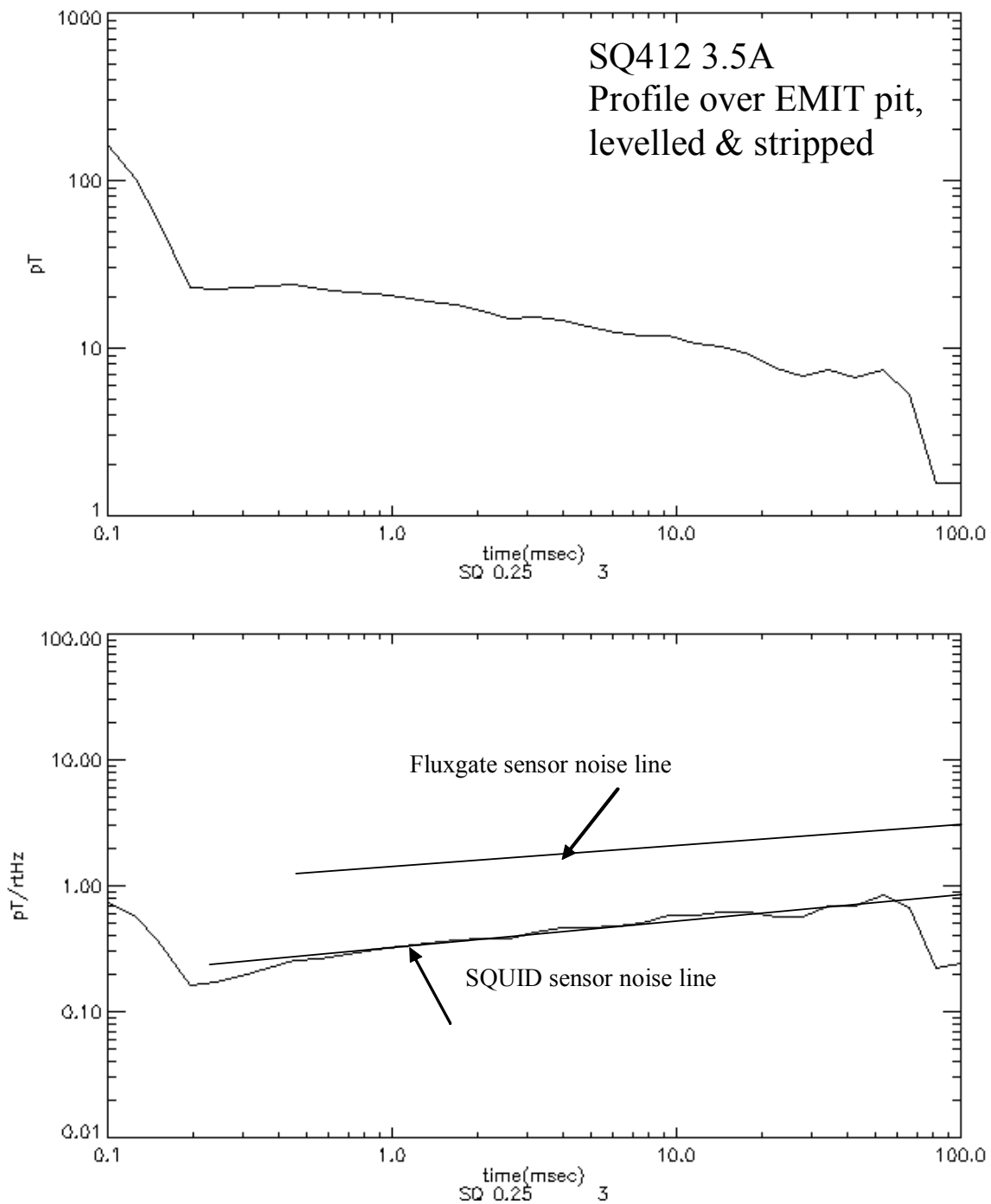


Figure 38: Noise of SQUID sensor with BEAMOD™ Mk 2 system in a 4 m profile over EMIT test pit, using BEAMOD™ time windows, transmitter current 3.5A.
 TOP: RMS noise in pT in each time window, for 64 stacks.
 BOTTOM: RMS noise normalized for time window width, into units of $\text{pT} \cdot \sqrt{\text{sec}}$
 Noise is computed from data which has been levelled, stripped, and roughened as described in text.

7.3. Summary of results using B-field sensors

Table 4 shows the set of targets, depths and orientations tested with the two B-field sensors over the EMIT test pit. The full set of plotted profiles and decay curves are included in full in Appendices D and E.

Table 4 - Time-Domain EMI Observations on Munitions at EMIT Test Pit

TIME-DOMAIN EMI OBSERVATIONS ON MUNITIONS AT EMIT TEST PIT							
Target	Depth to base (m)	EM63		Fluxgate FG		SQUID SQ	
		x//	vert	x//	vert	x//	vert
Cu pipe	0						
	300						
	530	y	y	y	y	y	y
	880	y	y	y	y	y	y
20mm shell	0	y	y		y		y
	300	n	y		y	m	y
	530						
	880						
40mm shell	0	y	y			y	
	300	y	y	y	y	y	y
	530	m	y	m	y	y	y
	880	n	m	n	y	n	y
75mm shell	0						
	300	y	y				
	530	y	y	y	y	y	y
	880	n	y	y	y	y	y
BDU33 practice bomb	0						
	390	y					
	530			y			
	910	y		y	y	y	y

Notes: (1) Cu pipe copper plumbing pipe 400mm long x 100 mm diameter
 20 mm shell: cannon shell, ferrous, 80mm long x 20mm diameter
 40 mm shell: cannon shell, ferrous, 130mm long x 40mm diameter
 75 mm shell: cannon shell, ferrous, 230mm long x 75mm diameter
 BDU33 practice bomb, ferrous, 600mm long, body 100mm diameter, tail assembly 150 mm diameter

Notes: (2) Depth to base is depth below pit cover or ground level.
 For EM33, add 425mm for depth below transmitter coil and receiver coil
 For BEAMOD™ Mk2 assembly, add 395 mm for depth below transmitter coil centre,
 and receiver sensor reference point

Notes: (3) y = target detectable above noise
 n = target NOT detectable above noise
 m = target marginally detectable in noise

Note that profiles in Appendices D and E are generally limited to two or three points per profile in order to speed up the process of data acquisition, since the BEAMOD™ Mk2 system is relatively awkward to move in its present prototype form. Points measured are station 1.0 (1m removed from the target, hence typically background), 2.0 (directly over the target) and 1.5 (for horizontally oriented shells which have their maximum response at this location). The decay curve response of the target is available from either the 1.5 or 2.0 location. Examples of profiles where a full profile has been acquired as well as a two or three-point profile, are shown in Appendix E pages 4-5, and Appendix F pages 11-12.

7.4. Comparison of target responses with modeling using a conductive permeable prism approximation

The approximation algorithm as applied to EM63 data is described in Section 10, and in full in a paper included as Appendix B. We now demonstrate that this algorithm can be applied in the same way to B-field data.

Figure 39 shows observed and model responses of a 400mm x 100mm copper pipe at depth 530mm below the pit cover, as observed using the fluxgate sensor. The profile is a three-point half-length profile designed to capture the critical features of the expected shape of the profile.

Figure 40 shows full profiles for observed and model data for the same model, where the target is at depth 880 mm below the pit cover. The late-time channels 11-21 (times 1-7.5 msc) were inverted by iterative forward modeling to obtain the model shown (automated inversion suffers from bias due to the strong geological background response). Fitting amplitudes and decay constant resolves position (Z, X and Y in this case, due to the use of three-component data) and conductivity. WE are restricted to iterative forward modeling rather than mathematical inversion for this exercise due to existing limitations of our software in this prototyping phase of the project. Iterative forward modelling is inevitably rather subjective, with the stopping criterion being simply the best visual fit of channel amplitudes and decay near the center of the profile, but it is of value to note that the 3-sensor 3-component observed data resolves position of the target without recourse to prior knowledge of the target position. Note also that in Figs. 39-41 the data resolves a Y-coordinate, corresponding to discrepancy in actual positioning of the target within the pit, even though the “nominal” or “correct” position was directly below the profile, i.e. with an intended Y=0. Since the model derived for the shallower target also fits the observed data for the deeper target, we have a demonstration of the validity of the processing stream for the observed data, and the validity of the approximation algorithm used for forward modeling of the target.

Figure 41 and Figure 42 provide further examples of use of the algorithm in comparing B-field observed and model responses of a 40mm cannon shell with base respectively at depths 0 and 300mm below ground level. Late-time channels were manually iteratively inverted to obtain the model shown. Conductivity, apparent flux gathering and effective permeability parameters are the same for late-time data for the targets at the two different depths (as expected, if the model algorithm is to be generally useful).

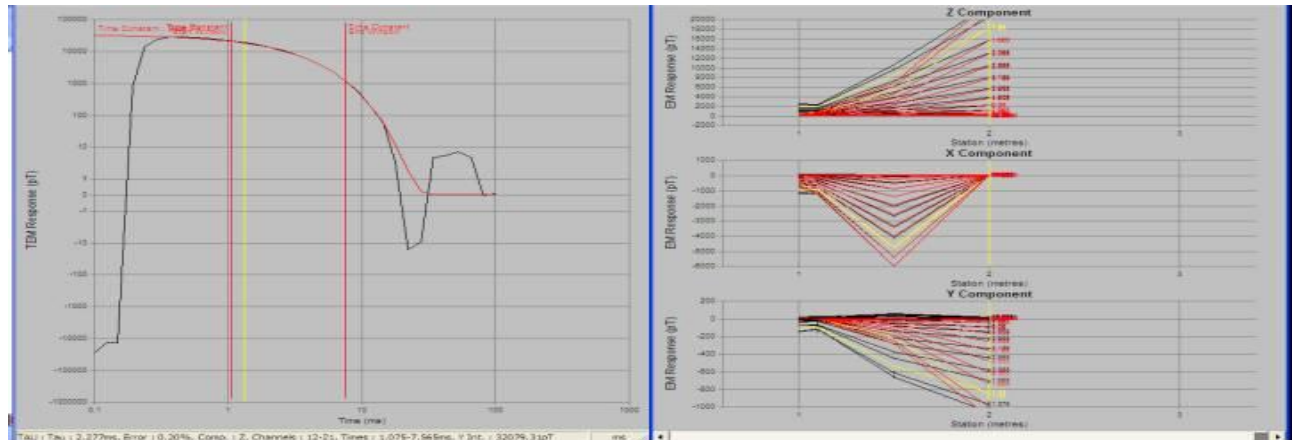


Figure 39: Three-point half profile observed (after stripping and leveling) and model responses of a 400mm x 100mm copper pipe at true depth 530mm below the pit cover, as observed using the fluxgate sensor.

File FG431: target is horizontal, center at station 2.0. Profile shows The late-time channels Ch 11-21 (1-7.5) msec. The yellow line is ch 13 (1.3 msec).

Profile was manually inverted to obtain the model shown. Note the very close fit at left to an exponential decay curve. The oscillation of the decay curve for times >20 msec shows limitations of the stripping process at late times/low amplitudes.

Inversion parameters:

Depth center=870 mm below transmitter; (ie. Interpreted depth to base of target =525mm below pit cover).

Target Center is Z=-0.870, X=2.0, Y=0.04 m, conductivity=3.0E6 S/m.

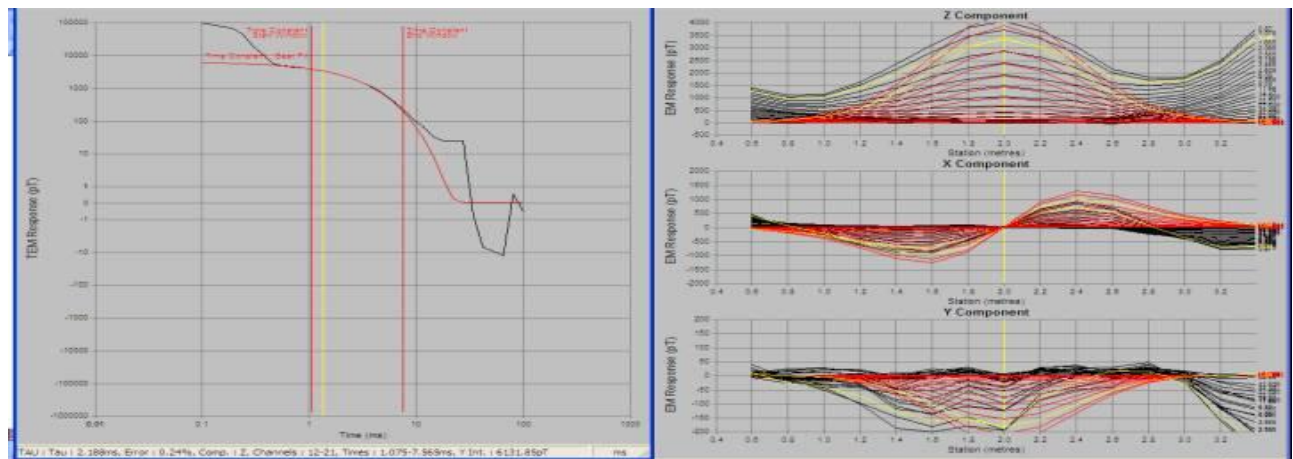


Figure 40: Observed (after stripping and leveling) and model profile responses of a 400mm x 100mm copper pipe at true depth 880mm below the pit cover, as observed using the fluxgate sensor.

File FG805: target is horizontal, center at station 2.0. Profile shows The late-time channels Ch 11-21 (1-7.5) msec. The yellow line is ch 13 (1.3 msec).

Profile was manually inverted to obtain the model shown. Note the very close fit at left to an exponential decay curve. The oscillation of the decay curve for times >20 msec shows limitations of the stripping process at late times/low amplitudes.

Inversion parameters: Depth center=1200 mm below transmitter; (ie. Interpreted depth to base of target =855mm below pit cover).

Target Center is Z=-1.200, X=2.0, Y=0.04 m, conductivity=3.0E6 S/m.

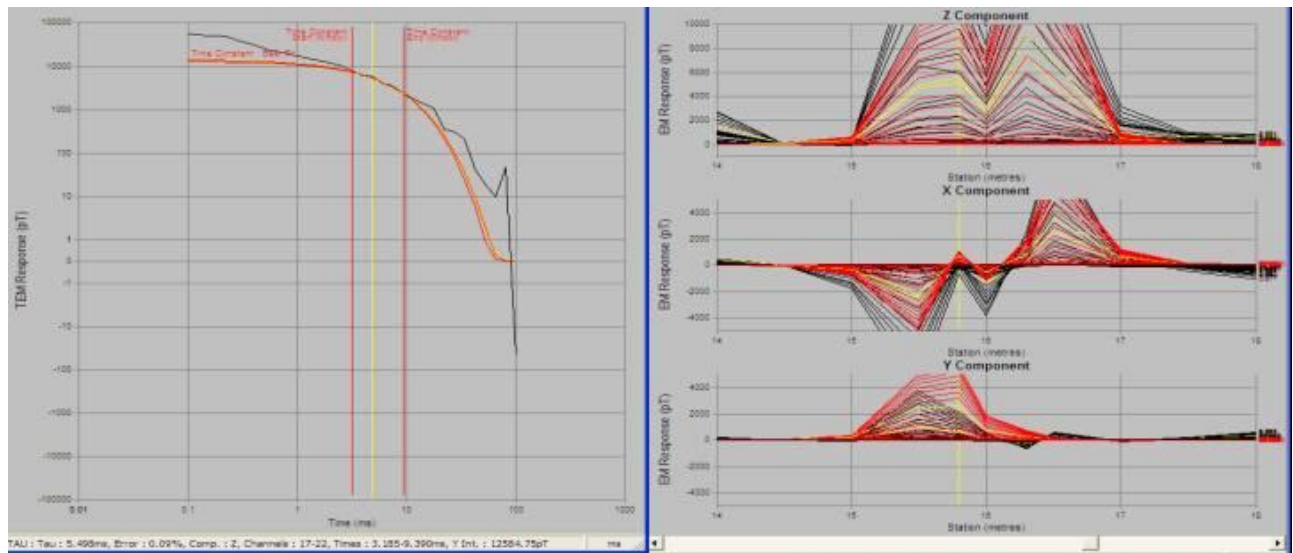


Figure 41: Observed and model profile late-time responses of a 40mm cannon shell with base at ground level (pit cover), as observed using the fluxgate sensor. File FG807: target is horizontal, center at station 16.0. Profile is late time Ch 11-21 (1-7.5 msec). Profile was manually inverted to obtain the model shown. Yellow line is Ch 19 (4.9 msec). Note the decay curve is slower than an exponential, but locally fits an exponential decay curve with $\tau=5.5$ msec.

Inversion parameters:

Depth center=415 mm below transmitter; (ie. Interpreted depth to base of target =40mm below ground). Target Center is $Z=-0.415$, $X=16.02$, $Y=-0.1$ m, conductivity= $1.3E5$ S/m.

App flux gathering coeffs $U_1 = 6000$, $U_2 = 38$. Eff magnetic permeability $\mu_{e1} = 600$, $\mu_{e2} = 300$.

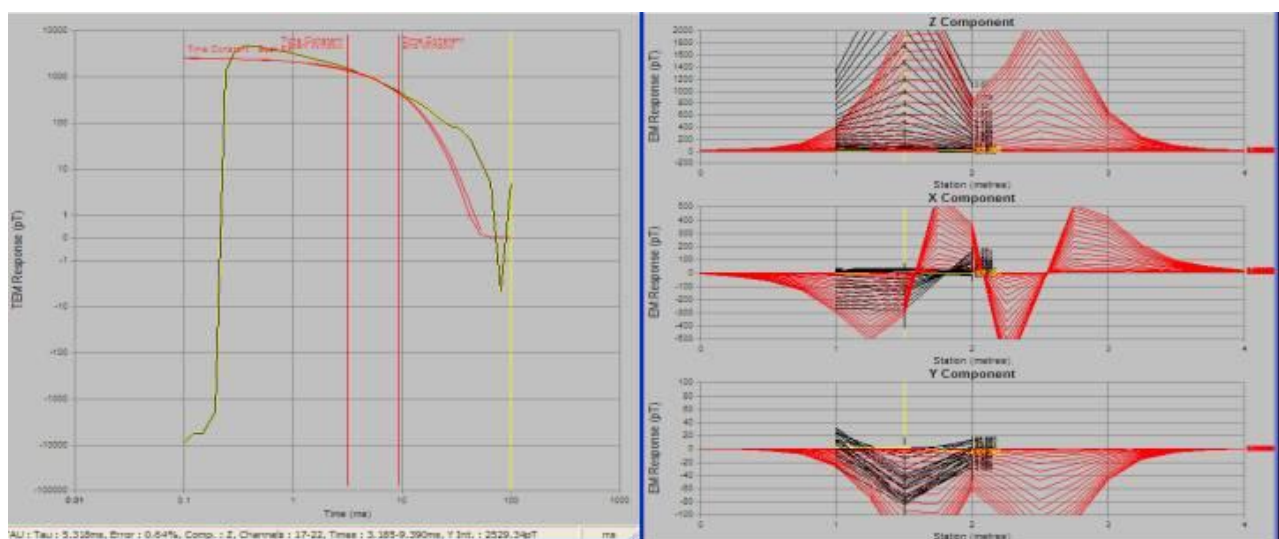


Figure 42: Observed and model profile late-time responses of a 40mm cannon shell with base at depth 300 mm below pit cover, as observed using the fluxgate sensor.

File FG415: target is horizontal, center at station 2.0. Profile is late-time Ch 11-21 (1-7.5 msec). Profile was manually inverted to obtain the model shown. Yellow line is Ch 19 (4.9 msec). Note the decay curve is slower than an exponential, but locally fits an exponential decay curve with $\tau=5.5$ msec.

Inversion parameters: Depth center=700 mm below transmitter; (ie. Interpreted depth to base of target =325 mm below ground). Target Center is $Z=-0.7$, $X=2.065$, $Y=0.05$ m.

Conductivity, app flux gathering coeffs, and eff magnetic permeability as for Figure 41.

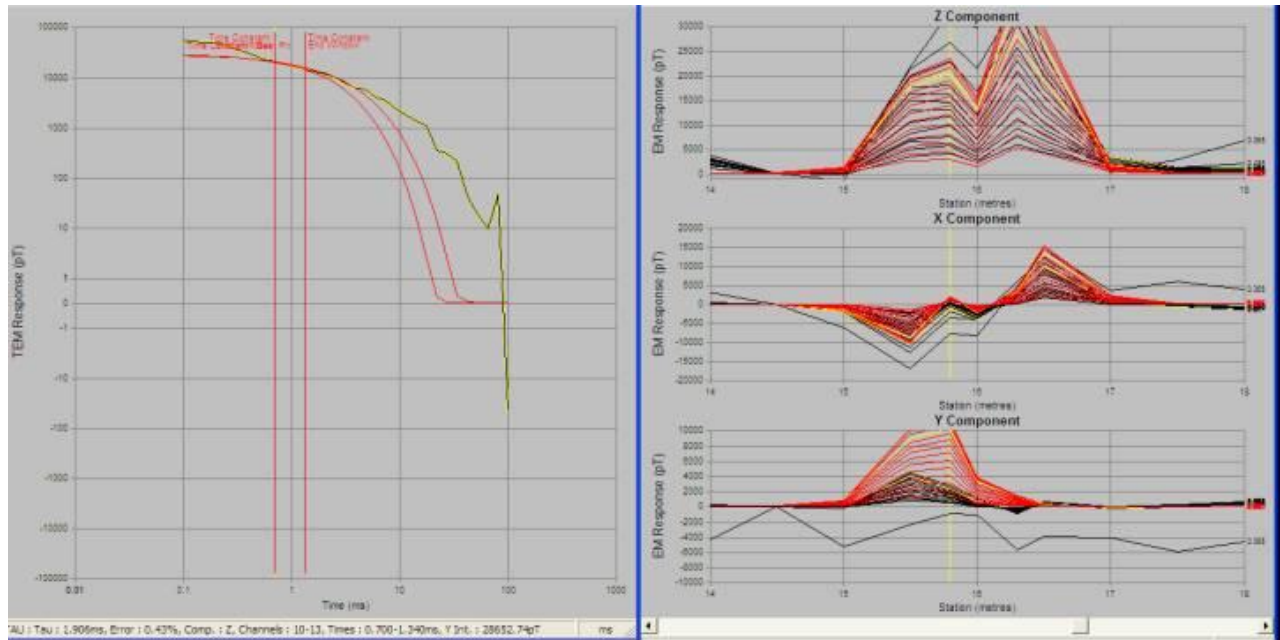


Figure 43: Observed and model early-time profile responses of a 40mm cannon shell with base at ground level (pit cover), as observed using the fluxgate sensor.

File FG807: target is horizontal, center at station 16.0. Profile is late time Ch 7-20 (0.7-6 msec). Profile was manually inverted to obtain the model shown. Yellow line is Ch 10 (0.7 msec). Note the decay curve is slower than an exponential, but locally fits an exponential decay curve with $\tau=2$ msec.

Inversion parameters:

As for Figure 41 except reduced effective magnetic permeability $\mu_{e1} = 300$, $\mu_{e2} = 150$.

Figure 43 shows a match of observed and field data for the same 40mm shell at the earth surface, but computed using early time channels. All target parameters remain the same except for the effective permeability which reduces by a factor of two at early times compared with late times. It is important to note the difference in behavior of this 40mm shell compared with the 75 mm shell discussed in Figure 3 of Appendix B; in the case of the 75 mm shell, a huge reduction of both permeability and flux gathering coefficients (a factor of order 150) was noted in the change from late to early time modeling. We attribute the change in these coefficients to the frequency-dependent non-linear or viscous behavior of magnetic properties in steel, and the very different behavior of the two shell types suggests that differing magnetic properties exist and may in future be useful in target discrimination.

In a perfectly linear world we would expect the target parameters for the fitted model of the 40mm shell to be the same when fitting EM63 data in Figure 34 as when fitting fluxgate-sensor data in Figure 42, over similar time window ranges. In fact the fit yields some differences in the target magnetic properties, being for the EM63:

Apparent flux gathering coefficients $U_1 = 5000$, $U_2 = 38$,

Effective magnetic permeability $\mu_{e1} = 400$, $\mu_{e2} = 300$,

and for the fluxgate sensor:

Apparent flux gathering coefficients $U_1 = 6000$, $U_2 = 38$,

Effective magnetic permeability $\mu_{e1} = 600$, $\mu_{e2} = 300$.

The fluxgate sensor shows stronger magnetic properties in the range 20-50% for both apparent flux gathering and effective permeability. As a hypothesis, we can attribute this difference to the different transmitter waveforms (the fluxgate sensor has transmitter pulses three times longer than the EM63), but the difference does not affect our conclusions regarding depth of detection of the target since we derive the model parameters for each transmitter system using actual observations with that system.

7.5. Assessment of maximum depth of detection, EM63 vs. fluxgate sensor

Table 4 above provides a qualitative indicator of depth of detection capabilities of the EM63 and the two B-field sensors. We summarize results thus:

- a. Copper pipe: all sensors see both orientations to maximum depth of 880 mm below pit cover.
- b. 20mm cannon shell: At 300 mm depth below pit cover, x-parallel orientation, this item is not detectable by the EM63, but is marginally detectable by the fluxgate sensor, and detectable by the SQUID sensor. (The latter is better on this small target due to its better response at early time windows).
- c. 40 mm cannon shell: At 530 mm depth below pit cover, x-parallel orientation, this item is not detectable by the EM63, but is marginally detectable by the fluxgate sensor, and detectable by the SQUID sensor.
- d. 40 mm cannon shell: At 880 mm depth below pit cover, vertical orientation, this item is marginally detectable by the EM63, but is detectable by both B-field sensors.
- e. 75 mm cannon shell: At 880 mm depth below pit cover, x-parallel orientation, this item is not detectable by the EM63, but is detectable by both B-field sensors.
- f. BDU33 practice bomb: detectable by all sensors; needs a deeper pit to see limits.

Given the validation of the modeling process outlined in the previous Section, we use the noise characteristics of the profile of the EMIT pit and for each type of target superimpose a series of model curves for a range of burial depths. This allows a quantitative assessment of the useful time window and limits of detection depth, for all targets and all sensor types. Detection ability is a subjective criterion; we adopt for the purpose of this discussion the criterion that the target signature should be a factor two or more above noise in order to be detectable.

We calculate target model response curves for each sensor by first fitting a model to an observed profile acquired with that sensor, over the target where depth to target is sufficiently small to give EMI response over the full range of time windows. Inversion or iterative fitting for the target of known shape, depth and decay rate allows us to derive the conductivity and magnetic parameters for the target. These parameters are then used to compute model responses at a range of target depths from 200 to 2000 mm.

Figure 44 shows the set of model curves computed for the 400 x 100 mm copper pipe, horizontal, at depths 200 to 1700 mm. Calculations are made for each of the EM63, BEAMOD™ Mk 2 with fluxgate sensor and current 12 A, and BEAMOD™ Mk 2 with SQUID sensor and current 3.5 A. The limit of detection for the EM63 for this relatively large, highly conductive but non-magnetic object is 1400 mm, marginally deeper for the fluxgate sensor, and about 1700 mm for the SQUID sensor. Note however that at the deeper depths, the time range of detection is strongly limited and discrimination of the target (as distinct from simple detection) will be increasingly difficult.

Figure 45 shows the set of model curves computed for the 40 mm steel munitions shell, horizontal, at depths 200 to 1400 mm. Calculations are made for the EM63 and BEAMOD™ Mk 2 with fluxgate sensor and current 12 A. The predicted limit of detection for the EM63 for this relatively highly magnetic object is 530 mm, compared with range 780 mm for the fluxgate sensor. As previously observed, at the deeper depths, the time range of detection is strongly limited and discrimination of the target (as distinct from simple detection) will be increasingly difficult.

Figure 46 shows the set of model curves computed for the 75 mm steel munitions shell, horizontal, at depths 200 to 1400 mm. Calculations are made for the EM63 and BEAMOD™ Mk 2 with fluxgate sensor and current 12 A. The predicted limit of detection for the EM63 for this relatively highly magnetic object is 780 mm, compared with 1110 mm for the fluxgate sensor. With this larger class of target, decay rates are slower, and the time range of detection is less restricted for deep targets than was the case for the 40mm shell.

Figure 47 shows the set of model curves computed for the BDU33 practice bomb, horizontal, at depths 200 to 1400 mm. Calculations are made for the EM63 and BEAMOD™ Mk 2 with fluxgate sensor and current 12 A. The predicted limit of detection for both the EM63 and fluxgate sensors in the time window range 5-10msec is the same, at 1110mm. At later times the advantage of the fluxgate sensor becomes strongly apparent, e.g. at 20 msec the predicted limit of detection for the EM63 is 400 mm vs. 780 mm for the fluxgate sensor.

The bandwidth of detection is increased when using the fluxgate sensor compared with the EM63 system, for steel targets such as the 75 mm cannon shell and the BDU33 practice bomb. Using a target depth of 530 mm, Figure 47 shows for example that a BDU33 practice bomb target has a time-window of detection extending to 45 msec with the fluxgate sensor, compared with 20 msec for the EM63. Comparable increases are 25 msec vs 20 msec for the 75 mm shell, and 15 msec vs. 10 msec for the 40 mm shell. The copper pipe target shows a decrease in bandwidth with the fluxgate sensor, although depth of detection is still superior.

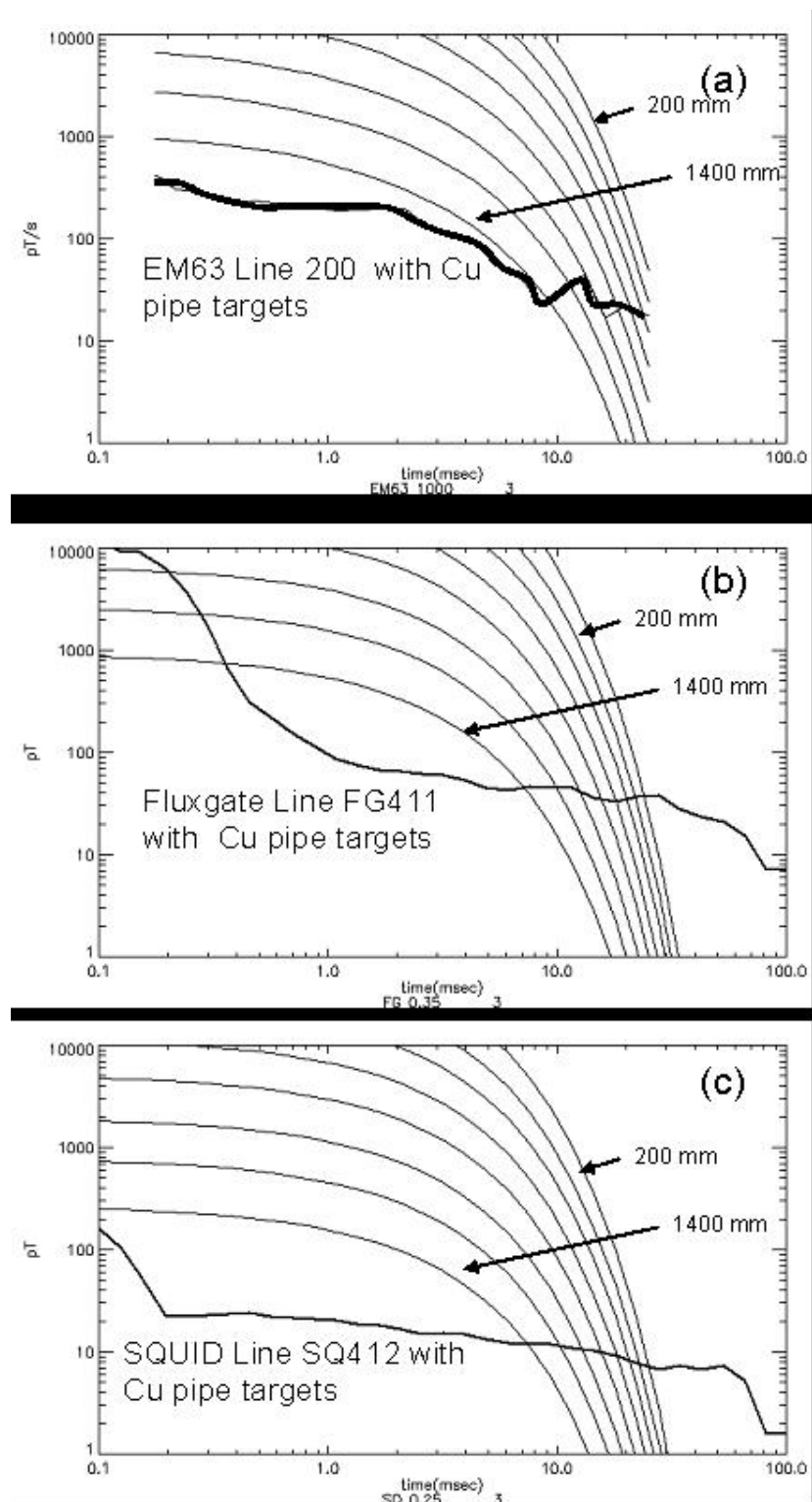


Figure 44 Model response of the copper pipe target oriented horizontally, to three EMI systems. Model response of the copper pipe target oriented horizontally to three EMI systems. Thick lines are observed noise levels on the EMIT test pit.

The suite of models (thin black lines) are computed for target depth to base, below the pit cover. Add 425mm or 395 mm for total depth below EM63 or BEAMOD transmitter coil, respectively. Range of depths below pit cover is: 200, 300, 400, 530, 680, 880, 1110, 1400mm

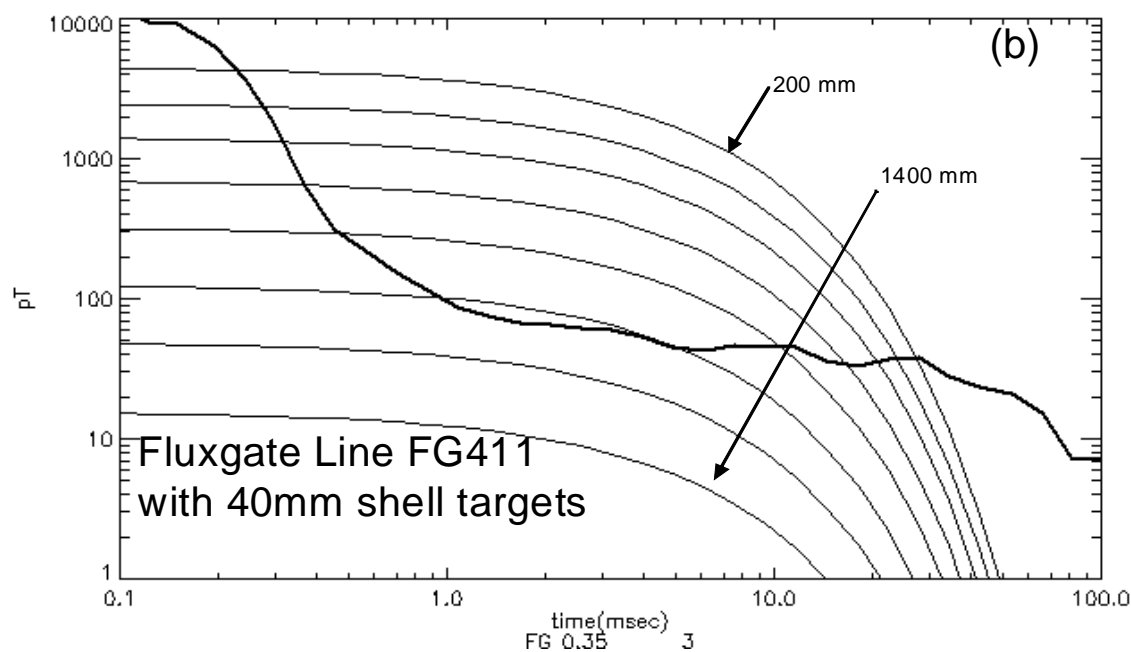
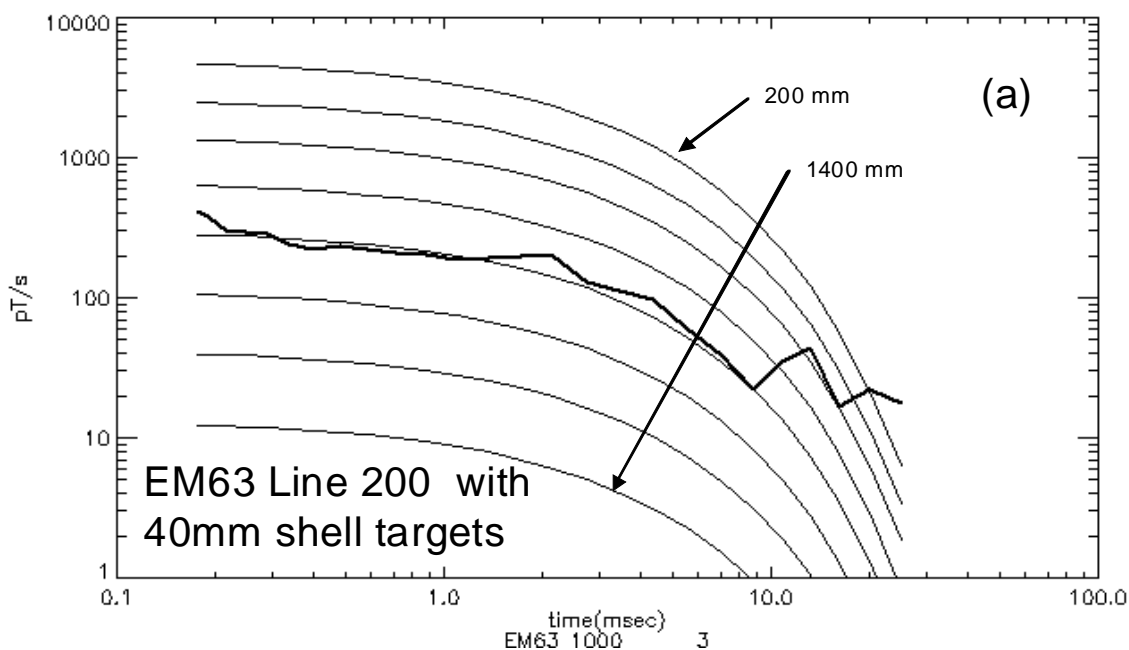


Figure 45 Model response of the 40mm shell target oriented horizontally, to two EMI systems

Model response of the 40mm shell target oriented horizontally, to two EMI systems

Thick lines are observed noise levels on the EMIT test pit.

The suite of models (thin black lines) are late-time responses computed for target depth to base, below the pit cover. Add 425mm or 395 mm for total depth below EM63 or BEAMOD™ transmitter coil, respectively.

Range of depths below pit cover is: 200, 300, 400, 530, 680, 880, 1110, 1400mm.

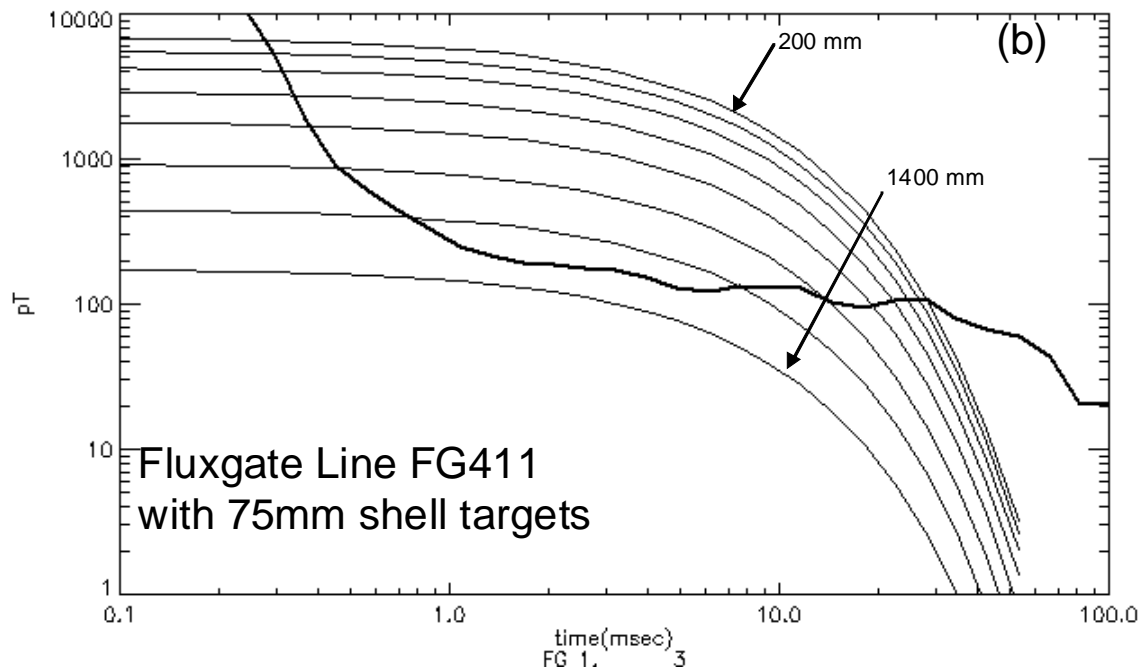
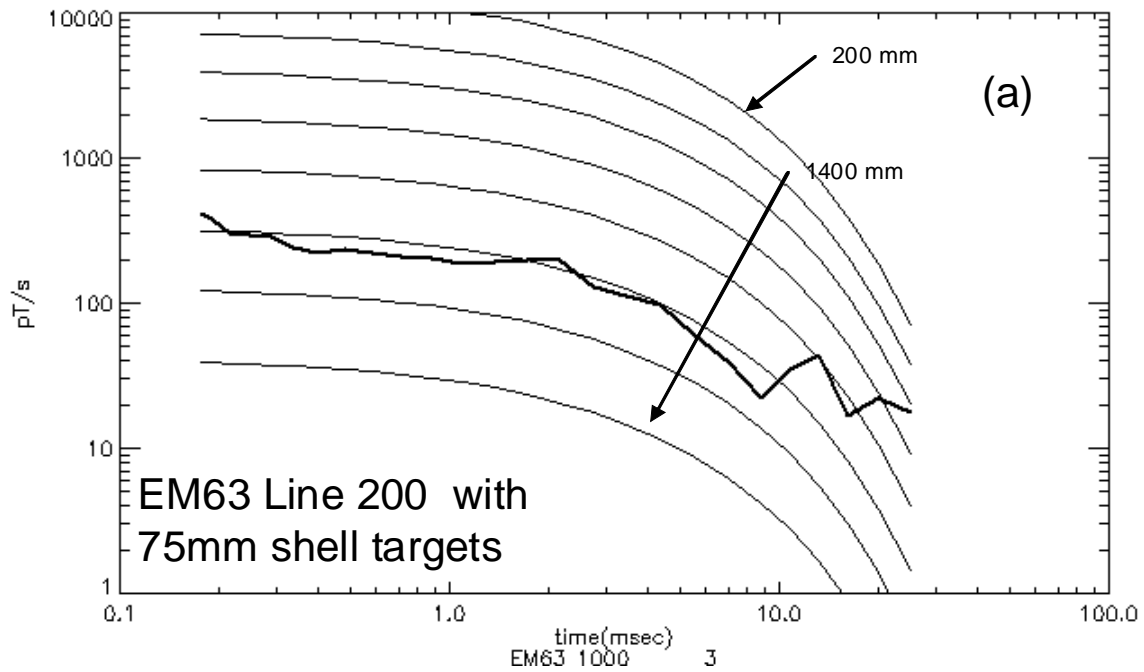


Figure 46 – Modeled response of the 75 mm shell target oriented horizontally, to two EMI systems
Thick lines are observed noise levels on the EMIT test pit.

The suite of models (thin black lines) are late-time responses computed for target depth to base, below the pit cover. Add 425mm or 395 mm for total depth below EM63 or BEAMOD™ transmitter coil, respectively.

Range of depths below pit cover is: 200, 300, 400, 530, 680, 880, 1110, 1400mm.

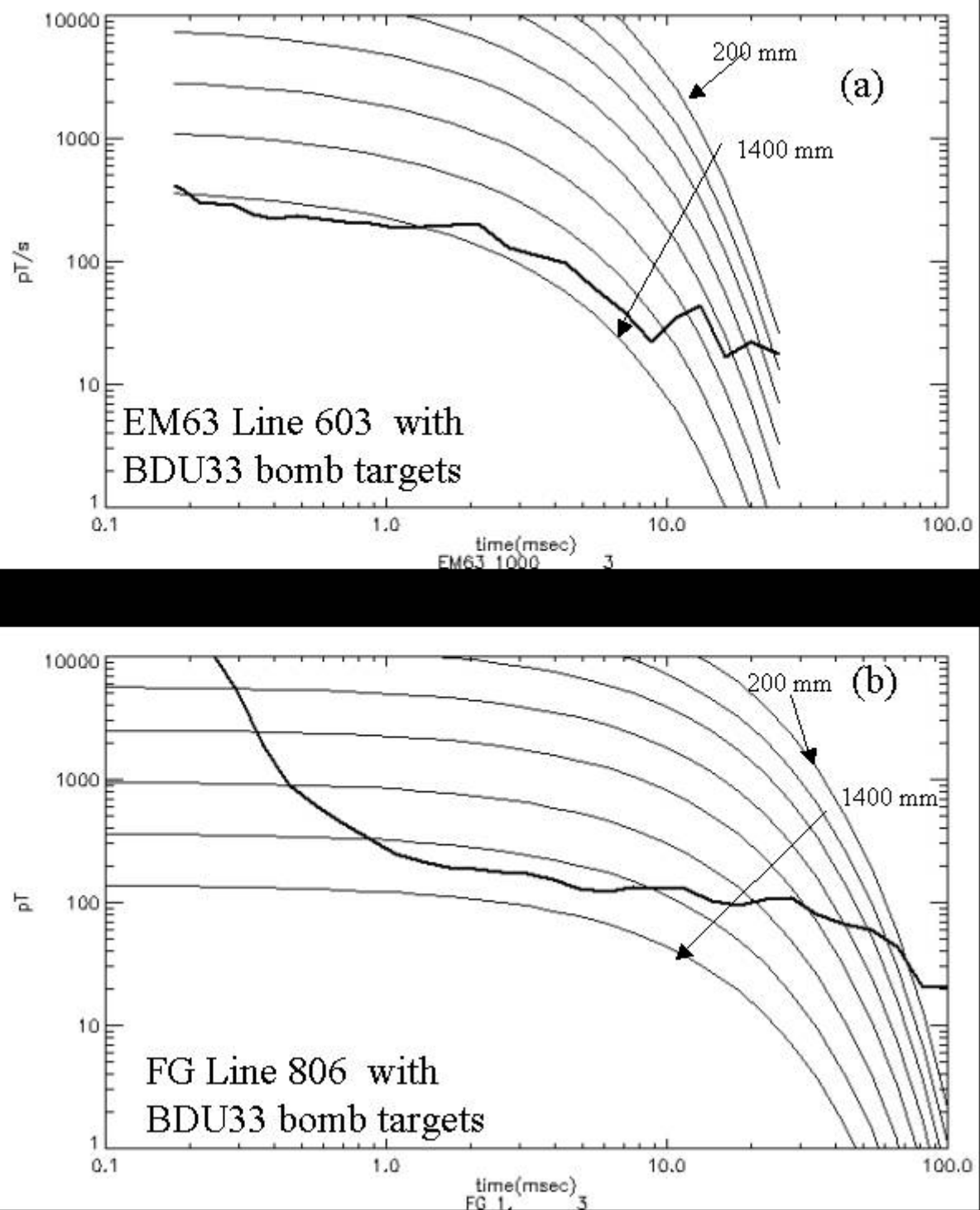


Figure 47 – Modeled response of the BDU33 practice bomb target oriented horizontally, to two EMI systems.

Thick lines are observed noise levels on the EMIT test pit.

The suite of models (thin black lines) are late-time responses computed for target depth to base, below the pit cover. Add 425mm or 395 mm for total depth below EM63 or BEAMOD™ transmitter coil, respectively.

Range of depths below pit cover is: 200, 300, 400, 530, 680, 880, 1110, 1400mm.

7.6. Summary of performance advantage in depth detection

The performance advantage of the B-field sensors over the EM63 in terms of depth of detection in the presence of instrumental and geological noise may be summarized thus:

- a. Copper pipe: The SQUID has an advantage of 1700 mm vs 1400mm for the EM63 and fluxgate (20% deeper - applies only at short window times <1 msec, which is not of high value).
- b. 40mm cannon shell: The fluxgate sensor has an advantage of 780 mm vs 530mm for the EM63 (47% deeper).
- c. 75mm cannon shell: The fluxgate sensor has an advantage of 1110 mm vs 780mm for the EM63 (42% deeper).
- d. BDU33 practice bomb: The fluxgate sensor and EM63 have comparable depth sensitivity at the intermediate time range 5-10 msec, but the fluxgate is strongly superior at late times of order 20 msec, having a computed depth detection advantage of about 780 mm vs 480 mm for the EM63 (50% deeper).

In terms of window of detection, the fluxgate sensor shows increases of between 25% and 125% in late-time detection for steel targets (strongest increase for largest targets), but a decrease in window of detection for the copper pipe target.

In addition the B-field sensors are demonstrated to provide three-component data which Section 10 shows provides enhanced precision in location and target orientation.

8. FLUXGATE MAGNETOMETER RESULTS OVER NEWHOLME UXO TEST RANGE (ARMIDALE, NSW AUSTRALIA)

8.1. Geological background

The Newholme UXO test range is 13 km north of Armidale, northern NSW, Australia. It is agricultural land used for both grazing and crops by the University of New England (Armidale) School of Agriculture. The soil cover ranges from zero to a few meters thick, over granite. In Appendix C it is seen that inert UXOs have been emplaced at depths up to 4 m.

All profiles at Newholme were acquired with the BEAMOD Mk2 system, transmitter current 12 A, and a fluxgate sensor. While the original intention of the project was to test both the fluxgate and the SQUID sensors at Newholme, the SQUID was not available for rental during the month of May when field trials were scheduled. Previous trials at the EMIT test pit have established that the SQUID has no practical advantage over the fluxgate magnetometer in the BEAMOD™ configuration; hence omission of the SQUID at this site does not affect the outcome of the project.

Figure 48 and Figure 49 show the geological background signal in two profiles which do not pass over a metallic target. The two profiles have comparable amplitude envelopes over three meters of profile. Figure 50 shows for comparison a profile over the EMIT test pit, plotted on the same scales; it is clear that the geological signal variation at the EMIT test pit is several-fold stronger and more variable over the length of the profile. As noted in discussion in Sections 6.3 and 7.2, the strong geological signal at the EMIT test pit is attributed to the presence of iron oxides in the soil, rather than electrical conductivity. The lower geological signal at the Newholme test range makes the detection of deep targets easier than at the EMIT test pit.

Figure 51 shows the profile obtained over a 40 mm shell at the same location as Figure 48. Amplitudes are smaller than those observed at the EMIT facility (Figure 43) but the target item used at Newholme appears to be a different type of 40 mm shell compared with that supplied to EMIT.

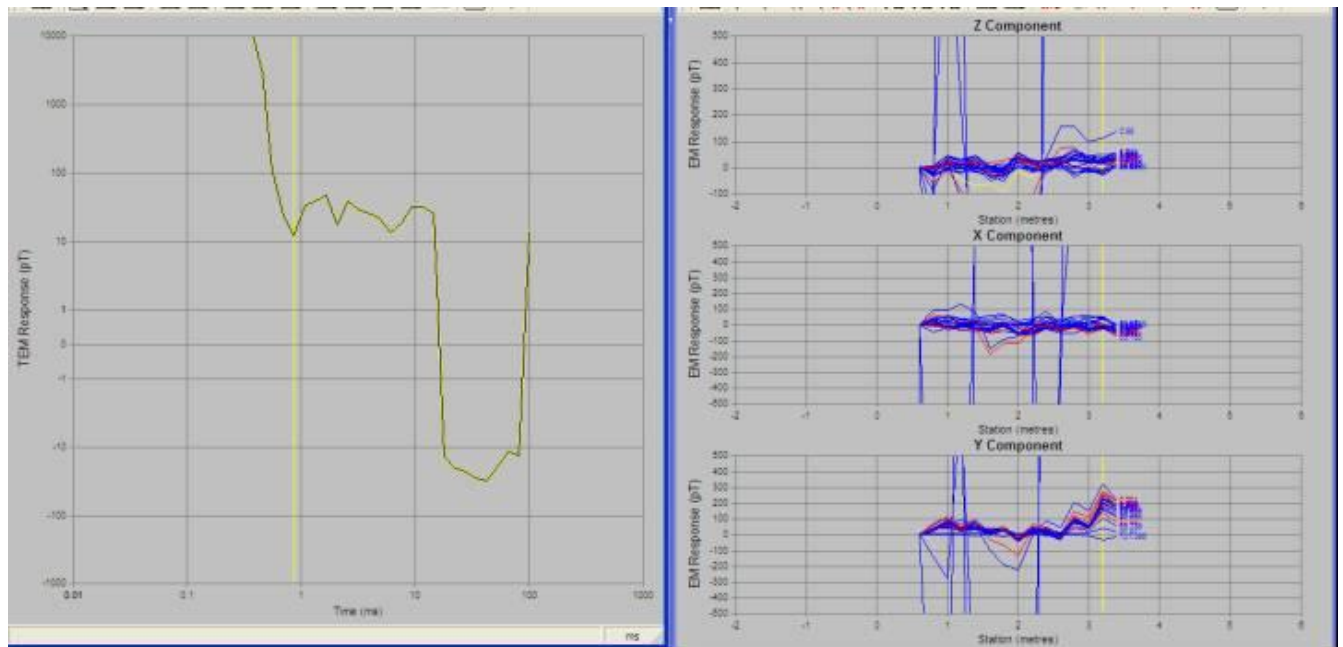


Figure 48 – Profile with BEAMODTM Mk2, transmitter current 12A, and fluxgate sensor at south-west corner of Newholme test site, without a target (File FG702)
Right: Profile of length 3 m. Left: Decay curve at station 3.4.

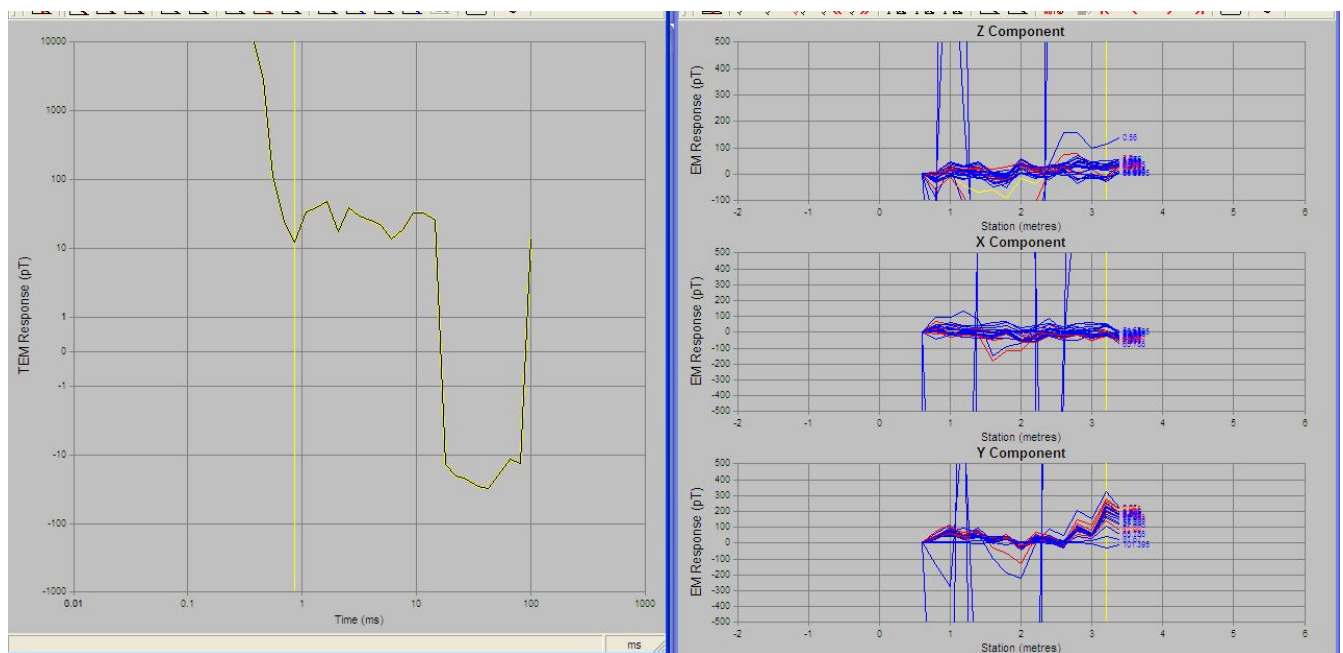


Figure 49 – Profile with BEAMODTM Mk2 and fluxgate sensor at east edge of Newholme test site, without a target (File FG712).
Right: Profile of length 8 m. Left: Decay curve at station 3.4.

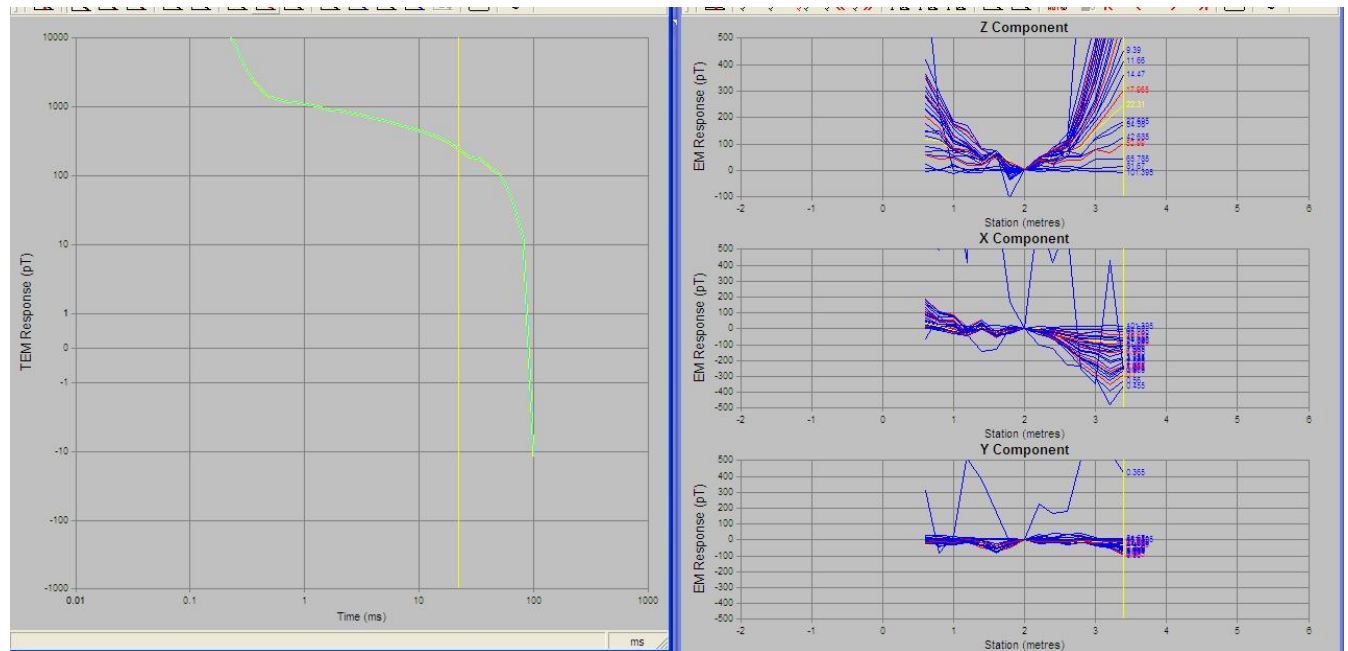


Figure 50 – Profile with BEAMOD™ Mk2 and fluxgate sensor at EMIT test pit, without a target (File FG804).

Right: Profile of length 3 m. Left: Decay curve at station 3.4.

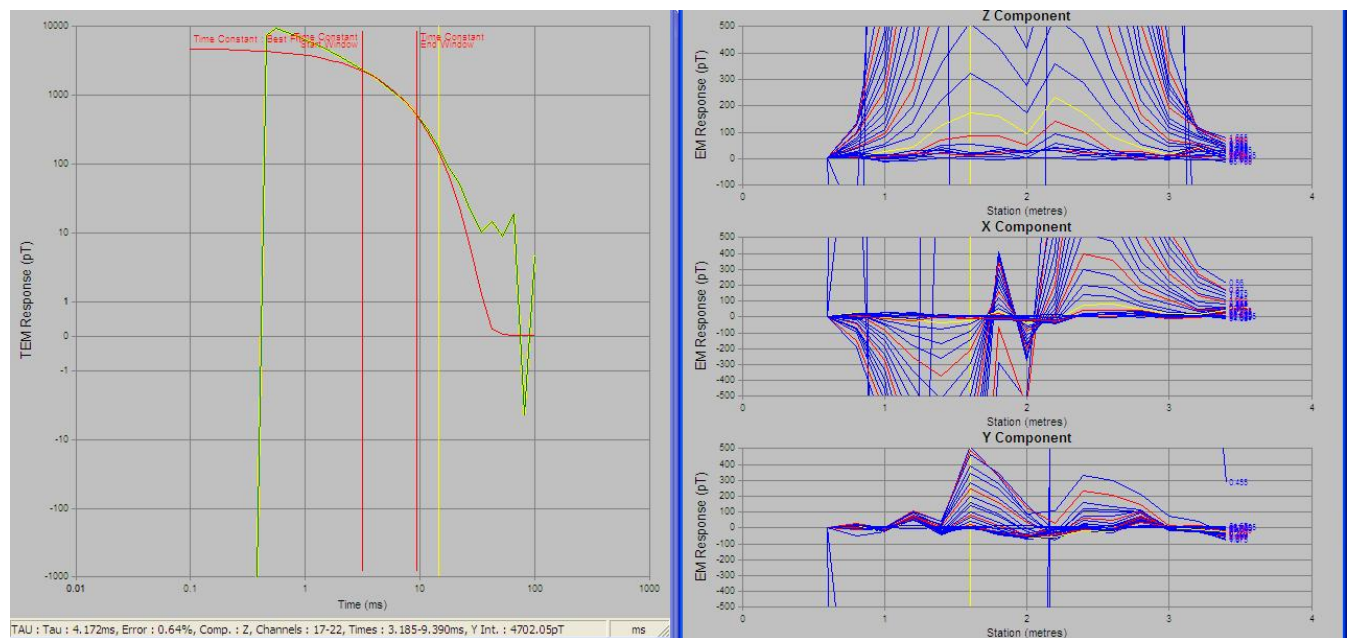


Figure 51 – Profile with BEAMOD™ Mk2 and fluxgate sensor at Newholme test range, same location as Figure 48 with a 40 mm shell as target

The target is on ground surface below station 2.0, oriented horizontal and parallel with profile (File FG704).

Right: Profile of length 3 m. Left: Decay curve at station 1.6.

8.2. Response of rocket heads and BDU33 practice bombs

Figure 52, Figure 53 and Figure 54 show profiles over three PWH rocket heads. The rocket heads have diameter 2.75 inch or 75 mm, and are similar in size to a 75 mm cannon shell. The three rocket heads are all at depth 500 mm below ground surface, being horizontal perpendicular to the profile, horizontal parallel with, and vertical below, the profiles. In each case the three-component data is successfully obtained, and the shape and amplitude of Z-component data increase in sequence as expected from previous observation and model studies on steel shells.

Figure 55 and Figure 56 show profiles acquired over two BDU33 practice bombs. The first is at depth 0.8 m and is clearly detectable. However the deeper BDU33 at 2 m is not detected, a result in keeping with predictions developed in Section 7.5 and Figure 47. (The BEAMOD™ system used on these targets had a transmitter of reduced height due to equipment breakage; the transmitter coil was 115 mm above ground level, reduced from 395 mm above ground in preceding data.

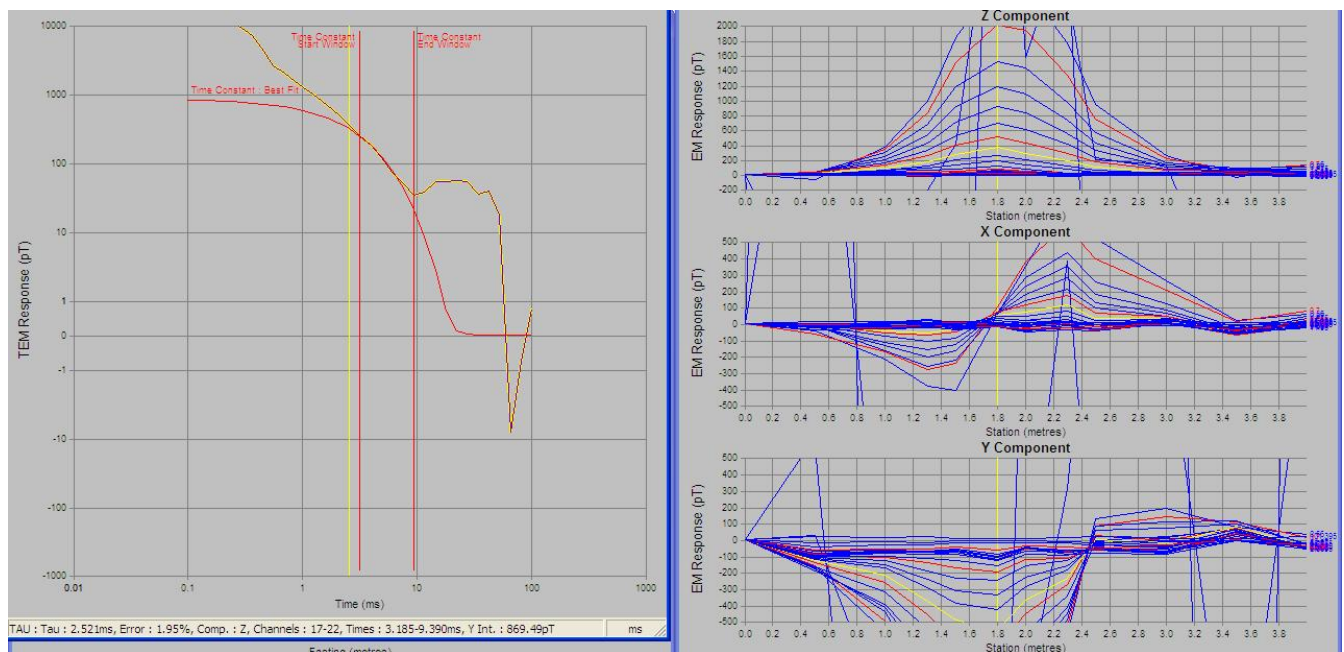


Figure 52 – Profile with BEAMOD™ Mk2 and fluxgate sensor at Newholme test range, target 11 (PWH rocket head) at depth 500 mm, notionally below station 2.0. Observed data has been leveled and stripped.

The target is horizontal, axis perpendicular to the profile (File FG705).

Right: Profile plot.

Left: Decay curve at station 1.8. The oscillatory nature of the decay curve for times > 10 msec is due to limitations of the stripping process at late times/low amplitudes.

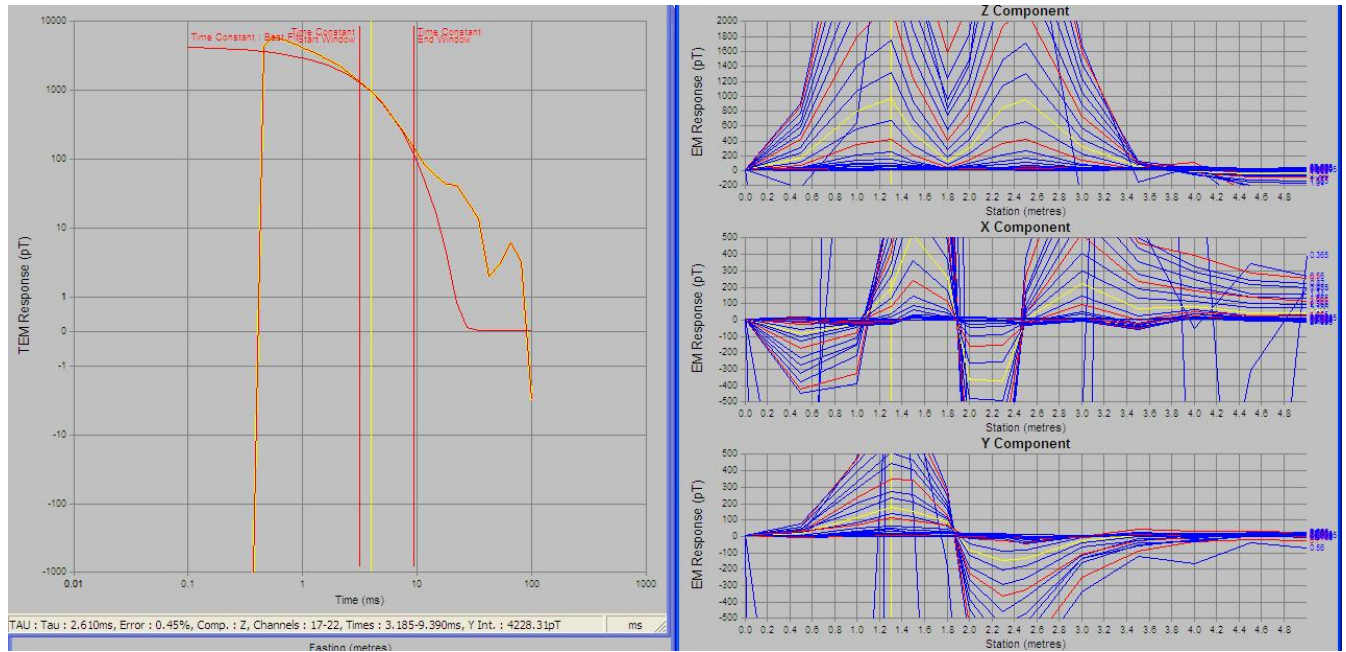


Figure 53 – Profile with BEAMOD™ Mk2 and fluxgate sensor at Newholme test range, target 12 (PWH rocket head) at depth 500 mm, notionally below station 2.0. Observed data has been leveled and stripped.

The target is horizontal, axis parallel with the profile (File FG706).
Right: Profile plot. Left: Decay curve at station 1.3.

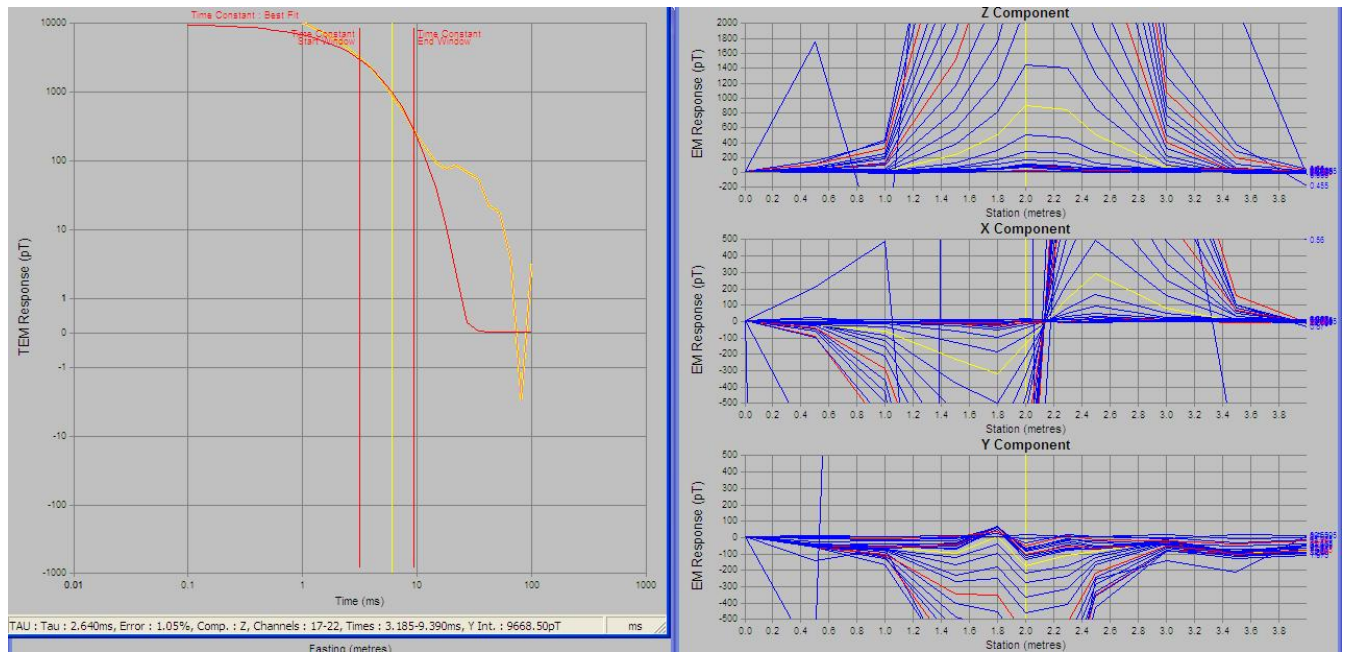


Figure 54 – Profile with BEAMOD™ Mk2 and fluxgate sensor at Newholme test range, target 13 (PWH rocket head) at depth 500 mm, oriented vertical, notionally below station 2.0. Observed data has been leveled and stripped.

The target is vertical, nose down (File FG707).
Right: Profile plot. Left: Decay curve at station 2.0.

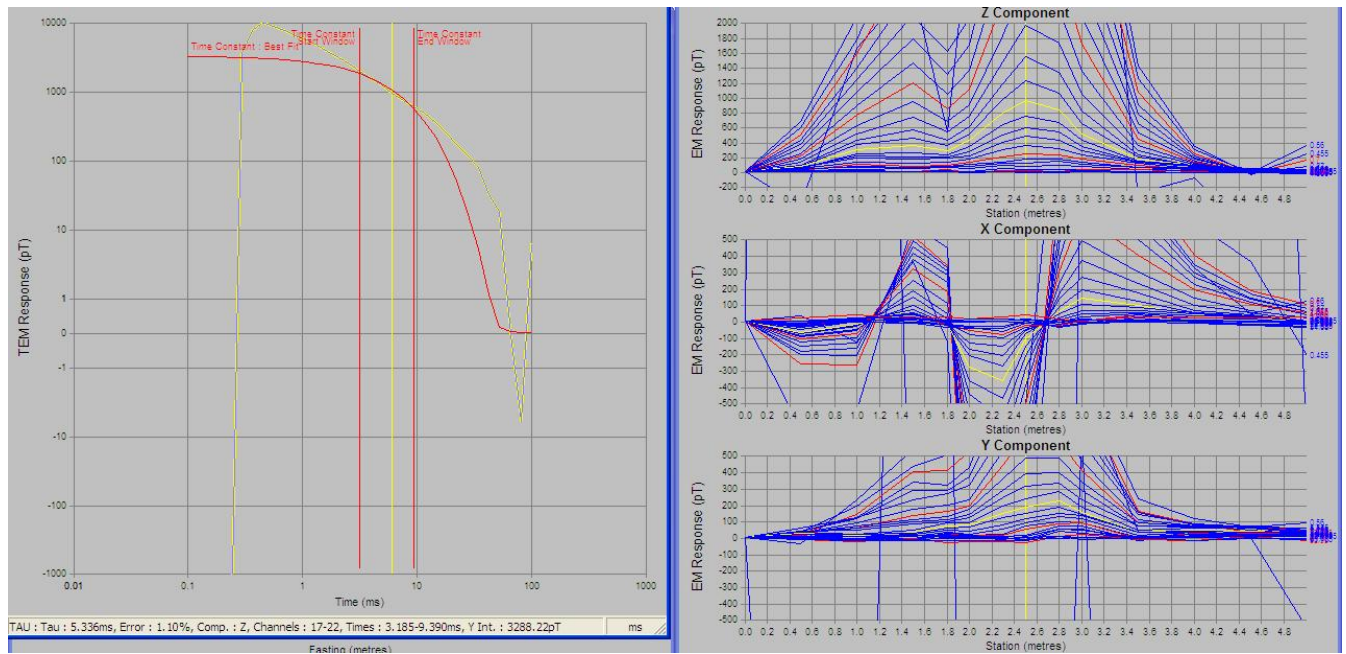


Figure 55 – Profile with BEAMOD™ Mk2 and fluxgate sensor at Newholme test range, target 34 (BDU33 practice bomb) at depth 800 mm, notionally below station 2.0
The target azimuth is 75 deg from the profile, with dip 20 deg. (File FG708).
Right: Profile plot. Left: Decay curve at station 2.5.

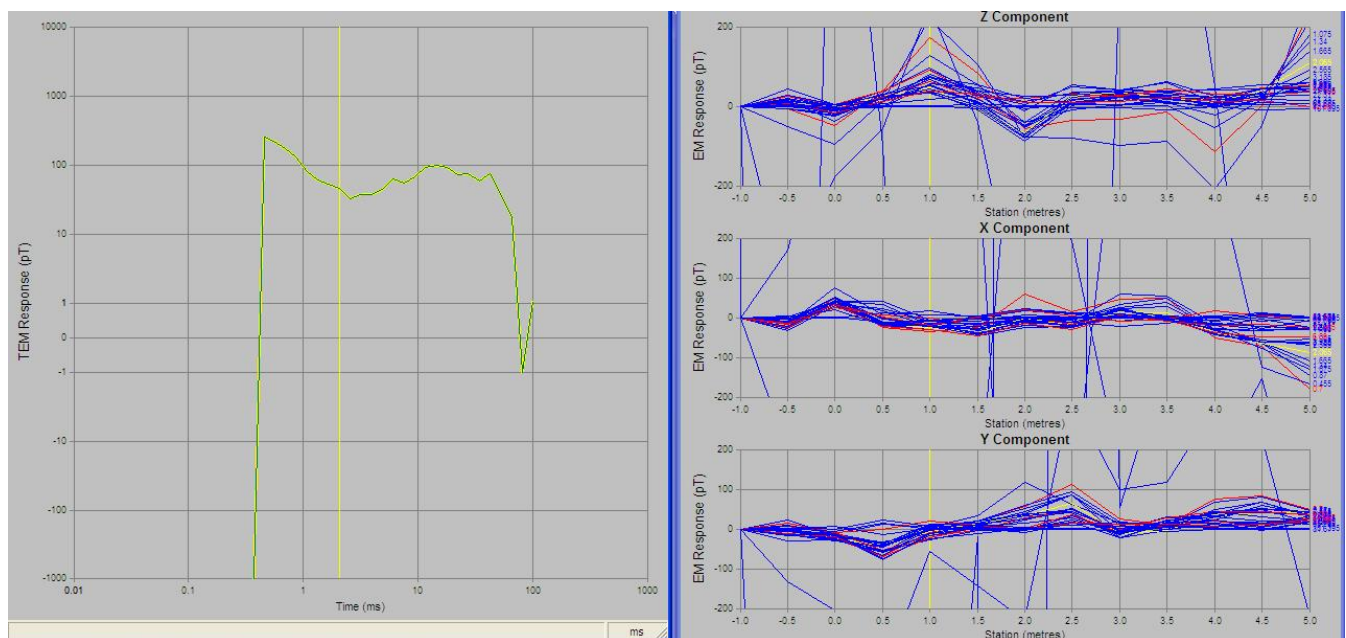


Figure 56 – Profile with BEAMOD™ Mk2 and fluxgate sensor at Newholme test range, target 33 (BDU33 practice bomb) at depth 2 m, notionally below station 2.0
The target azimuth is 75 deg from the profile, with dip horizontal. (File FG709).
Right: Profile plot. Left: Decay curve at station 2.5.

8.3. Response of 500 lb Mk 82 bombs

Finally we show responses over two 500 lb Mk 82 bombs. Figure 57 shows the very strong 3-component response over a Mk 82 bomb at depth 0.6 m. Figure 58 shows response of the same type of bomb, at depth 2.6 m; the large metallic target

is clearly detected, although profiles show that the target signature is of similar amplitude to the noise envelope.

This is a pleasing result for the BEAMOD™ system since it demonstrates an instance where useful 3-component EMI data can be acquired over a target at 2.6 m depth.

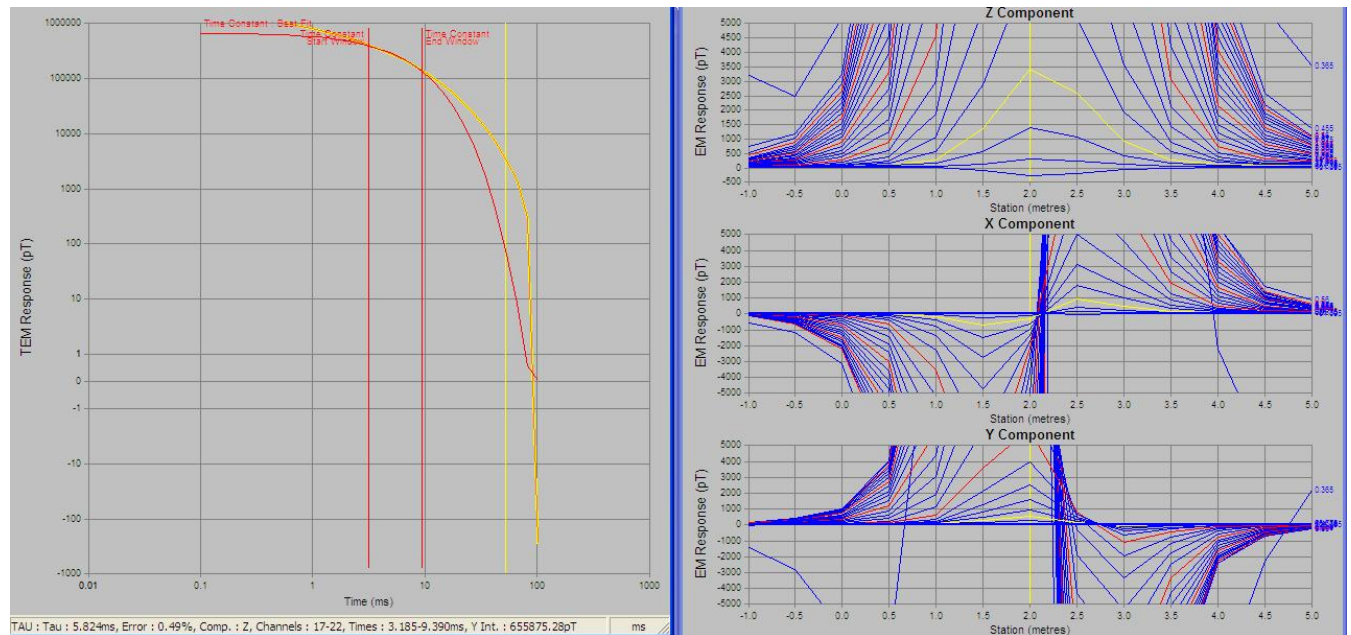


Figure 57 – Profile with BEAMOD™ Mk2 and fluxgate sensor at Newholme test range, target 21 (Mk 82 bomb, 500 lb) at depth 600 mm, notionally below station 2.0. The target azimuth is 45 deg from the profile, with dip 0 deg. (File FG710). Right: Profile plot. Left: Decay curve at station 2.0.

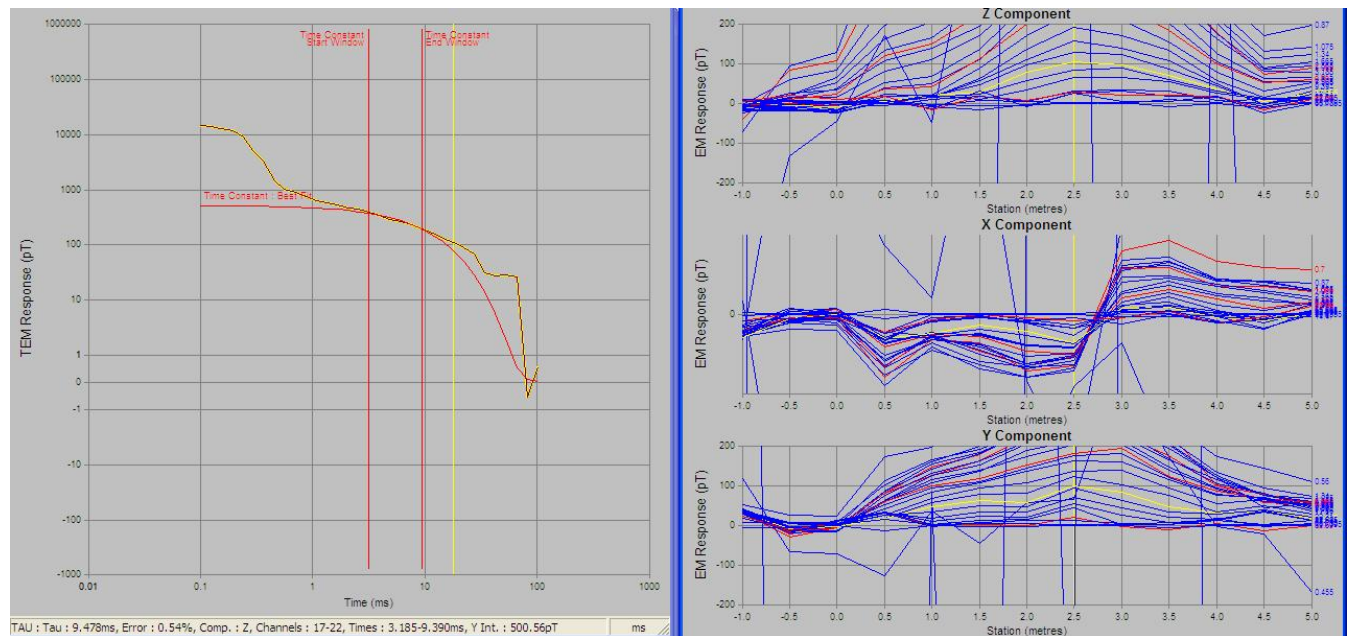


Figure 58 – Profile with BEAMOD™ Mk2 and fluxgate sensor at Newholme test range, target 4 (Mk 82 bomb, 500 lb) at depth 2.6 m, notionally below station 2.0
The target azimuth is 75 deg from the profile, with dip 20 deg. (File FG713).
Right: Profile plot. Left: Decay curve at station 2.5.

8.4. Response of a target acquired from a moving platform

It is not the aim of this one-year project to develop a UXO detection system suitable for acquisition while in continuous motion. However in response to a request from SERDP following the IPR in February 2006, some examples of Newholme data were acquired with a continuously moving system.

Continuous data acquisition presents a demand for a trade-off between speed of ground coverage and transmitter frequency. A low transmitter frequency demands a low profiling speed in order to get sufficient useful stacking of transmitter pulses over a given target. The transmitter frequency of 2.08 Hz used in all studies with BEAMOD™ thus far (apart from under power lines) is designed for maximum target discrimination capability by providing time windows to 100 msec. For continuous recording a transmitter frequency of order 8 Hz is likely to be preferable as it provides time windows to 25 msec but has a four-fold faster stacking rate.

Another possible limitation occurs with B-field sensors where any change in orientation of the sensors in the Earth's magnetic field produces large very low-frequency shifts in the output of the sensor; these shifts can drive the sensor electronics off scale. We note that these problems are soluble as demonstrated by Lee et al (2001) who developed a prototype platform and signal processing allowing use of a SQUID magnetometer as the EMI sensor in an airborne EM survey.

In this study, we demonstrate with the fluxgate sensor that measurement of munitions responses is feasible from a continuously-moving platform, but detailed design and optimization of measurement from a moving platform is left to future years of the project.

Figure 59 shows a profile over a PWH rocket head conventionally-acquired, i.e. with the BEAMOD™ system stationary for 64 stacks at each station. Figure 60 and Figure 61 show the same profile acquired with the BEAMOD™ system in continuous motion at 0.2 m/sec. Figure 6 shows a picture of the system mounted on a sled as used for these continuous-movement tests.

For data acquisition in continuous motion, the SMARTem receiver records a continuous full waveform for the entire profile (duration about 30 sec). This continuous data record is then post-processed similarly to that for an airborne EM profile, to yield stacked data sampled at profile intervals of 0.5 m. For each post-processed station, raw data from a total of 1 metre of profile is stacked and converted to a single result using a tapered stacking algorithm. This approach does not overly smooth profiles and allows sharp changes in the EMI response along the profile to be observed without unnecessary smoothing. For a slower traverse, longer periods of data could be used with a resulting improvement in quality.

Figure 60 and Figure 61 show the continuous motion data after processing for transmitter frequencies of 8.33 Hz and 2.08 Hz respectively. Comparison of the decay curves for Figure 59, Figure 60 and Figure 61 shows that the observed data decay curve degrades to noise at levels in the range 100- 500 pT for both the stop-start mode and the continuous motion with transmitter frequency 8.33Hz. However with continuous motion and the lower transmitter frequency of 2.08 Hz, the reduced stacking available gives a distinct increase in the noise floor of about one order of magnitude.

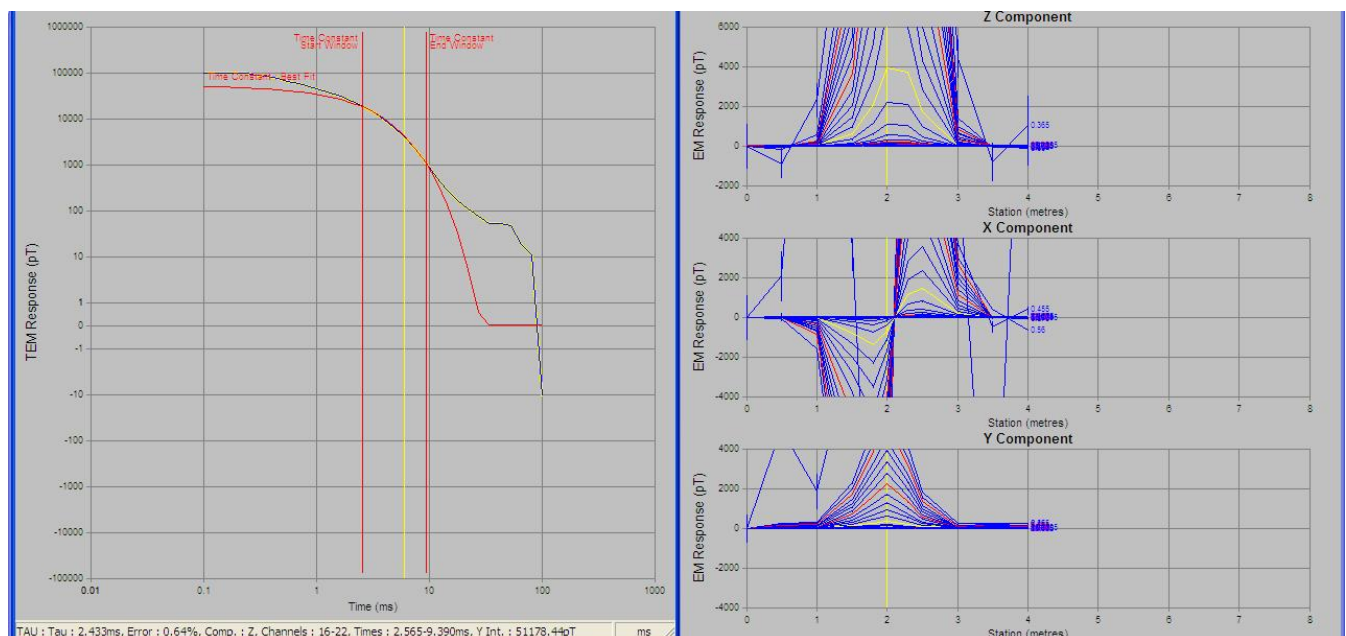


Figure 59 – Conventional stop-start profile with BEAMOD™ Mk2 and fluxgate sensor at Newholme test range, target 13 (PWH rocket head 2.75 inch, oriented vertically). Depth to target is 0.5 m, notionally below station 2.0. Transmitter frequency 2.08 Hz; current 12 A. (File FG719).
Right: Profile plot. Yellow curve is time window 7 msec. Left: Decay curve at station 2.0.

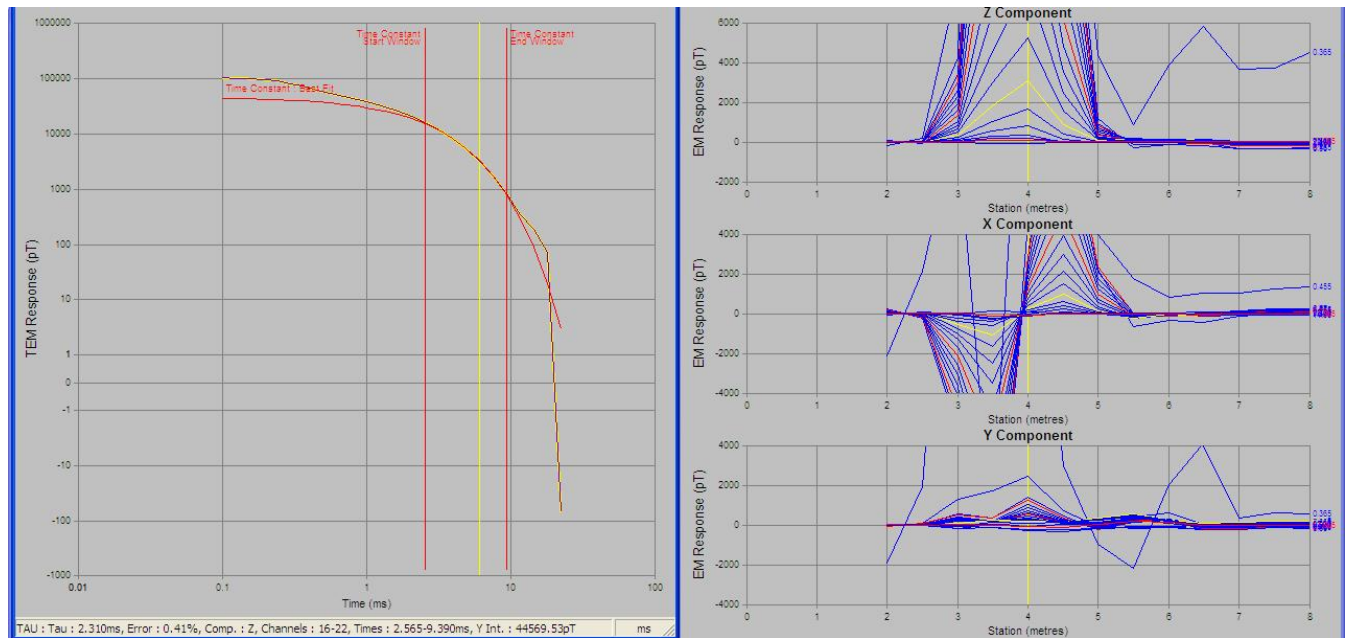


Figure 60 – Continuous motion profile with BEAMOD™ Mk2, medium frequency, and fluxgate sensor at Newholme test range, target 13 (PWH rocket head 2.75 inch, oriented vertically). Station distance is arbitrary, being based on time from commencement of the continuous profile. Depth to target is 0.5 m. Transmitter frequency 8.33 Hz; current 12 A. (File FG721). Right: Profile plot. Yellow curve is time window 7 msec. Left: Decay curve at station 4.0.

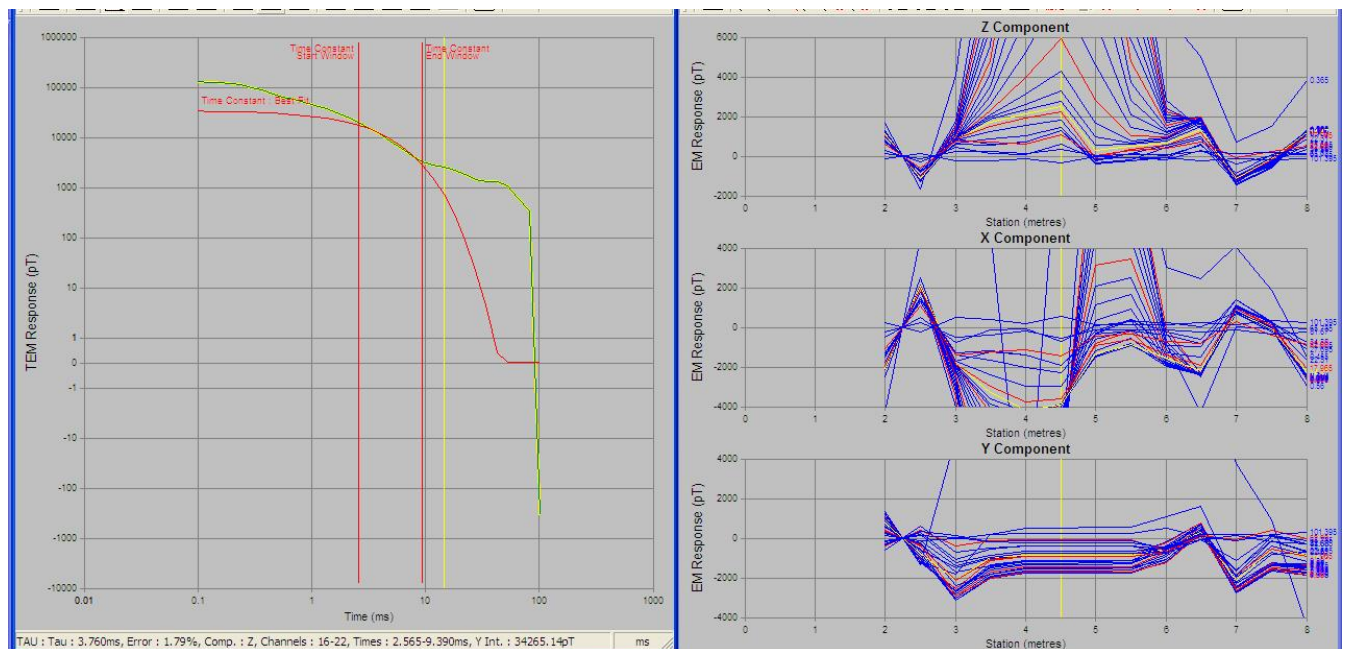


Figure 61 – Continuous motion profile, as for Figure 60 but with a low transmitter frequency of 2.08 Hz (File FG720). Right: Profile plot. Yellow curve is time window 7 msec. Left: Decay curve at station 4.5.

Figure 62 shows similar continuous-motion profiles at the two transmitter frequencies, for a profile shifted 5 m east, i.e. without a munitions target below. As with the previous figures, the frequency 8.33 Hz allows recovery of a smooth profile from continuous-motion recording, while the reduced stacking available with a transmitter frequency of 2.08 Hz produces a disproportionately-large increase in point to point noise.

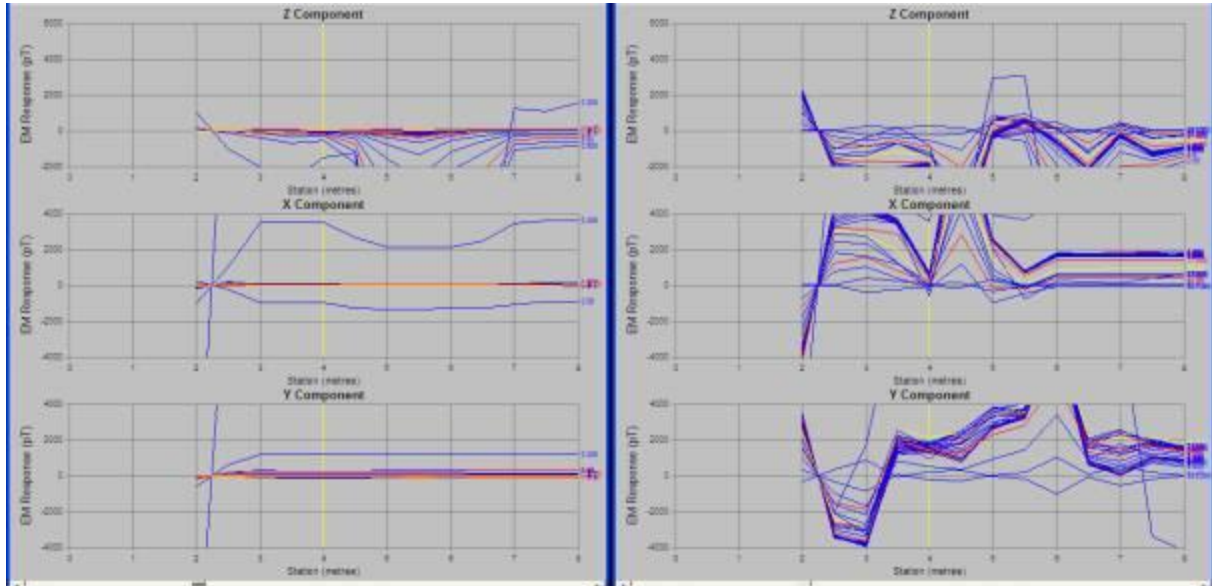


Figure 62 – Continuous motion profiles with BEAMOD™ Mk2, at Newholme test range, no target below the profile.

Station distance is arbitrary, being based on time from commencement of the continuous profile.

LEFT: Profile acquired with transmitter frequency 8.33 Hz.

RIGHT: Profile acquired with transmitter frequency 2.08 Hz.

8.5. Conclusions on response of a target acquired from a moving platform

The previous five figures successfully demonstrate that data acquisition with a B-field sensor is attainable. The use of full-waveform processing is a necessary part of this (available with the existing design of the SMARTem receiver used in the project). Although the stacking time for the two frequencies differs only by a factor of four, the noise level differs by about a factor of 10 which indicates that a threshold number of stacks is necessary for useful data to be obtained in continuous-motion mode. We have not attempted to investigate the threshold in this first year of the project, but note that the noise floor for the continuous profiles at 8.33 Hz (receiver time windows to 22.2 msec) is similar to that obtained with stop-start data acquisition.

9. COMPARISON OF POWER-LINE NOISE REJECTION WITH BEAMOD™ AND EM63

9.1. EM63 Profile

EMI profiles were conducted under high-tension power lines at the Mundaring Cemetery, 4km south of the EMIT property. The location facilitated acquiring profiles across a road perpendicular to the azimuth of the power lines, without interference of vehicle traffic. Figure 63 shows the two instruments EM63 and BEAMOD™ Mk2 in use at the site.



Figure 63 – BEAMOD™ Mk 2 and EM63 instruments in use under high-tension power lines
Left: The BEAMOD™ Mk 2 instrument in use under high-tension power lines.
Right: The EM63 instrument in use at the same site.

As an aid to quantifying noise, a 40 mm cannon shell was placed on the surface, oriented parallel with the profile, immediately under the power lines (16 m mark).

The EM63 operated at 4.5 Hz, and data was sampled at 0.1 m (200 msec) intervals. In order to reduce 50 Hz noise and compare with similar acquisition specifications on the BEAMOD, the EM63 data was smoothed over pairs of profile points, thus giving data averaged over 400 msec.

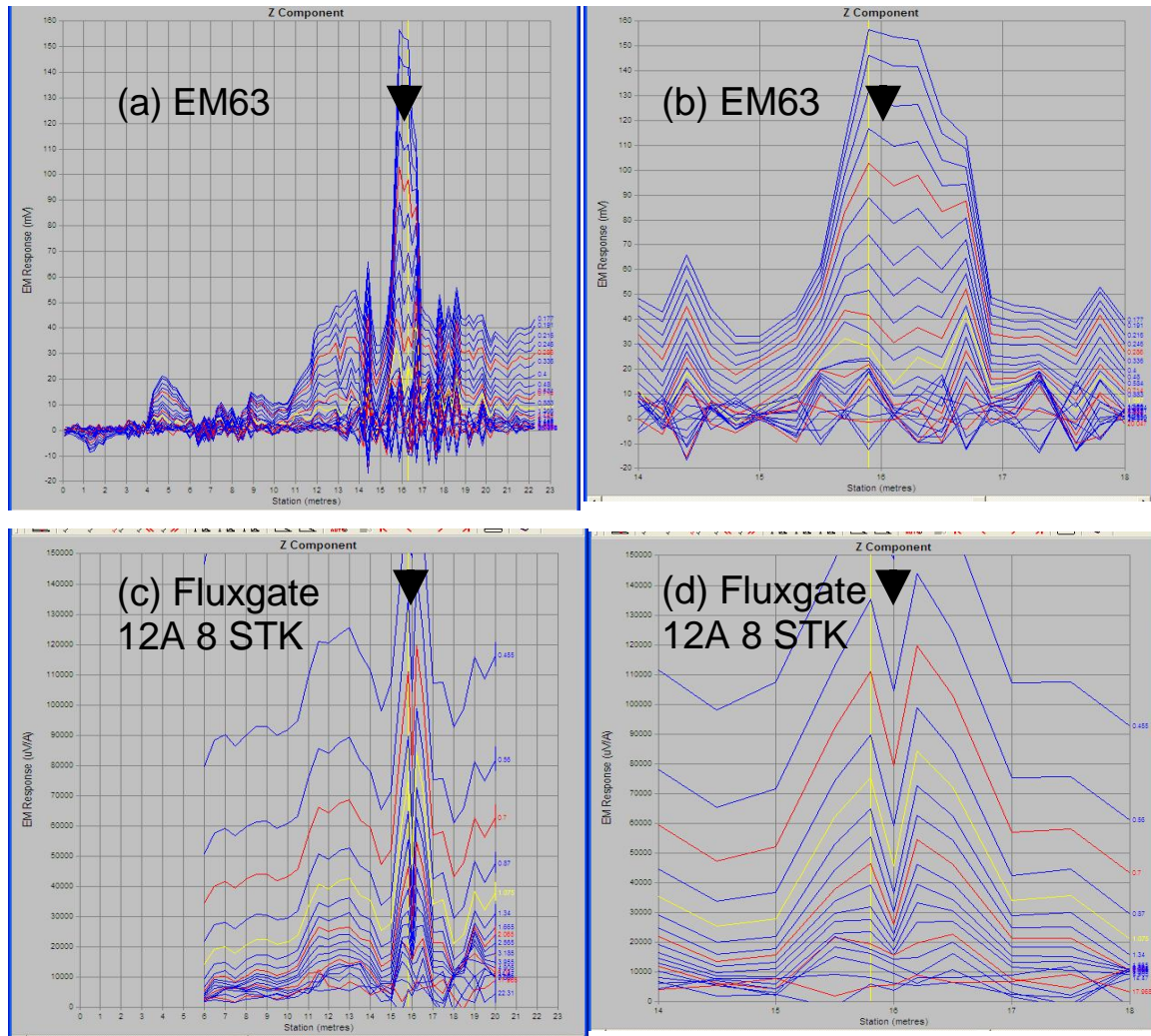


Figure 64 – Profiles acquired with the EM63 and BEAMOD™ Mk2 with fluxgate sensor, under power lines

(a) Profile of length 23 m acquired with the EM63 instrument, transmitter moment 445 A.m^2 . The arrow at 16 m is the location of a 40mm cannon shell on the ground, which is directly below the power lines. Data is averaged over 0.2 m or 400 msec.

(b) As for (a), using an expanded scale showing the profile from 14 to 18 m. The profile in yellow is for time window 1 msec. The noise envelope associated with 50Hz power-line noise is greater than 50% of the amplitude of the target response at time 1 msec.

(c) Profile of length 23 m acquired with the BEAMOD™ Mk2 with fluxgate sensor, transmitter frequency 8.33 Hz, transmitter current 12 A, moment 180 A.m^2 . Data is averaged over 480 msec (8 stacks at 8.33 Hz). The arrow at 16 m is the location of a 40mm cannon shell on the ground, which is directly below the power lines.

(d) As for (c), using an expanded scale showing the profile from 14 to 18 m. The profile in yellow is for time window 1 msec. The noise envelope associated with 50Hz power-line noise is of order 10% of the amplitude of the target response at time 1 msec.

Figure 64 (a-b) shows the EM63 profile obtained. The noise induced by the power lines produces a noise level such that time domain samples at windows later than 1 msec are of no value. (This may also be compared with Figure D21 in Appendix D, for the same target on the EMIT test pit).

9.2. Fluxgate Sensor Profile

Figure 64 (c-d) shows the equivalent profile acquired with the BEAMOD™ Mk 2 system, with fluxgate sensor, and transmitter current of 12 A. The transmitter was operated at 8.33 Hz giving a maximum window delay time of 23 msec, chosen to be comparable with the EM63. The SMARTem™ tapered stacking algorithm was applied over 8 stacks, or a total sample time of 480 msec, chosen to be comparable with the averaging time used for the EM63 plots above.

We can obtain a semi-quantitative, visual estimate of noise level by noting the envelope (maximum to minimum amplitude) on late-time channels where signal response has decayed to be near zero, thus leaving point-to-point variations along a profile to be indicators of noise. This noise envelope is compared with target anomaly amplitudes for a chosen reference time; we use time window 1 msec (yellow line in Figure 64 and Figure 65) as our reference in this comparison. Figure 65c is an example where late-time channels show negligible noise on such visual examination. Visual estimates of noise on Figures 64b and 64d show that the noise envelope attributable to 50Hz noise is of order 50% of the target amplitude at time 1 msec in the case of the EM63, and only 10% of the target amplitude at time 1 msec in the case of B-field measurements with the BEAMOD system. While it would be possible to use a roughening filter to extract the noise on a more quantitative basis, we believe this visual comparison to be a clear demonstration of the superior performance of the BEAMOD system, and sufficient for the purpose since noise envelopes associated with 50 Hz are expected to be variable, and hence we believe a more quantitative estimate of this type of noise would not add to the state of knowledge.

The noise level in (d) for time window 1 msec is of order 10% of the signal level at time window 1msec (compared with 50% for the EM63). This result represents a 5:1 improvement in 50Hz noise reduction for the BEAMOD™ system, operating over similar stacking times. This result was achieved using a transmitter moment of $180\text{A}\cdot\text{m}^2$, compared with the EM63 moment of $445\text{A}\cdot\text{m}^2$. (The output power of the two systems is comparable, because the EM63 uses an effective 25% duty cycle).

Thus we see that the signal to noise ratio for the BEAMOD™ system with smart (tapered) stacking is dramatically improved relative to that for the EM63 system. The improved signal to noise is further enhanced by the fact that the fluxgate sensor enables acquisition of three-component EMI data as shown in Fig. 9.3a.

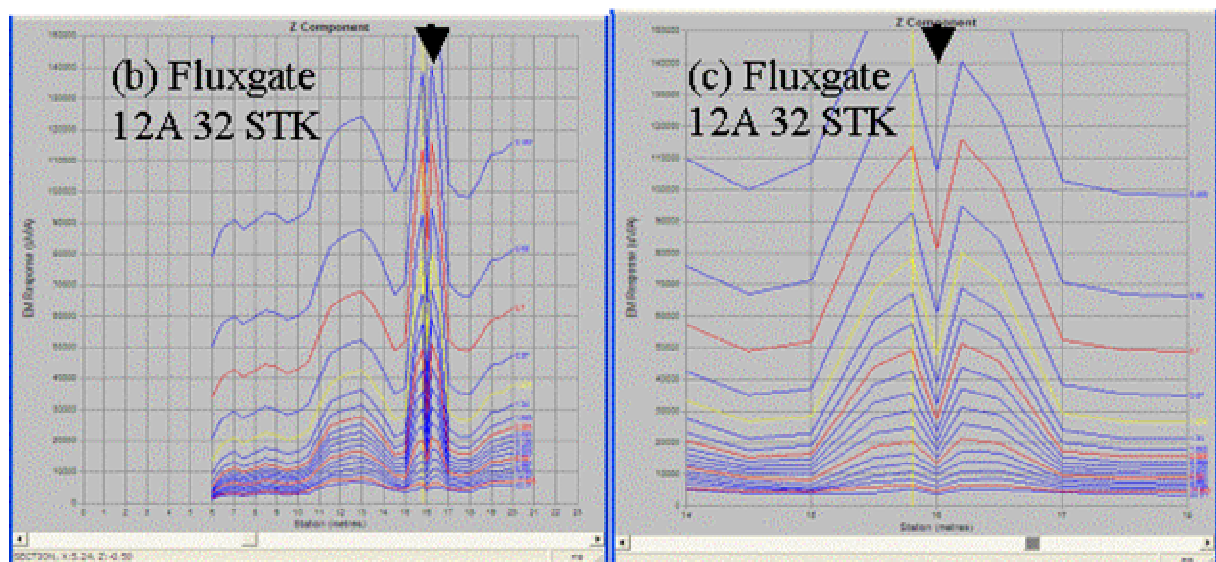
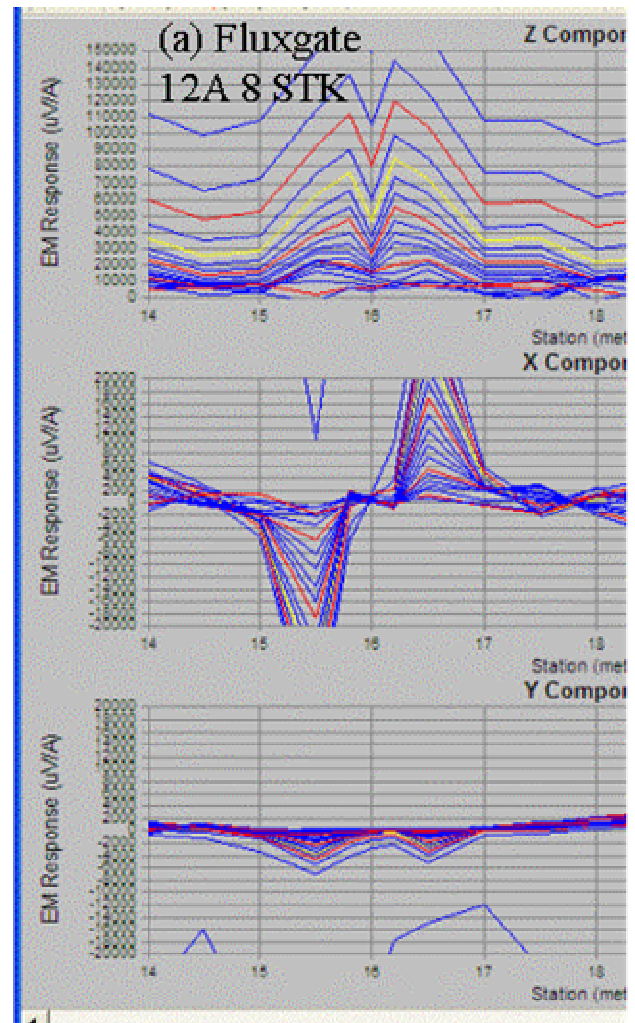


Figure 65 Three component profile acquired with the BEAMOD™ Mk2 with fluxgate sensor under power lines.

(a) Same profile as Figure 64d, with addition of X and Y components.

(b) Same profile as Figure 64(c), acquired using 32 stacks (x4 increase in averaging).

(c) As for (b), but with expanded scale. The noise threshold is below geological noise.

In Figure 65 (b-c) the signal to noise achievable by using a four-fold longer stacking time with the BEAMOD™ system. The noise associated with the power lines is below the level of recognition, and below the point to point noise associated with variations in geological background. We claim conservatively a 20:1 improvement in 50 Hz noise reduction for the BEAMOD™ system, operating over a four-fold increase in stacking times. Such long stacking times are unlikely to be achievable in a moving system, but the result illustrates that when superior discrimination is required, the BEAMOD™ system can be applied with great advantage in the immediate vicinity of noisy power lines.

Finally, we show in Figure 66 the profile obtained using the same BEAMOD™ Mk 2 and fluxgate sensor, except the transmitter frequency is at the low value of 2.08Hz (as used in tests on the EMIT test pit). The lower transmitter frequency results in poorer rejection of 50Hz noise for the same number of stacks, but it is still superior to that obtained with the EM63.

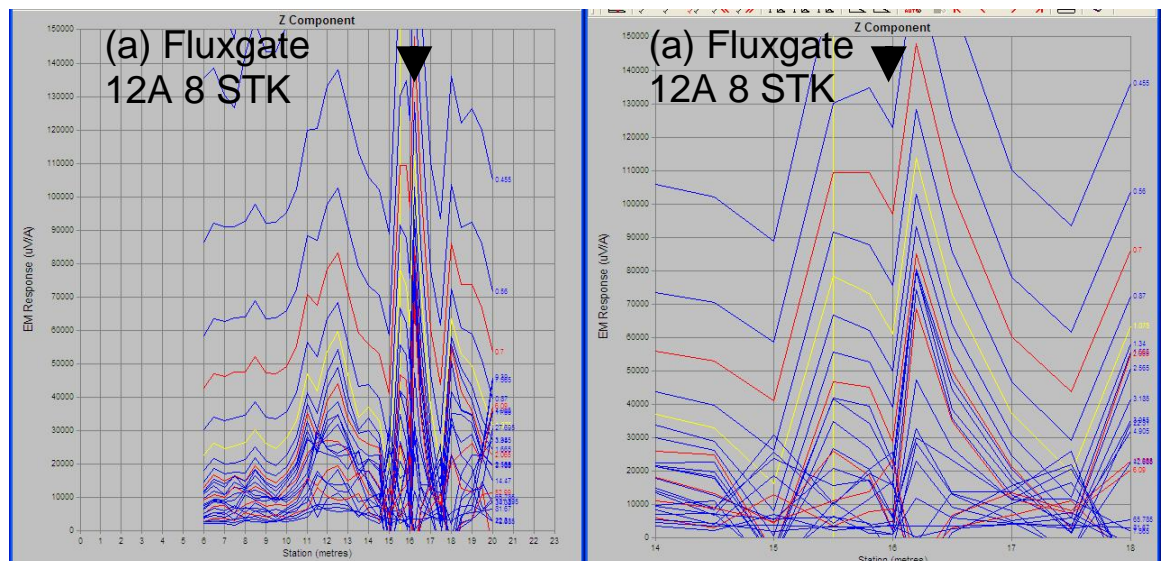


Figure 66 Profiles acquired with the BEAMOD™ Mk2 with fluxgate sensor, under power lines, at low transmitter frequency.

(a) Profile as for Fig. 9.2c, but with transmitter frequency reduced to 2.08 Hz.

(b) As for (a), using an expanded scale showing the profile from 14 to 18m. The profile in yellow is for time window 1msec. The noise envelope associated with 50Hz power-line noise is of order 30% of the amplitude of the target response at time 1msec.

9.3. SQUID Profile

Figure 67(a-b) duplicates Figure 64 to show the EM63 profile under the power lines as a comparison with a profile using the SQUID sensor. Figure 67(c-d) shows the equivalent profile acquired with the BEAMOD™ Mk 2 system, with the SQUID sensor, and transmitter current of 1.2A.

The SQUID sensor was found to suffer additional leveling or drift problems in this 50Hz noise environment compared to its behavior in the low-noise environment of the EMIT test pit. Part of the profile was acquired using a transmitter current of 3.5A, but in the vicinity of the power line drift of the zero

level on the receiver was such that the transmitter current had to be reduced to 1.2A (moment 18 A.m²) in order to keep the SQUID output signal on scale on the SMARTem receiver.

The transmitter was operated at 2.08Hz, as was used for all measurements at the EMIT test pit. This low transmitter frequency does not allow a direct comparison with the EM63 instrument (hence measurements with the fluxgate sensor discussed in the previous Section used the higher frequency of 8.33Hz). The SMARTemTM tapered stacking algorithm was applied over 10 stacks, chosen to be comparable with the averaging used for the smoothed EM63 plots above, but the averaging time at this low transmitter frequency is a factor of 5 longer. The noise level in (d) for time window 1msec is of order 50% of the signal level at time window 1msec, which is comparable with the noise level experienced by the EM63. Note however that the BEAMODTM Mk2 transmitter used with the SQUID here has a moment of 18 A.m² and is over an order of magnitude less than that of the EM63.

We conclude that although the SMARTem receiver is successfully suppressing noise, the inability of the SQUID sensor to operate stably at higher transmitter moments makes it unsuitable for use in this noisy environment.

9.4. Conclusions on success of power line noise rejection

1. The BEAMODTM system achieves a 5:1 improvement in suppression of 50 Hz noise in time windows > 1msec, compared with the EM63. This applies over similar sample stacking times, and similar transmitter moments.
2. The inability of the SQUID sensor in its present form to operate stably at comparable transmitter moments makes it unsuitable for use in this noisy environment.

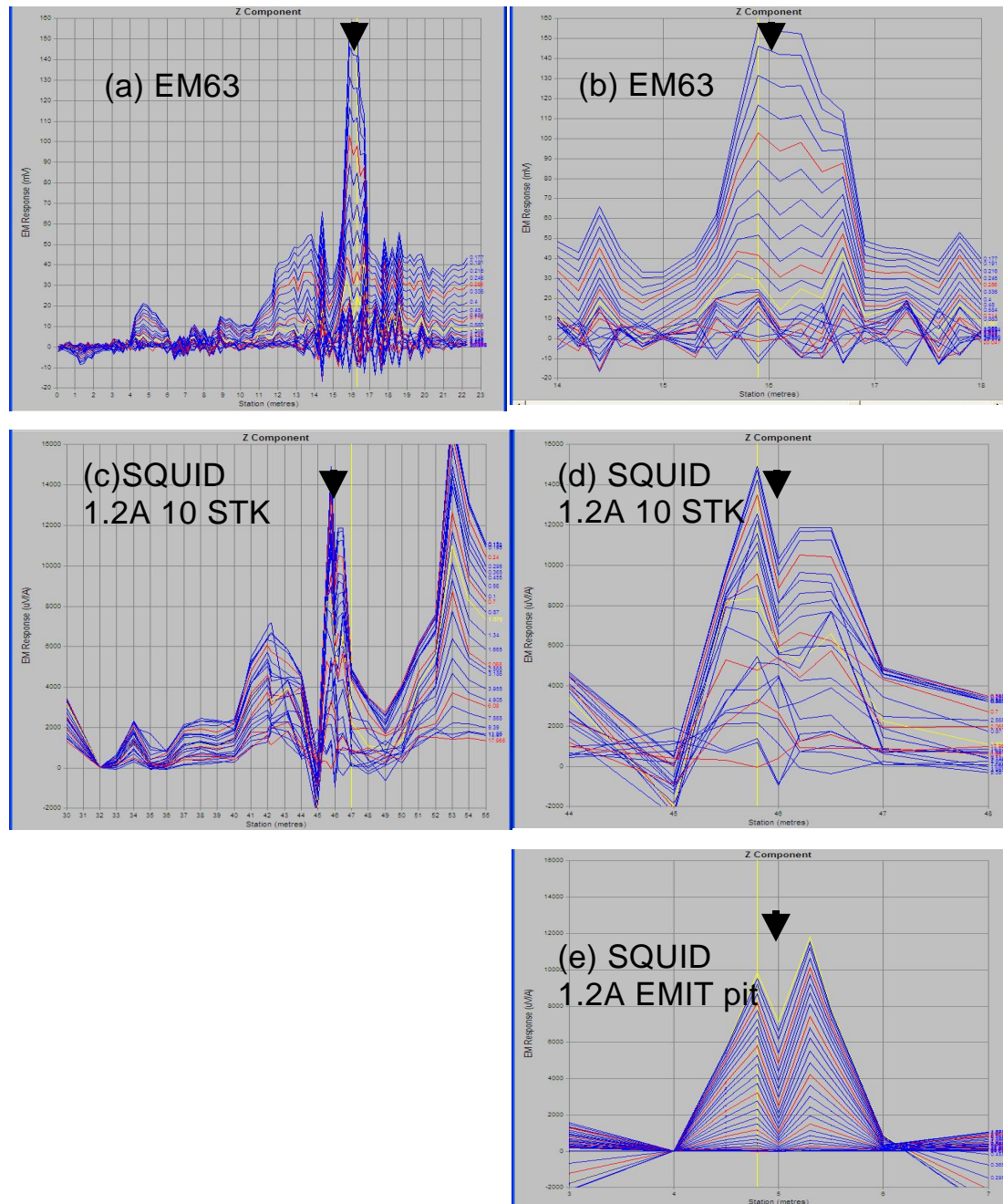


Figure 67 Profiles acquired with the BEAMOD™ Mk2 with SQUID sensor, under power lines

(a) Profile as for Figure 64 acquired with the EM63 instrument, averaged over 0.2 m or 400 msec.

(b) As for (a), using an expanded scale showing the profile from 14 to 18 m. The profile in yellow is for time window 1 msec. The noise envelope associated with 50Hz power-line noise is greater than 50% of the amplitude of the target response at time 1 msec.

(c) Profile of length 23m acquired with the BEAMOD™ Mk2 with SQUID sensor, transmitter current 1.2 A, moment 18 A.m². Data is averaged over 600 msec (10 stacks at 8.33Hz). The arrow at 16 m is the location of a 40mm cannon shell on the ground, which is directly below the power lines.

(d) As for (c), using an expanded scale showing the profile from 14 to 18m. The profile in yellow is for time window 1msec. The noise envelope associated with 50Hz power-line noise is of order 50% of the amplitude of the target response at time 1msec.

(e) Profile over a 40mm shell on ground level, EMIT test pit. Acquired with BEAMOD™ and SQUID.

10. SCOPING OF AN ALGORITHM FOR FAST INVERSION OF EMI DATA OVER A FERROUS TARGET

Development of the algorithm for fast modeling is subject of a separate paper, now accepted for publication in the Journal of Applied Geophysics. The paper is included in this Report as Appendix B, but for completeness of this Report in case of absence of Appendices, the abstract follows.

The time-domain EM induction response of non-magnetic and magnetic targets can be approximated using a conductive permeable prism composed of six faces of conductive plates, each face being composed of a set of conductive ribbons. The effect of magnetic permeability is included by the use of two “apparent flux gathering” coefficients, and two “effective magnetic permeability” coefficients, in the axial and transverse directions. These four magnetic property coefficients are a function of physical properties and geometry of the target, but are independent of prism orientation relative to a transmitter. The approximation algorithm is computationally fast, allowing inversions for target parameters to be achieved in seconds. The model is tested on profiles acquired with a Geonics EM63 time-domain EM metal detector over a non-magnetic copper pipe target, and a steel artillery shell in horizontal and vertical orientations. Results show that this approximation to a permeable prism has a capability of fitting geometric, conductivity and magnetic parameters at both early and late sample times. The magnetic parameters show strong change from early to late times on the EMI decay curve, indicating that the magnetic properties of the target have non-linear characteristics. It is proposed that these magnetic parameters and the nature of their non-linearity may carry additional discrimination information for distinguishing between intact munitions and scrap in UXO studies.

See Appendix B for details of this algorithm.

Section 7.4 also demonstrates the application of this new algorithm to the modeling of B-field responses of both the non-magnetic copper pipe target and selected magnetic steel munitions targets.

11. INVERSION SENSITIVITY WITH THE BEAMOD™ CONFIGURATION

11.1. Modeling and inversion of synthetic data with the BEAMOD™ configuration

We evaluate the usefulness of three-component data from a single vector B-field sensor by generating synthetic data for a known model, adding noise, and then subjecting the synthetic data to inversion with a range of starting parameters. Such studies can become infinitely large if all combinations of fixed and floating parameters are investigated, hence we have selected for presentation just six results which we believe summarize the most important properties of this type of data.

Synthetic data was generated using the copper pipe model developed for Figure 40, placed at a depth below ground of 0.5 m. Gaussian noise was added to the data at the level of 1% data value, plus a white noise floor of 50 pT standard deviation. Six inversions were performed, three using a horizontal and three using a vertically-oriented starting model. Figure 68 shows as a pictorial example the start and end of inversion#4 when using a single 3-component fluxgate sensor. Table 5 shows the resultant inversion parameters for the full set of six inversions.

In Table 6 we show the same synthetic data, restricted to the vertical Z-component only, submitted to the same six inversion tests. Note that the Y-coordinate (transverse to the profile) of the target position is held fixed for these inversions since it is axiomatic that a single profile of Z-component data cannot resolve off-line information.

The results for the two sets of inversions can be summarized with four observations:

For three-component data acquired with a single 3-component vector sensor,

- when the size of the target is known, data inverts to yield the position of the target in X, Y, Z space to order 0.01 m, and orientation to within a few degrees.
- when the size of the target is not known, data inverts to yield the approximate position of the target, but inversion likely to be unstable giving a meaningless estimate of dip and azimuth

For single Z-component data acquired with a single sensor,

- when the size of the target is known, data inverts to yield the position of the target in X, Z space to order 0.1 m, and orientation to within 10 or 20 degrees (ie. an order of magnitude lower precision than in the three-component case).
- when the size of the target is not known, data inverts to yield the approximate position of the target, but inversion likely to be unstable giving a meaningless estimate of dip and azimuth.

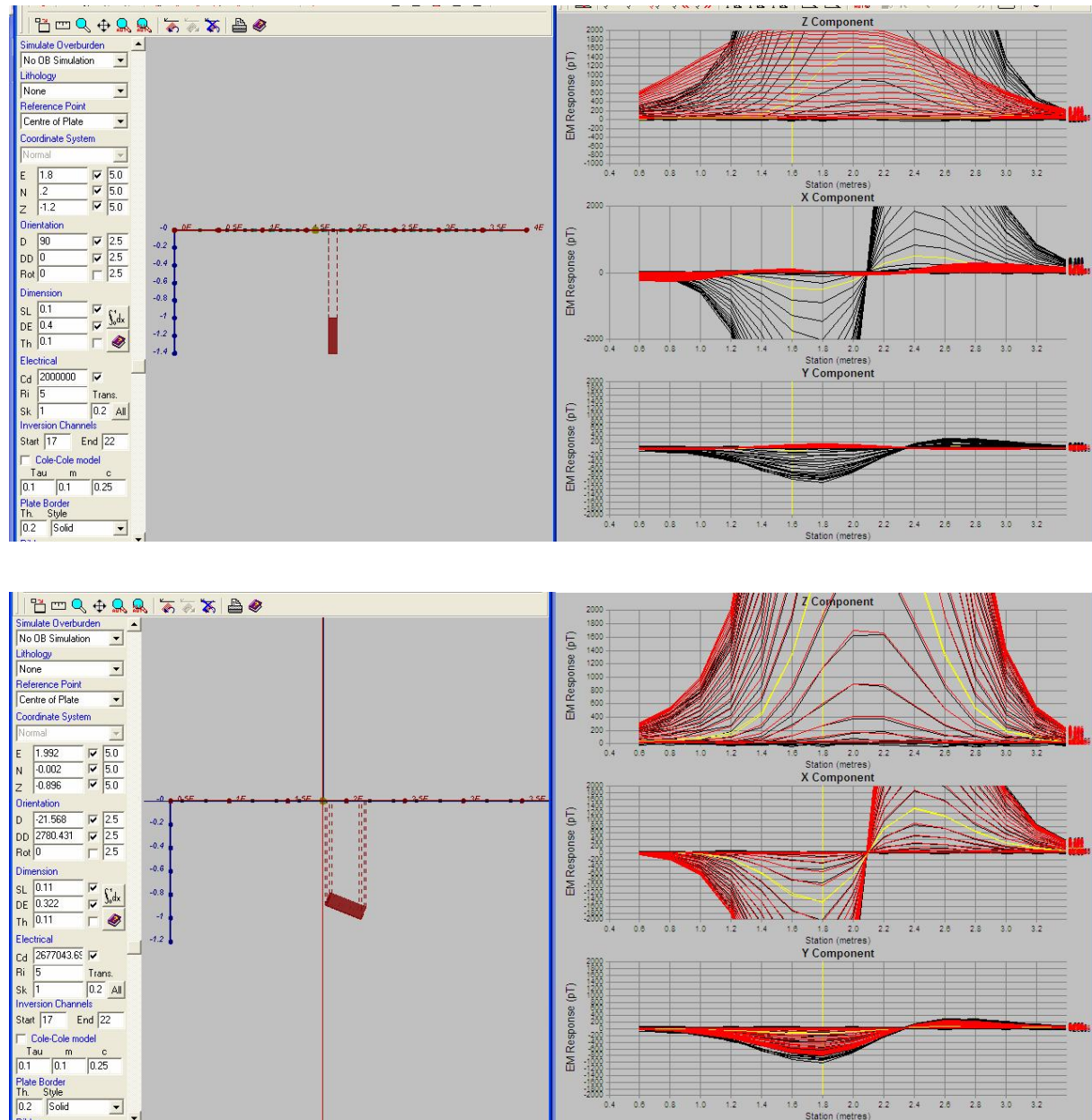


Figure 68 - Starting and fitted models for an example of inversion of synthetic B-field data for a single 3-component B-field sensor.

TOP: At left, the starting model for inversion#4. Black profiles: synthetic data computed using parameters shown in Table 5, and with Gaussian noise added. Red profiles: Starting model.

BOTTOM: The inverted model.

Table 5 – Inversion study on synthetic three-component in-loop B-field data.

Six inversions were performed using starting models as shown. Inversion is based on fitting channels 17-22 (times 3.1-9.4 msec).

Target Parameter	unit	Synthetic data	Start	Inversion1	Inversion2	Start	Inversion3	Inversion4	Start	Inversion5	Start	Inversion6
X	m	2	1.8	2	1.99	1.8	2	2	1.8	2.1	1.8	2.08
Y	m	0	0.2	0	0	0.2	0	0	0.2	0.038	0.2	0.12
Z	m	-0.895	-1.2	-0.896	-0.896	-1.2	-0.896	-0.896	-0.6	-0.662	-0.6	-0.56
Dip	deg	20	0	20	21	90	20	20	0	-8	90	45
azimuth	deg	80	90	80	81	0	80	80	90	15	0	0
Conductivity	Siemen	3.00E+06	2.00E+06	3.06E+06	2.76E+06	2.00E+06	3.06E+06	2.67E+06	1.20E+07	1.00E+07	1.20E+07	1.20E+07
diameter	m	0.1	0.1	0.1	0.106	0.1	0.1	0.11	0.05	0.05	0.05	0.054
length	m	0.4	0.4	0.4	0.353	0.4	0.4	0.322	0.1	0.388	0.1	0.23
comment									erroneous transverse result		erroneous nr-vertical result	

Parameters in red are fixed during the inversion

Table 6 – Inversion study on synthetic single Z-component in-loop B-field data.

Six inversions were performed using starting models as shown. Inversion is based on fitting channels 17-22 (times 3.1-9.4 msec).

Target Parameter	unit	Synthetic data	Start	Inversion1	Inversion2	Start	Inversion3	Inversion4	Start	Inversion5	Start	Inversion6
X	m	2	1.8	2.37	2.04	1.8	1.99	1.9	1.8	2.1	1.8	2.1
Y	m	0	0.2	0	0	0	0	0	0	0	0	0
Z	m	-0.895	-1.2	-0.86	-0.915	-1.2	-0.896	-1.03	-0.6	-0.662	-0.6	-0.662
Dip	deg	20	0	68	10	90	30	31	0	-8	90	-8
azimuth	deg	80	90	-90	90	0	99	90	90	15	0	15
Conductivity	Siemen	3.00E+06	2.00E+06	4.08E+06	2.60E+06	2.00E+06	3.01E+06	2.80E+06	1.20E+07	1.00E+07	1.20E+07	1.00E+07
diameter	m	0.1	0.1	0.1	0.11	0.1	0.1	0.105	0.05	0.05	0.05	0.05
length	m	0.4	0.4	0.4	0.34	0.4	0.4	0.673	0.1	0.24	0.1	0.24
comment				erroneous vertical result					erroneous transverse result		erroneous transverse result	

Parameters in red are fixed during the inversion

Thus we see that in the model studied here, the three-component vector sensor yields greatly superior precision in both location and orientation of the target compared with single Z-component data. However profiles acquired with a single three-component vector sensor do not have sufficient resolution to invert for target size. This is an important result which has implications for target discrimination; we expect the inversion process using a single sensor (whether Z-component or vector) to be much easier if target dimensions for a range of anticipated objects are known a priori from either usage or excavation history.

We now extend this inversion study to the full BEAMOD™ system, using three vector sensors in the configuration shown in Sections 3.4 to 3.7. Table 7 shows results of the equivalent study using the same synthetic data as before (generated for all three receiver sensors, and subjected to the same level of addition of Gaussian noise), and using the same set of six starting models for inversions.

Table 7 – Inversion study on synthetic BEAMOD™ data using three sensors each with three components measuring B-field data.

Six inversions were performed using starting models as shown. Inversion is based on fitting channels 17-22 (times 3.1-9.4 msec).

Target Parameter	unit	Synthetic data	Start	Inversion1	Inversion2	Start	Inversion3	Inversion4	Start	Inversion5	Start	Inversion6
X	m	2	1.8	2.01	2	1.8	2.01	1.99	1.8	2.086	1.8	2.091
Y	m	0	0.2	0	0	0.2	0	0	0.2	0.02	0.2	0.02
Z	m	-0.895	-1.2	-0.883	-0.894	-1.2	-0.883	-0.902	-0.6	-0.735	-0.6	-0.719
Dip	deg	20	0	18.9	20.2	90	19	21.3	0	11.54	90	11
azimuth	deg	80	90	79.6	80	0	11	80.2	90	80.8	0	81
Conductivity	Siemen	3.00E+06	2.00E+06	2.92E+06	2.70E+06	2.00E+06	2.93E+06	2.32E+06	1.20E+07	1.01E+06	1.20E+07	1.10E+06
diameter	m	0.1	0.1	0.1	0.104	0.1	0.1	0.114	0.05	0.049	0.05	0.047
length	m	0.4	0.4	0.4	0.404	0.4	0.4	0.353	0.1	1.035	0.1	1.069
comment												

Parameters in red are fixed during the inversion

11.2. Key results from modeling and inversion studies with the BEAMOD™ configuration on synthetic data

Two key observations can be made from this study with the full BEAMOD™ configuration:

- As with the case of the single vector sensor, when the size of the target is known, data inverts to yield the position of the target in X, Y, Z space to order 0.01 m, and orientation to within a few degrees.
- when the size of the target is not known, data inverts to yield the position of the target with significantly greater accuracy than was the case with the single vector sensor (note Z-coordinate estimates for inversions #5 and #6) AND data inverts stably to yield correct orientation data (whereas the inversion failed on orientation parameters for the single vector sensor).

A question mark remains over the behavior of this prototype inversion approach applied to the BEAMOD™ configuration, as to resolvability of actual size parameters (diameter and length). The diameter parameter appears to vary only slightly during inversions, whereas forward modeling suggests the parameter should be resolvable to a higher degree. Models listed in Tables 5-7 with size parameters different from source parameters used in generating the synthetic data have clearly inferior fits, hence the inversion algorithm is finding a local minimum in fitting error. This matter and means of optimizing the inversion algorithm will be investigated further in a continuation project, but the limitation does not diminish the importance of the results established thus far as to the

advantage of the BEAMOD™ geometry in correctly resolving orientation of the target as an essential aid to target discrimination.

11.3. Modeling and inversion of field data with the BEAMOD™ configuration

Figure 69 shows field data acquired at the Newholme test range using the full BEAMOD™ configuration. The project was limited to the use of a single fluxgate sensor in its first year, so the chosen profile was surveyed in stop-start mode three times with the fluxgate sensor successively in the center ‘C’ position, forward or north ‘N’ position, and the rear or south ‘S’ position, each position having a fixed pair of Helmholtz coils. The transmitter and receiver centers were 135 mm above ground level for these observations (reduced from 395 mm as used in other tests with the BEAMOD™ Mk2 system). Transmitter and receiver specifications were as for other Newholme profiles, i.e. frequency 2.08 Hz and current 12 A.

The profiles have the qualitative form expected for the three sensor positions. Note in particular that the Y-component (transverse to the profile) is much enhanced relative to Z and X components, and relative to the profile passing over the top of the target which is shown in Section 8.2 Figure 53. This enhanced Y-component is due to the east-shift of this profile relative to the target location.

It is not possible to perform an objective inversion with observed data of this complexity at this early stage of the project; the objective in this first year of study is simply to scope out an inversion algorithm and assess feasibility of inversion with a BEAMOD™ type of system. We have performed an inversion for position, orientation and conductivity of a magnetic target using the ‘C’ sensor only, and using fixed magnetic parameters as listed in the caption for Figure 69. This process uses the permeable prism approximation as developed in Section 10. With minor iterative adjustment we obtain the fit for all three sensors with the target model given in Figure 69.

By viewing the observed and model profiles in detail we can gain some semi-quantitative indication of the available resolution of the target length. The physical length of the steel PWH rocket head is listed as 0.42 m in Appendix C. Figure 69 uses a compromise target effective length of 0.3 m. In Figure 70 we show the observed and modeled data for the same target except shorter (0.15 m), and longer (0.4 m). It is apparent that south part of the profile (stations 0-2m) shows a better fit using the shorter length, while the north part of the profile shows a better fit using the longer target length. This discrepancy is probably due to the fact that the target is not a uniform cylinder of steel but has its maximum density in the northern end (nose). We can deduce from this study with the three 3-component sensors the hypothesis that it may be possible to discriminate between nose and tail response of a flat-lying munitions object, which is clearly an attractive prospect for future target discrimination studies.

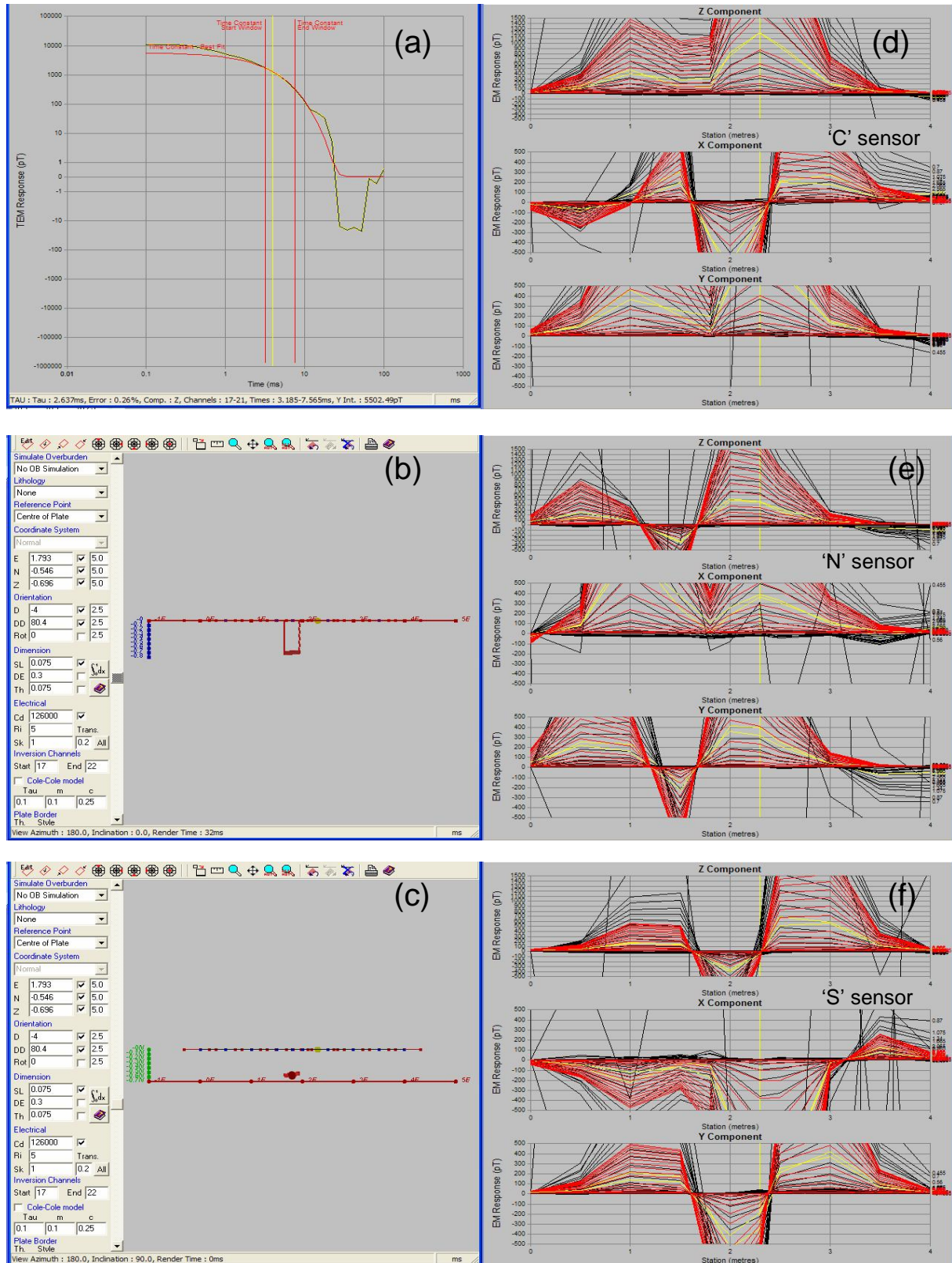


Figure 69 - Profiles and inverted model with all three sensor positions of BEAMOD™ Mk2 (fluxgate sensors) at Newholme test range. Profiles are 0.5 m east of, target 12 (PWH rocket head) at depth 0.5 m, notionally below and east of station 2.0. (See Figure 53 for comparable profile over the top of the target). (Continued next page).

Figure 69 (above) continued:

The target is horizontal, axis parallel with the profile (Files FG714-FG716).

(a) Decay curve for maximum response, 'C' sensor, showing decay constant 2.6 msec.

(b-c) Section and plan view of the fitted model.

(d-f) Profiles for three sensors, each with three components.

Black lines – observed field data.

Red lines – fitted model data for model shown at left.

Yellow lines – observed and fitted data for ch. 18 (3.9 msec).

Inversion parameters (* indicates parameter determined by inversion; other parameters are fixed):

Depth center=0.696* m below transmitter; (ie. Interpreted depth to center of target =0.561 m below ground, compared with notional burial depth of 0.5 mm).

Target Center is X=1.79* m, Y=-0.546* m, conductivity=1.26E5* S/m.

Target orientation is dip=4* deg, azimuth= -10* deg relative to true north.

Apparent flux gathering coefficients $U_1 = 700$, $U_2 = 0.25$.

Effective magnetic permeability $\mu_{e1} = 90$, $\mu_{e2} = 45$.

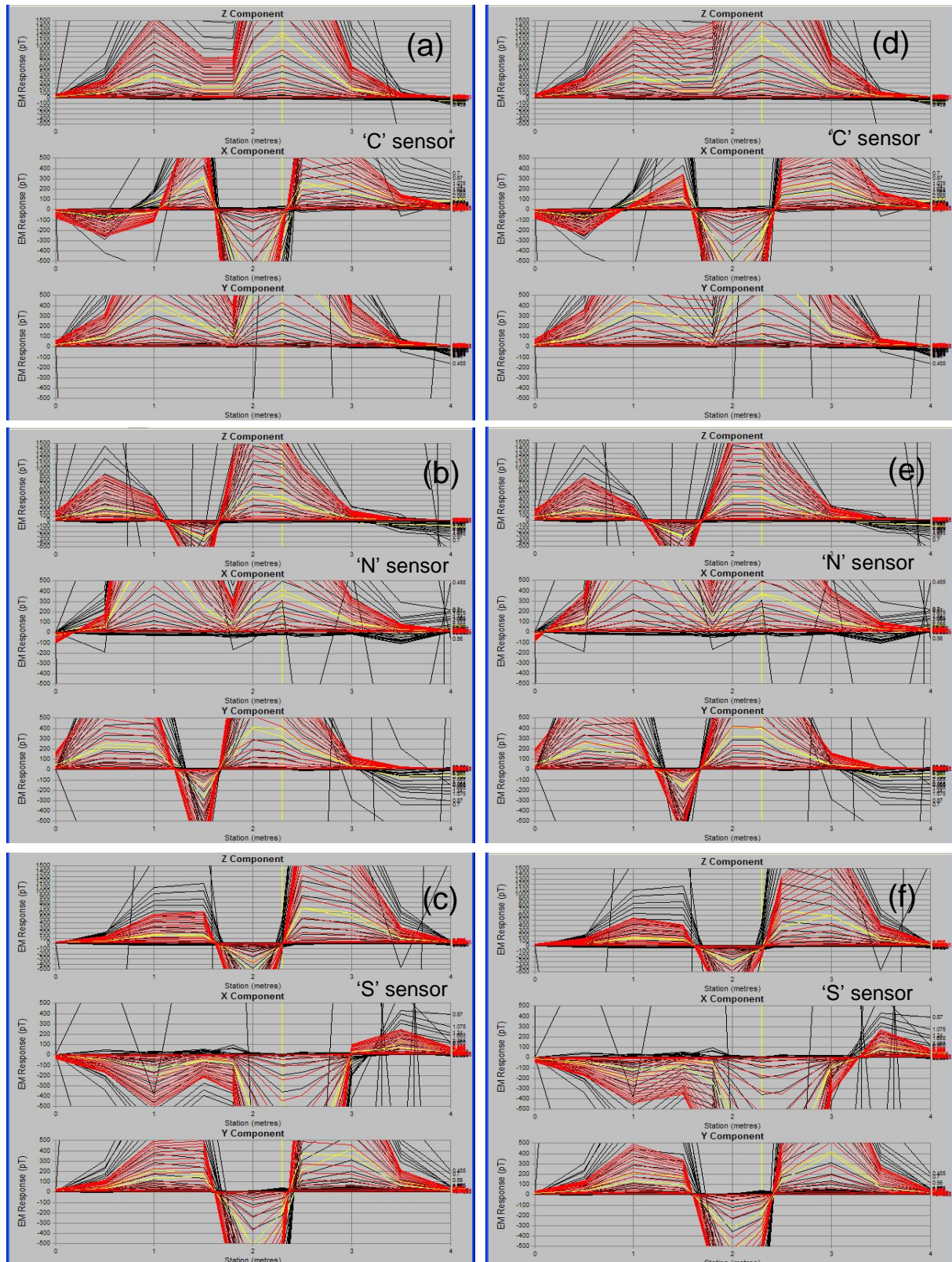


Figure 70 - Profiles and model as for Figure 69, but with (a-c) shorter target length of 0.15 m, and (d-f) with longer target length of 0.4 m.

11.4. Key results from modeling and inversion studies with the BEAMOD™ configuration on field data

Acquisition of sample three-sensor field data by successive profiles acquired with a single sensor in center, north and south positions relative to the transmitter coil shows that such data is

- Feasible using a fluxgate sensor with transmitter moment of 180 Am^2 ,
- Internally consistent, in that the three observed profiles show a high degree of consistency with model data computed for a single target,
- Further demonstrates the utility of the permeable prism approximate model for interpreting EMI data over munitions,
- Allows us to propose the hypothesis: **It is feasible with the full BEAMOD™ geometry to determine position, orientation AND nose direction of a munitions target, and that the difference in response between nose and tail of a flat-lying target may be an additional tool for discrimination of target type.**

12. SUMMARY OF RESULTS MEASURED AGAINST PERFORMANCE METRICS AND RECOMMENDATION

12.1. Metrics objectives

A Metrics statement was requested by SERDP following the February (2006) In-progress Review. It was provided to SERDP on 16 April 2006, and is attached to this Report as Appendix B. Four objectives were stated as follows:

1. Document noise characteristics of the fluxgate and SQUID B-field sensors under study, in a form which allows comparison with laboratory studies of other EM sensors at another time or place;
2. Compare the performance of the fluxgate and SQUID sensors with performance of an industry-standard EM63 instrument over a suite of standard ordnance items and a non-magnetic plumbing-grade copper pipe of specified size and shape;
3. Assess advantages of a vector sensor (fluxgate or SQUID) in the BEAMOD™ configuration, relative to profiles acquired from an EM63 instrument, in interpretation of position and orientation of said targets and
4. Assess advantages of new signal processing technology for UXO EM applications in regards to reduction of noise, particularly in data sets affected by cultural interference.

12.2. Assessment of results against metrics: noise, performance and cost

12.2.1. Noise characteristics

In Section 5 we showed that both the fluxgate and SQUID sensor are able to operate linearly. We have designed and used Helmholtz coils integrated with the BEAMOD™ transmitter to provide primary-field bucking, and have developed software post-processing which delivers linear performance of the receiver over transmitter moments 18 to 195 A.m². We quantified noise as a function of time window for intrinsic noise and geologic noise and found trade-offs as follows:

- a. Fluxgate advantage: operates stably at a transmitter moment 3.4 times larger than SQUID,
- b. SQUID advantage: lower noise in profile applications by factor of order 2 to 5.
- c. SQUID advantage: wider bandwidth, DC to >10kHz.

In addition the fluxgate sensor has advantages of being

- d. A factor x26 cheaper than the SQUID (\$6000 vs \$160,000, although very large reductions in SQUID costs can be expected if multiple units were to be ordered for BEAMOD™ use), and
- e. The fluxgate sensor is physically smaller, physically robust (does not require a Dewar vessel or use of liquid nitrogen on site).

On noise, performance and cost, we make the recommendation that:

We should continue development of the BEAMOD™ system using fluxgate magnetometers in preference to SQUID magnetometers as B-field sensors.

12.2.2. *Compare fluxgate SQUID and EM63 systems over a suite of ordnance targets*

Section 3.3.2 showed a modeling example which illustrates how the B-field detectors have an advantage over conventional dB/dt detectors, in reducing the response associated with near-surface scrap relative to deeper intact targets.

Section 6 and 7 considered target detection vs. depth from both observation and model considerations and showed the B-field detectors to be superior at the level of 20%-47% in depth of detection. Specific findings were:

- a. Copper pipe: The SQUID has an advantage of 1700 mm vs. 1400mm for the EM63 and fluxgate (20% deeper - applies only at short window times <1 msec, which is not of high value).
- b. 40mm cannon shell: The fluxgate sensor has an advantage of 780 mm vs. 530mm for the EM63 (47% deeper).
- c. 75mm cannon shell: The fluxgate sensor has an advantage of 1110 mm vs. 780mm for the EM63 (42% deeper).
- d. BDU33 practice bomb: The fluxgate sensor and EM63 have comparable depth sensitivity at the intermediate time range 5-10 msec, but the fluxgate is strongly superior at late times of order 20 msec, having a computed depth detection advantage of about 780 mm vs 480 mm for the EM63 (50% deeper).
- e. 500 lb Mk 82 practice bomb: profiles over two such targets at the Newholme test range, at depths 0.5 and 2.6 m, show in Section 8.3 that the BEAMOD™ transmitter with a single fluxgate sensor is able to detect this large target at a depth of 2.6 m on all three components of the sensor. No comparative profile from the single-component EM63 is available at this time.

In addition, the B-field sensors are demonstrated to provide three-component data which Section 11 shows provides enhanced precision in location and target orientation.

12.2.3. *Advantage of the vector sensor for determining position and orientation of a target.*

A peer-reviewed paper has been published describing a new very fast approximation algorithm for modeling the response of conductive permeable munitions targets in forward applications and in future inversions.

A novel feature of this algorithm is that it allows estimation of non-linear or frequency-dependent magnetic properties of a steel target, which may prove to be a useful property in target discrimination.

Model studies show the use of a single vector sensor delivers an order of magnitude greater accuracy in location in X,Y,Z space and orientation of the target, compared with the use of z-component only data.

Comparison of the use of a single vector sensor and the BEAMOD™ array of three vector sensors in model studies shows that where the target size is unknown, the single vector sensor is likely to produce unstable orientation estimates, whereas use of the array of three vector sensors delivers accurate and stable estimates of orientation of the unknown target.

Based on a comparison of observed and model data using the full BEAMOD™ configuration over a PWH rocket head at the Newholme UXO test range, we propose a hypothesis for future studies, that it is feasible with the full BEAMOD™ geometry to determine position, orientation AND nose direction of a munitions target, and that the difference in response between nose and tail of a flat-lying target may be an additional tool for discrimination of target type.

12.2.4. *Signal processing for reduction of cultural (power line) noise.*

Section 9 provides a conclusive result of noise reduction and useful operation of the BEAMOD™ system immediately beneath high-tension power lines. Two specific conclusions are:

- a. The BEAMOD™ system achieves a 5:1 improvement in suppression of 50 Hz noise in time windows > 1msec, compared with the EM63. This applies over similar sample stacking times, and similar transmitter moments.
- b. The inability of the SQUID sensor in its present form to operate stably at comparable transmitter moments makes the SQUID sensor in its present form unsuitable for use in this noisy environment.

12.3. Performance of B-field sensor on a moving platform

The fluxgate sensor was successfully operated in continuously-moving profiles over munitions targets at the Newholme UXO Test Range, NSW. At a transmitter frequency of 8.33 Hz and sled speed of 0.2 m/sec the noise floor for data acquired in continuous motion is comparable with the noise floor for profile data acquired in stop-start mode.

12.4. Recommendation

The BEAMOD™ design in its prototype form is proven technically to have superior noise, depth of detection, and capability for determination of target location and orientation. It is recommended that the hardware and software development as envisaged in Project UX-1445 and its preceding three-year proposal, be funded for a further two years, using the fluxgate magnetometer as the basis for an array of vector sensors.

13. REFERENCES

(See also list of references in Appendix B)

Delaney, W., 2003, the 2003 Defense Science Board task force on unexploded ordnance (UXO). Partners in Environmental Technology Technical Symposium and Workshop, December 2003, Session 3B, p. 59.

Duncan A., Williams P., Turner G., Amann B., Tully T., O'Keeffe K., Wellington A. 1998. Examples from a new EM and electrical methods receiver system. *Expl. Geophys.* 29 p347-354.

Foley, C.P., Leslie, K.E., Binks, R., Lewis, C., Murray, W., Sloggett, G.J., Lam, S., Sankrithyan, B., Savvides, N., Katzaros, A., Muller, K.-H., Mitchell, E.E., Pollock, J., Lee, J., Dart, D.L., Barrow, R.R., Asten, M., Maddever, A., Panjkovic, G., Downey, M., Hoffman, C. and Turner, R. 1999, Field trials using HTS SQUID magnetometers for ground-based and airborne geophysical applications: *IEEE Trans. Appl. Supercond.* 9, no. 2, 3786-3792.

Lee, J.B., Turner, R.J., Downey, M.A., Maddever, A., Dart, D.L., Foley, C.P., Binks, R., Lewis, C., Murray, W., Panjkovic, G., and Asten, M.W., 2001, Experience with SQUID magnetometers in airborne TEM surveying: *Exploration Geophysics*, 32, 9-13.

McCracken, K.G., Oristaglio, M.L. and Hohmann, G.W., 1986, Minimization of noise in electromagnetic exploration systems: *Geophysics* v.51. (3) 819-832.

APPENDIX A

METRICS FOR PROJECT UX1445

The document in this Section was provided to SERDP in April 2006 in response to a request at the IPR February for a set of metrics for the project

A1. Objectives

The object of the following is to:

1. Document noise characteristics of the fluxgate and SQUID B-field sensors under study, in a form which allows comparison with laboratory studies of other EM sensors at another time or place;
2. Compare the performance of the fluxgate and SQUID sensors with performance of an industry-standard EM63 instrument over a suite of standard ordnance items and a non-magnetic plumbing-grade copper pipe of specified size and shape;
3. Assess advantages of a vector sensor (fluxgate or SQUID) in the BEAMOD™ configuration, relative to profiles acquired from an EM63 instrument, in interpretation of position and orientation of said targets and
4. Assess advantages of new signal processing technology for UXO EM applications in regards to reduction of noise, particularly in data sets affected by cultural interference.

A2. Noise characteristics

For each of the fluxgate and SQUID sensors, using a nominal 2 Hz base frequency, measure using 64 stacks (half periods) in each of 15 separate successive recordings and present:

- a. With transmitter inactive, measure intrinsic sensor noise in a mu-metal magnetically-shielded box. Results to be presented as noise in $\text{pT/Hz}^{1/2}$ RMS for time windows 0.5 to 50 msec, for specified window widths.
- b. With transmitter inactive, measure unshielded noise (effectively, a measure of system noise at the time and place of the measurement). Results to be presented as:
 - i. noise in $\text{pT/Hz}^{1/2}$ RMS for time windows 0.5 to 50 msec, for specified window widths,
 - ii. point-to-point variation in 15 successive noise readings at a single fixed station, after trend removal (for consistency with section 3) below). Standard deviation of the 15 readings.
- c. With transmitter inactive, measure point-to-point variation in 15 successive noise readings (after trend removal) while stepping the sensor along a profile used for subsequent observations of ordnance response. Standard deviation of the 15 readings.

- d. With the *transmitter active*, measure point-to-point variation in 15 successive readings (after trend removal) while stepping the sensor along the profile used for subsequent observations of ordnance response. (This is a profile of the geological signal at the ordnance test site). Standard deviation of the 15 readings.

Include measurement with the EM63 instrument, measure and present as in (d) above.

A3. Comparison of signal/noise over metallic targets

Profiles and time-domain EM decay curves for the three systems (fluxgate, SQUID sensors, and EM63), over five standard metallic sources, placed at four different depths, as per Table 7 below.

This comparison will show:

- a. the decay curve at peak response for each sensor, each target, each depth;
- b. the time window range of target response amplitude, relative to the noise standard deviation as measured in (d) above.

Table 8 – Metallic Objects and Munitions under Test – Project UX1445

ITEM	TARGET DEPTH			
	0	300	530	(mm) 880
Copper pipe		x	x	x
20 mm shell	x	x		
40 mm shell	x	x	x	
75 mm shell		x	x	x
150 mm practice bomb				x

Techniques for the processing of SQUID and fluxgate sensor data profiles have been developed during our project. These will be employed for this comparison. Measurements of performance of fluxgate and SQUID sensors in this project have been made with sensors nominally static. Our comparison will include allowance for this in contrast to the dynamic measurements made with EM63.

A4. Advantages of the vector sensor in BEAMOD™ configuration

Advantages of the two B-field sensors (either or both) in the BEAMOD™ configuration (9-component = 3 tri-axial sensors), when benchmarked against the standard commercial EM63 instrument, are to be assessed using the following:

- a. Present observed profile of BEAMOD™ 9-component data over a selected target (a 75 mm cannon shell at 530 mm depth),
- b. Present model studies of BEAMOD™ geometry for a copper pipe (100 mm diameter, 400 mm long),

- c. Using (a) and (b) as input, provide inversion comparison of EM63 profile, measured BEAMOD™ 9-component profile, and numerically modeled BEAMOD™ 9-component data; assess accuracy of recovery of location and attitude of target. (Model data has random noise added before inversion).

Techniques for the processing of SQUID and fluxgate sensor data profiles have been developed during our project. These will be employed for this comparison. Measurements of performance of fluxgate and SQUID sensors in this project have been made with sensors nominally static. Our comparison will include allowance for this in contrast to the dynamic measurements made with EM63.

A5. Advantages of real-time signal processing in BEAMOD™ system

Advantages of real-time signal processing (particularly relating to rejection of power line noise) in the BEAMOD™ system, when benchmarked against the standard commercial EM63 instrument, is to be assessed by presenting comparable profiles of EM63 and a SQUID sensor under power lines. The level of power line noise rejection will be assessed, relative to a reference signal level provided by a 40mm cannon shell at earth surface.

A6. Criterion for success of this project

One of,

One or both B-field vector sensors achieves a greater time window range of detection (i.e. bandwidth of detection) than the EM63, for the majority of the targets listed in Table 1,

or,

One or both B-field vector sensors in BEAMOD™ configuration has comparable bandwidth of detection compared with the EM63, but provides higher precision in fixing location and orientation of an ordnance target, when inverting field or model data.

or,

One or both of the B-field vector sensors in BEAMOD™ trials, interfaced to "new" (SMARTem) real-time signal processing equipment, has comparable bandwidth of detection compared with the EM63 in measurements relatively free of power line noise, but provides an improvement in bandwidth of detection of at least a factor of 2 over EM63 in a "culturally noisy" environment in the vicinity of power lines.